

Non-equilibrium of charged particles in swarms and plasmas—from binary collisions to plasma effects

Z Lj Petrović^{1,2}, I Simonović, S Marjanović¹, D Bošnjaković¹, D Marić¹, G Malović¹ and S Dujko¹

¹ Institute of Physics, University of Belgrade, POB 68, 11080 Zemun, Belgrade, Serbia

² Serbian Academy of Sciences and Arts, 11001 Belgrade, Serbia

E-mail: zoran@ipb.ac.rs

Received 23 July 2016, revised 12 September 2016

Accepted for publication 22 September 2016

Published 2 November 2016



Abstract

In this article we show three quite different examples of low-temperature plasmas, where one can follow the connection of the elementary binary processes (occurring at the nanoscopic scale) to the macroscopic discharge behavior and to its application. The first example is on the nature of the higher-order transport coefficient (second-order diffusion or skewness); how it may be used to improve the modelling of plasmas and also on how it may be used to discern details of the relevant cross sections. A prerequisite for such modeling and use of transport data is that the hydrodynamic approximation is applicable. In the second example, we show the actual development of avalanches in a resistive plate chamber particle detector by conducting kinetic modelling (although it may also be achieved by using swarm data). The current and deposited charge waveforms may be predicted accurately showing temporal resolution, which allows us to optimize detectors by adjusting the gas mixture composition and external fields. Here kinetic modeling is necessary to establish high accuracy and the details of the physics that supports fluid models that allows us to follow the transition to streamers. Finally, we show an example of positron traps filled with gas that, for all practical purposes, are a weakly ionized gas akin to swarms, and may be modelled in that fashion. However, low pressures dictate the need to apply full kinetic modelling and use the energy distribution function to explain the kinetics of the system. In this way, it is possible to confirm a well established phenomenology, but in a manner that allows precise quantitative comparisons and description, and thus open doors to a possible optimization.

Keywords: charged particle swarms, non-equilibrium plasma, skewness, resistive plate chambers, positron traps, Monte Carlo simulations, Boltzmann equation

(Some figures may appear in colour only in the online journal)

1. Introduction

The idea of thermodynamic equilibrium (TE) is one of the most widely used ideas in the foundations of plasma physics. Not only is TE used as a background gas, but it is also used as the plasma itself, and, further, TE is implicitly incorporated in most theories through application of the Maxwell Boltzmann distribution function. On the other hand, the idea of local thermodynamic equilibrium (LTE) in principle

means that TE is not maintained, and that energy converted into the effective temperature is being used as a fitting parameter, but also that all the principles of TE still apply for the adjusted (local) temperature. It is often overlooked that TE implies that each process is balanced by its inverse process. It is difficult to envisage just exactly how this condition could be met under circumstances where most of the energy that is fed into the non-equilibrium, low-temperature discharges comes from an external electric field. The notion

of non-equilibrium is implemented very well in a wide range of plasma models, starting from fluid models and hybrid models, all the way to fully kinetic codes such as particle-in-cell (PIC) modelling.

At end of a field of ionized gases, opposite to the fully developed plasma, at the lowest space charge densities, electrons are accelerated (gain energy) from the external electric field and dissipate in collisions with the background gas. This realm is known as a swarm (swarm physics), and is often described by simple swarm models. We shall try to illustrate how and where one may employ concepts developed in low-temperature plasmas for problems that are not traditional non-equilibrium plasmas such as positrons in gases and gas-filled traps, gas breakdown and particle detectors.

The three selected examples are: the use and properties of higher-order transport coefficients (skewness) and how they may be implemented to close the system of equations for modeling of atmospheric plasmas; modeling of resistive plate chamber (RPC) particle detectors with a focus on the development of avalanches, and prediction of the current and deposited charge; and, finally, modeling of a generic representation of the three stage gas-filled positron trap, where the same models as for electrons may be employed in a full kinetic description to calculate the temporal development of the energy distribution function, and, through that, to describe how and when individual elementary processes affect the performance of the trap.

This is a review article as it covers three different topics that will (or have been) be presented in detail elsewhere. Yet the majority of the results will be developed in this paper. Necessarily, as it is a broad review, some finer points will be omitted in pursuit of the bigger picture, however, all will be covered elsewhere and the relevant literature is cited.

2. Higher-order transport and plasma modeling

The fluid equations often employed in plasma modeling are a part of an infinite chain, and whenever the chain is broken one needs a higher-order equation and related quantities to close the system of equations (Dujko *et al* 2013). That is why a closing of the equations is forced, sometimes labeled as ansatz, although the closure is not quite arbitrary. It is often based on some principles or simplifying arguments (Robson *et al* 2005) involving higher-order equations and related transport coefficients. Robson *et al* (2005) claimed that some serious errors have been incorporated into fluid equations that are commonly used in plasma modeling, and suggested benchmarks to test plasma models.

Equations (1) and (2) shown below, are the flux gradient equation and generalized diffusion equation, respectively, truncated at the contribution of the third order transport coefficients (also known as skewness). The terms, including $\widehat{Q}^{(F)}$ and $\widehat{Q}^{(B)}$ are terms that represent the contribution of the skewness tensor:

$$\vec{\Gamma}(\vec{r}, t) = \vec{W}^{(F)} n(\vec{r}, t) - \widehat{D}^{(F)} \cdot \nabla n(\vec{r}, t) + \widehat{Q}^{(F)} : (\nabla \otimes \nabla) n(\vec{r}, t) + \dots \quad (1)$$

$$\begin{aligned} \frac{\partial n(\vec{r}, t)}{\partial t} + \vec{W}^{(B)} \cdot \nabla n(\vec{r}, t) - \widehat{D}^{(B)} : (\nabla \otimes \nabla) n(\vec{r}, t) + \widehat{Q}^{(B)} : (\nabla \otimes \nabla \otimes \nabla) n(\vec{r}, t) + \dots \\ = Rn(\vec{r}, t) \end{aligned} \quad (2)$$

where $\vec{\Gamma}(\vec{r}, t)$, $n(\vec{r}, t)$, $\vec{W}^{(F)}$, $\widehat{D}^{(F)}$, $\widehat{Q}^{(F)}$, $\vec{W}^{(B)}$, $\widehat{D}^{(B)}$, $\widehat{Q}^{(B)}$, R are the flux of charged particles, charged particle number density, flux drift velocity, flux diffusion tensor, flux skewness tensor, bulk drift velocity, bulk diffusion tensor, bulk skewness tensor and rate for reactions, respectively. If equations (1) and/or (2) are coupled to the Poisson equation for an electric field then the system of corresponding differential equations might be closed in the so-called local field approximation. This means that all transport properties are functions of the local electric field. The skewness tensor has been systematically ignored in previous fluid models of plasma discharges, although its contribution may be significant for discharges operating at high electric fields, and in particular for discharges in which the ion dynamics play an important role.

As for experimental determination of the higher-order diffusion of electrons, there have been some attempts, but those were mostly regarded as unsuccessful due to the end effects (Denman and Schlie 1990). In other words, those experiments may have failed to comply with both the requirements for negligible non-hydrodynamic regions and for lower pressures. An estimate was made that reliable skewness experiments would have to be up to 10 m long with pressures that are at least ten times smaller than those in standard swarm experiments. It seems that the only reliable yet very weak result was observed for H₂ in time of flight (TOF) emission experiments of Blevin *et al* (1976, 1978), as described in the PhD thesis by Hunter (1977). This is because the measurement was made away from the electrodes, thus providing a hydrodynamic environment.

At the same time some calculations were performed based on the available cross sections either by using a Monte Carlo simulation (MCS) and two term solutions of the Boltzmann equation (BE) (Penetrante and Bardsley 1990) or by using the momentum transfer theory (Vrhovac *et al* 1999). Whealton and Mason (1974) were the first to determine the correct structure of the skewness tensor in the magnetic field free case. For ions there have been more general studies and in particular theoretical studies. Koutselos gave a different prediction of the structure and symmetry of the tensor (Koutselos 1997) but those results were challenged (corrected) by Vrhovac *et al* (1999), who confirmed the structure of the skewness tensor previously determined by Whealton and Mason. Subsequently Koutselos confirmed the structure of the skewness tensor obtained by previous authors (Koutselos 2001).

Finally, having in mind the need for data in fluid modeling and the poor likelihood of experimental studies in the near future, a systematic study has been completed by Simonović *et al* (2016) dealing with the symmetry by using the group projector method (Barut and Raczka 1980, Tung 1984), multi-term Boltzmann equation solutions and MCS results in general terms. It should be noted that the third-order transport coefficients are often called skewness, but in principle it is the term that was to be applied only for the longitudinal diagonal

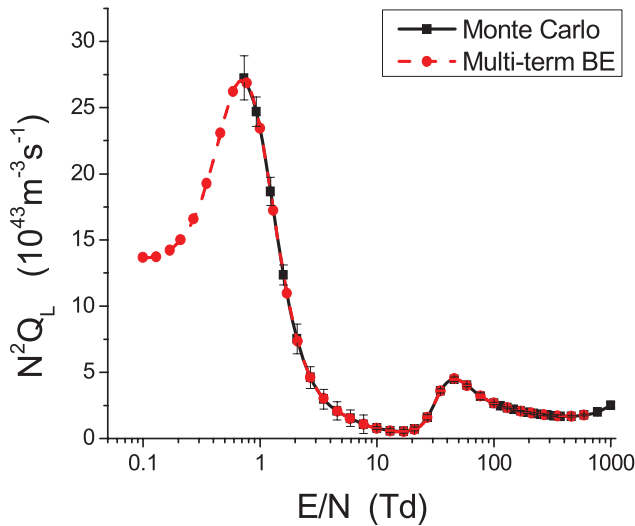


Figure 1. The longitudinal component of the skewness tensor calculated for electrons in methane.

term, which defines most directly the (departure from the) shape of the moving Gaussian. We will, however, use the term skewness for the entire tensor and all its terms.

The structure of the skewness tensor is the following (Wheaton and Mason 1974, Vrhovac *et al* 1999, Koutselos 2001, Simonović *et al* 2016):

$$Q_{xab} = \begin{pmatrix} 0 & 0 & Q_{xxz} \\ 0 & 0 & 0 \\ Q_{xxz} & 0 & 0 \end{pmatrix}, \quad Q_{yab} = \begin{pmatrix} 0 & 0 & 0 \\ 0 & 0 & Q_{xxz} \\ 0 & Q_{xxz} & 0 \end{pmatrix}$$

$$Q_{zab} = \begin{pmatrix} Q_{zxx} & 0 & 0 \\ 0 & Q_{zxx} & 0 \\ 0 & 0 & Q_{zzz} \end{pmatrix},$$

where $a, b \in \{x, y, z\}$ and Q_{abc} are the independent, non-zero terms in the tensor (although some of them may be identical if they are established for different permutations of the same derivatives). The components of the tensor may be grouped as longitudinal $Q_L = Q_{zzz}$ and transverse $Q_T = \frac{1}{3}(Q_{zxx} + Q_{xxz} + Q_{xxz})$.

In this paper, we present results for skewness of electron swarms in methane. Methane is known for producing negative differential conductivity (NDC) and in this work we will demonstrate the unusual variation of the longitudinal and transverse components of the skewness tensor for E/N (electric field over the gas number density) regions in which NDC occurs. NDC is characterized by a decrease in the drift velocity despite an increase in the magnitude of the applied reduced electric field. Cross sections for electron scattering in methane are taken from Šašić *et al* (2004). For the purpose of this calculation we assumed a cold gas approximation: $T = 0\text{K}$, which is justified as we covered mostly the E/N range where mean energies are considerably higher than the thermal energy. The initial number of electrons in the simulations was 10^7 and those were followed for sufficient time to achieve full equilibration with the applied field before sampling was applied. Sampling in an MCS is performed either

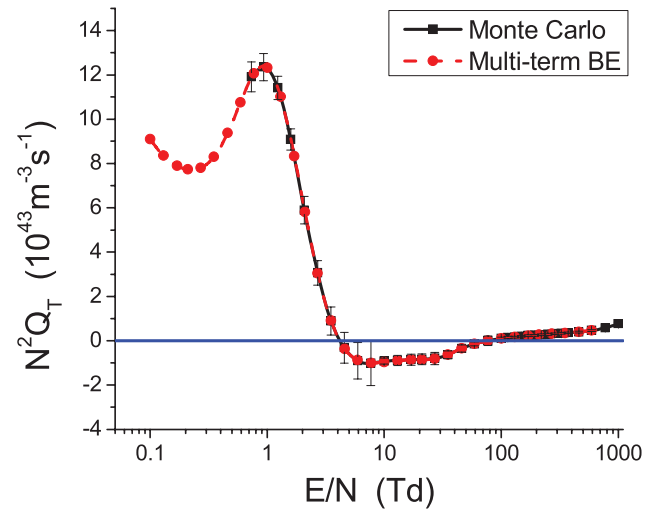


Figure 2. The transverse component of the skewness tensor calculated for electrons in methane.

for the flux (velocity space) $Q_{abc}^{(f)} = \frac{1}{3!} \left\langle \frac{d}{dt} (r_a^* r_b^* r_c^*) \right\rangle$ or for the bulk (real space) $Q_{abc}^{(b)} = \frac{1}{3!} \frac{d}{dt} \langle r_a^* r_b^* r_c^* \rangle$ components (Simonović *et al* 2016) where $r_a^* = r_a - \langle r_a \rangle$.

Uncertainties are established as the root mean square deviations. Statistical fluctuations in MCSs are more pronounced for skewness than for the lower-order transport coefficients. Thus, it is very important to present statistical uncertainties (errors) associated with the results. In addition to Monte Carlo results, the skewness tensor is calculated from the multi-term Boltzmann equation solution. The explicit formulas for skewness tensor elements in terms of moments of the distribution function will be given in a forthcoming paper (Simonović *et al* 2016).

In figures 1 and 2 we show the variation of the longitudinal and transverse skewness tensor components with E/N for electrons in CH_4 , respectively. In figure 3 we show the variation of independent components of the skewness tensor with E/N . The independent components of the skewness tensor have been calculated from a multi-term solution of the Boltzmann equation.

The first observation that is very important is that the multi-term Boltzmann equation results agree very well with those obtained in MCSs. This is an important cross check and it means that the techniques to calculate the skewness are internally consistent, although two very different approaches are implemented (having said that we assume that the solution to the Boltzmann equation and the MC are both well established and tested (Dujko *et al* 2010)).

We see that Q_T becomes negative in the same range of E/N where NDC occurs. At the same time Q_L remains positive. Q_{zxx} and the sum of Q_{xxz} and Q_{xxz} are negative in different regions of E/N .

Comparing the second- and third-order longitudinal transport coefficients we noticed that if diffusion decreases with increasing E/N then the skewness also decreases, but even faster (figures 4 and 5). When it comes to the effect of the cross sections (or inversely to the ability to determine the cross sections from the transport data) it seems that skewness has a

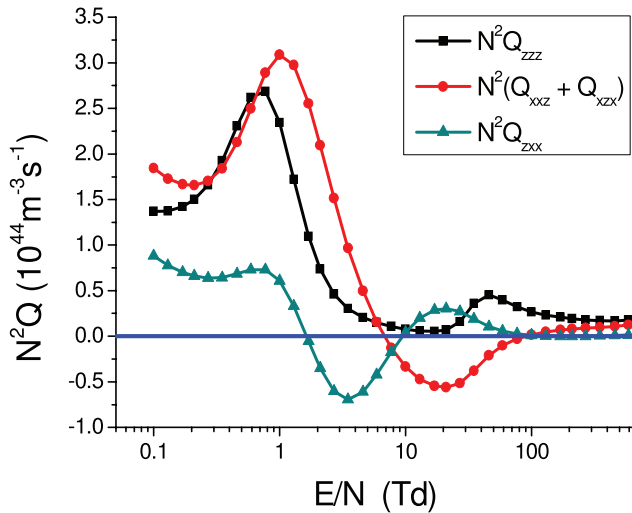


Figure 3. All independent components of the skewness tensor calculated for electrons in methane.

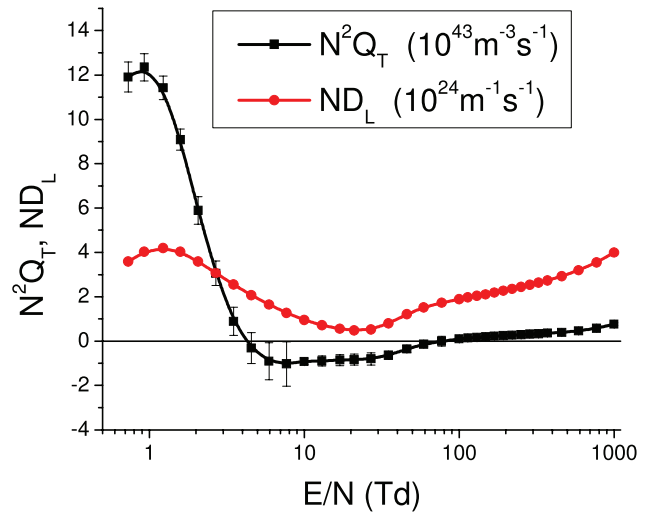


Figure 5. Comparison between longitudinal diffusion and transverse skewness for electrons in methane (the scale for the two different transport coefficients are provided in the legend).

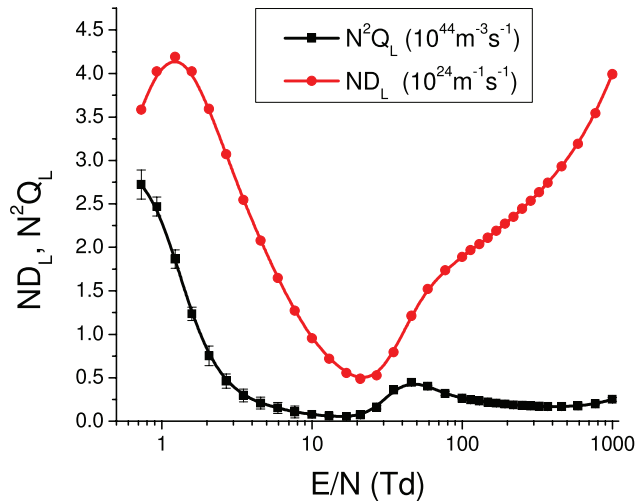


Figure 4. Comparison between longitudinal diffusion and skewness for electrons in methane (the scale for the two different transport coefficients are provided in the legend).

more pronounced structure, and thus is more useful in fixing the shape and absolute values of the cross sections. If the diffusion increases, then we are able to distinguish between the two scenarios: if diffusion increases as a concave function, then the skewness decreases, while if the diffusion increases as a convex (or linear) function then the skewness increases.

We have observed that the transverse skewness is also in a good, if not better, correlation with the longitudinal diffusion (figure 5). This is a good example that illustrates that the skewness tensor represents directional motion.

Different transverse components have different E/N profiles. Q_{zxx} follows the behavior of the drift velocity while the remaining components change their trends of behavior near the end of the NDC region (figure 6). For different gases we have seen different trends and a clear correlation was not found (Simonović *et al* 2016).

Furthermore, but without illustrating it with special figures, the explicit effect of non-conservative collisions (ionization in this case) has been observed. However, in many cases the

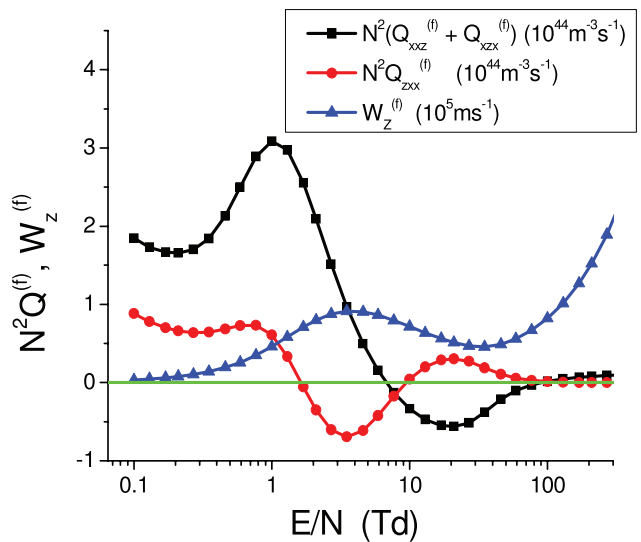


Figure 6. Off-diagonal components of skewness compared to the drift velocity for electrons in methane (the scale for the two different transport coefficients are provided in the legend).

agreement between multi-term BE results and those obtained in MCSs is better than what would be expected based on the estimated errors. At the same time it turned out that discrepancies between a two-term and multi-term (MCS) results may be quite large, ranging up to a factor of 10.

Possible measurements of higher-order transport coefficients seem possible and also profitable for the sake of determining the cross sections. Nevertheless the difficulties and possible uncertainties may outweigh the benefits. Thus, calculation of the data seems like an optimum choice for application in higher-order plasma models. The behavior of higher-order transport coefficients provides an insight into the effect of individual cross sections (their shape and magnitude), and their features such as the Ramsauer Townsend effect or resonances on the overall plasma behavior. The transport coefficients as an intermediate step give a guidance, especially when they develop special features (kinetic effects

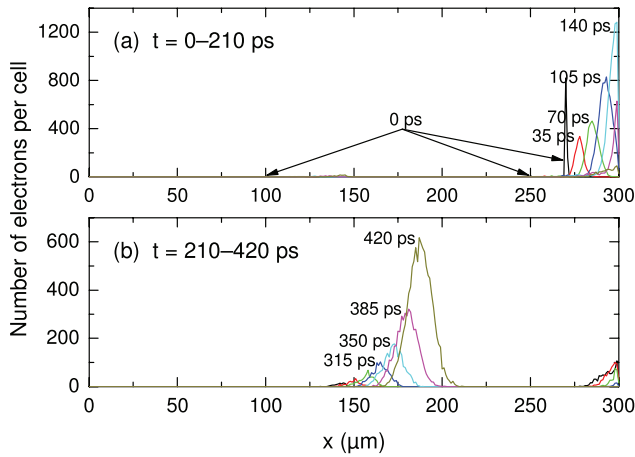


Figure 7. The spatio-temporal development of electron avalanches ((a) and (b)) in an RPC device. The number of electrons per cell (1D integration of a 3D simulation) is shown where the cells (1 cell = 1 μm) are along the discharge axis x . The cathode corresponds to $x = 0$ while the anode corresponds to $x = 300 \mu\text{m}$.

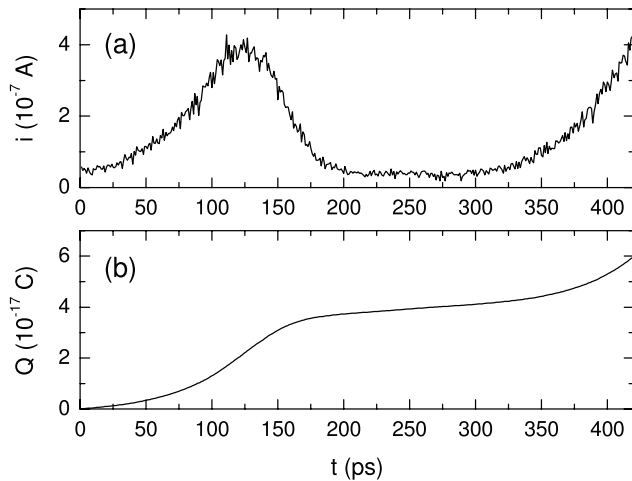


Figure 8. The time development of (a) electron induced current and (b) induced charge in the RPC device.

(Petrović *et al* 2009)) that may also be easily implemented in the determination of the cross sections.

3. Avalanches in resistive plate chambers

The next example of the connection of the elementary processes to plasma behavior through intermediate swarm-like phenomenology modeling will be modeling of RPC detectors. These devices are used for timing and triggering purposes in many high-energy physics experiments at CERN and elsewhere (The ATLAS Collaboration 2008, Santonico 2012). RPCs may be both used for spatial and temporal detection while providing large signal amplifications. They are usually operated in avalanche (swarm) or plasma (streamer) regimes depending on the required amplification and performance characteristics. Numerous models have been developed to predict RPC performance and modes of operation (Lippmann *et al* 2004, Moshaii *et al* 2012). We have studied systematically the swarm data (Bošnjaković *et al* 2014a) and then the

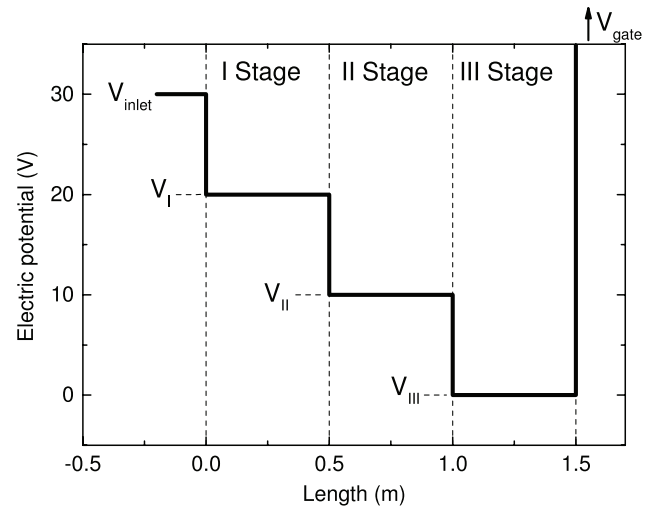


Figure 9. Schematic drawing of a generic Surko trap consisting of three equal potential drops. The composition of the background gas, its pressure and geometry are given in table 1.

Table 1. Parameters for simulation of a generic positron Surko trap.

| Parameters | Stage I | Stage II | Stage III |
|--|--------------|--------------|--|
| Radius (mm) | 5 | 20 | 20 |
| Length (m) | 0.5 | 0.5 | 0.5 |
| Pressure (Torr) | 10^{-3} | 10^{-4} | 10^{-5} |
| Background gas | N_2 | N_2 | $\text{N}_2^{0.5} + \text{CF}_4^{0.5}$ |
| Magnetic field (G) | 530 | 530 | 530 |
| Voltage (V) | 20 | 10 | 0 |
| The initial parameters | | | |
| Potential of the entrance electrode (V) | 30 | | |
| Potential of the source (V) | 0.1 | | |
| Width (FWHM) of the initial energy distribution (eV) | 1.5 | | |

model of RPCs (Bošnjaković *et al* 2014b) where RPC efficiency and timing resolution have been predicted by MCS without any adjustable parameters, and were found to agree with experiment very well. Here we show some of the data not presented in Bošnjaković *et al* (2014b), which focuses on avalanche development and furthermore the induced current and charge.

Calculations of the development of the Townsend avalanche have been performed for a timing RPC gas mixture of $\text{C}_2\text{H}_2\text{F}_4:i\text{-C}_4\text{H}_{10}:\text{SF}_6 = 85:5:10$ with realistic chamber geometry (gas gap = 0.3 mm) at $E/N = 421 \text{ Td}$. We show in figure 7 the development of an avalanche in the gap with three initial clusters of charges (first generation secondary electrons indicated by arrows at 0 ps) formed by an incoming high-energy particle. The first cluster (from the left) has one electron, the second has nine and the third has 983 initial electrons. The distribution over a small group of cells has been randomly selected according to well-established distributions. At the beginning, the initial condition shapes the profile of the ensemble, but eventually a Gaussian is formed that drifts under the influence of an electric field and diffuses due to numerous collisions.

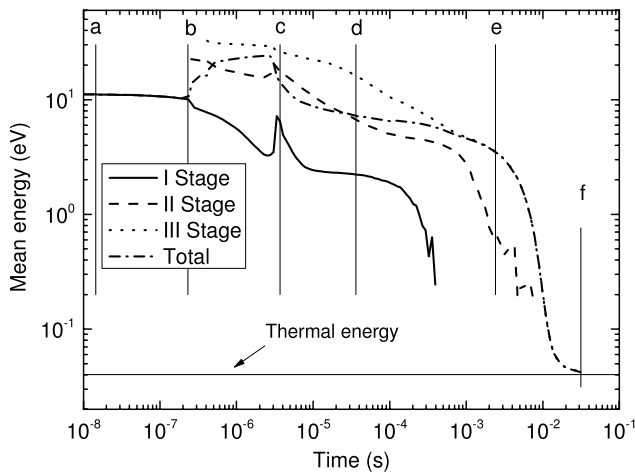


Figure 10. The mean energy of the positron ensemble (swarm) as a function of time. Averages for each stage and for the entire volume (total) are provided. The energy distribution function is plotted in figure 11 for the times marked by the points (a)–(f) in this figure.

We will first follow the development of the cluster closest to the anode (at $270 \mu\text{m}$), as indicated by spatial electron profiles at different times in figure 7(a). The largest initial group, which is also the closest to the anode, develops the fastest: from the initial very sharp profile it quickly establishes a Gaussian shape that also very quickly gets absorbed by the anode. The second peak (from the right) is quick to follow but it is very small and cannot be observed clearly due to interference from the first pulse. In figure 7(b), we show the development of the first cluster (at $100 \mu\text{m}$) for longer times. This cluster is the furthest from the anode and it takes the most time to reach the anode, again as a well developed moving Gaussian. It develops, however, a well-separated and defined current pulse (unlike the second cluster of charged particles). The induced current and the corresponding induced charge are shown in figure 8.

The predictions in figure 8, extended to provide important information on the temporal resolution, may be used to optimize the device by changing gas composition, field and geometry, and also may be extended to allow for the formation of the plasma in later stages when a streamer discharge may be generated at atmospheric pressure (Bošnjaković *et al* 2016). Trial and error development of such devices is simply too costly to allow for an empirical learning curve. Nevertheless, one could argue that it could be possible to develop a model based on a standard swarm description of a moving Gaussian with drift and diffusion plus the benefit of multiplication through ionization. All of these processes have their swarm coefficients. However, the very short times of the formation of the initial cluster, it being inhomogeneous and a very nonlinear growth with a possible separation of faster and slower electrons, dictate the need to perform an MCS in order to achieve the required accuracy. Thus, this example allows for the use of transport coefficients, but is better accomplished by full kinetic modeling. Transport coefficients are better taken advantage of in fluid modeling of the possibly developing streamer (Bošnjaković *et al* 2016). In any case, the ionized gas and the developing plasma channel are both represented very

accurately (qualitatively and quantitatively). Here we have used kinetic swarm modeling, although using transport coefficients may also be an option, albeit a less accurate option.

4. Gas-filled positron (and electron) traps

While it is often assumed that keeping the antimatter away from the matter is a way of preserving it longer, the introduction of background gas to the vacuum magnetic field trap led to the birth of the so-called Penning Malmberg Surko traps (often known simply as Surko traps). These devices take advantage of the very narrow region of energies, where in nitrogen electronic excitation can compete and even overpower the otherwise dominant (for almost all other gases and inelastic processes) positronium (Ps) formation (Murphy and Surko 1992, Cassidy *et al* 2006, Clarke *et al* 2006, Sullivan *et al* 2008, Marjanović *et al* 2011, Danielson *et al* 2015). To be fair, the principles of the trap have been worked out in great detail, but mostly based on beam-like considerations (Murphy and Surko 1992, Charlton and Humberston 2000). However the device consists of a charge being released in a gas in the presence of electric and magnetic fields, and thus it is an ionized gas that is exactly described by a swarm model until the space charge effects begin to play a significant role, and then it is best described by a plasma model (again with a significant reference to collisions and transport). Thus, for quantitative representation and accurate modeling of traps, a swarm-like model is required and recently two such models were used to explain the salient features of Surko traps (Marjanović *et al* 2011, Petrović *et al* 2014, Natisin *et al* 2015). An explanation and quantitative comparisons will be the subject of a specialized publication (Marjanović and Petrović 2016). Here we only focus on the development of the energy distribution function, which is the primary medium connecting the large-scale behavior of the trap with microscopic binary collisions.

As pressures used in the gas-filled traps are very low, and the mean free paths become comparable to the dimensions of the trap, one may be assured that the description at the level of transport coefficients and fluid models would fail. This example thus requires a full kinetic level of description.

The generic (model) trap consists of three stages, each with a 10 V potential drop and each of the same length (figure 9). The properties, the pressures and other features are listed in table 1. A standard, well-tested (for electron benchmarks—Lucas and Saelee 1975, Reid 1979, Ness and Robson 1986, Raspopović *et al* 1999) Monte Carlo code has been used here. Realistic geometry was included along with the boundary conditions (potentials, energy distributions and losses). Special care was given to the testing of the modeling of trajectories in magnetic fields (Raspopović *et al* 1999 Dujko *et al* 2005).

First results are shown in figure 10 where we plot mean energies as a function of time in three separate stages (chambers) and also averaged for the entire volume. The energy steps provided by the potential drops are observable for the mean energies in stages II and III. The overall increase in energy is also observed in the total volume average. The initial plateau of the mean energy is extended mainly due to

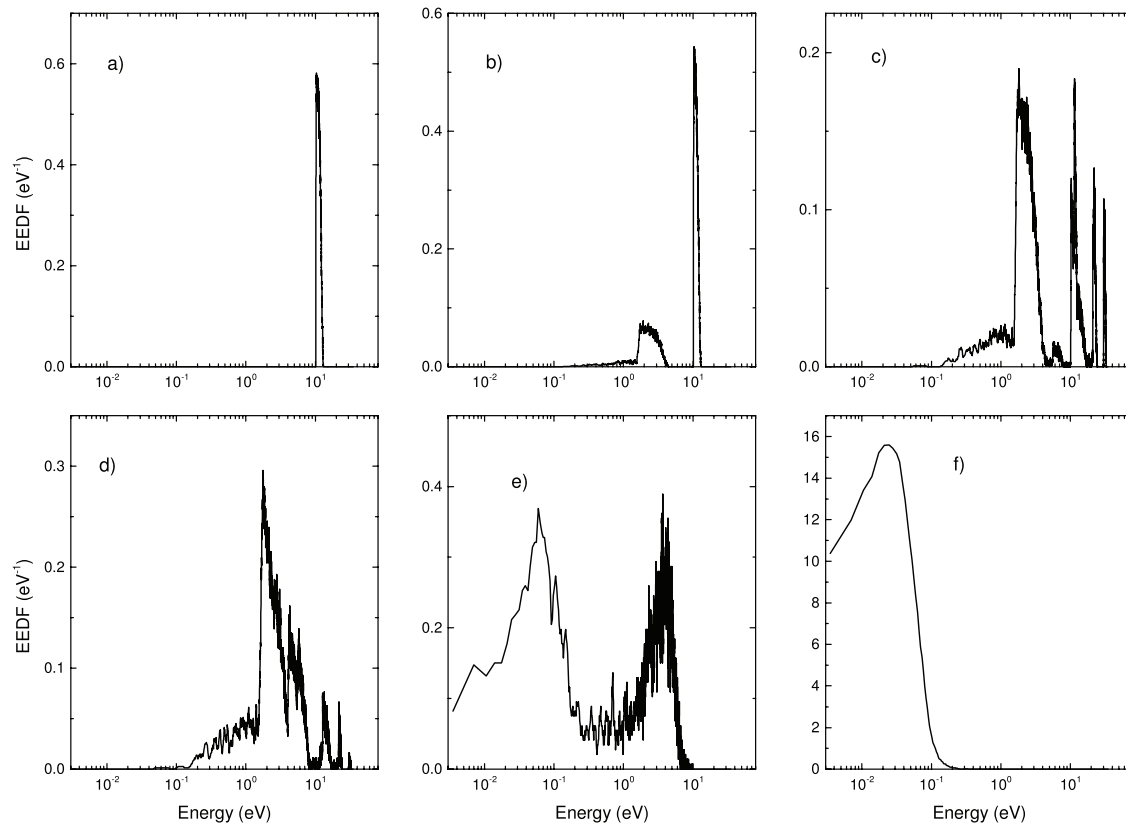


Figure 11. Positron kinetic energy distribution of the entire swarm sampled at different times (indicated in figure 10). Calculations were performed for the Surko trap as shown in figure 9 with the conditions listed in table 1.

the logarithmic nature of the plot. Following another plateau due to inelastic energy losses, the mean energy falls to the thermal value for the final thermalization.

The voltage drop in the initial stage is used to accelerate the positrons coming from the moderator into the energy range where electronic excitation of nitrogen is as efficient as Ps formation. Thus the initial distribution in figure 11 is a mono-energetic beam at 10 eV. Upon development of the group of positrons that have lost energy in excitation (figure 11(b)), positrons leave the stage I and pass into stages II and III so the two new peaks develop at 20 eV and 30 eV (figure 11(c)). The positrons that have collided form a group peaking at around 2 eV. During the next period two processes are obvious. The first is the quenching of the initial beams into the group, peaking at around 2 eV but extending up to 7 eV, where Ps formation removes the particles. The second is the process that uses vibrational excitation of CF_4 and thermalizes the 2 eV group into a low-energy group peaking at around 0.07 eV (figures 11(d) and (e)). It is interesting to see that the peak at around 2 eV is the first to disappear, leaving a group at around 5 eV to thermalize more slowly. At this point the low-energy positrons are also mainly localized in the third stage.

The final stage is characterized by two processes, the disappearance of the higher-energy group at around 5 eV and the gradual thermalization of the low-energy group at around 70 meV towards the thermal energy (*f*) of around 40 meV. At that point a quasi-thermal Maxwellian is developed. The transition appears to be rapid but, by the virtue of a logarithmic plot, it is the longest transition in the process of thermalization and

involves bouncing between the potential boundaries of the third stage many times. At the same time one should see that the properties of the trap are adjusted so that in the first bounce across the three stages most particles suffer electronic excitation/Ps formation collisions and either disappear or are trapped.

The simulation provides many different properties of the positron ensemble (swarm) but the point of this paper is to show a direct connection between binary collision processes and the macroscopic behavior. Using the energy distribution one can easily see the dominant processes and predict which aspects of the processes are promoted by the clever design of the Surko trap. It may also be used to optimize its characteristics (Marjanović *et al* 2016). Nevertheless, the principles of the trap were properly understood from the initial concepts but in this case we have detailed representation of the energy distribution, allowing accurate quantitative comparisons. For example, one may now adjust the details of the cross section in order to fit the measured properties (such as sampled mean energy that may be somewhat skewed by the sampling process). In that respect the measured observables from the trap may play a role in the swarm data that need to be fitted in order to tune the cross sections so that the number, momentum and energy balances may be preserved. As analysis of the positron swarm data led to a number of complex kinetic effects (Banković *et al* 2009, 2012) it would be interesting to see whether similar effects may be observed or even affect the operation of the traps.

These results are akin to the well-established initial equilibration for electrons in gases (Dujko *et al* 2014) with

temporal and spatial Holst Oosterhuis luminous layers (Hayashi 1982, Fletcher 1985) that are strongly related to the well-known Frank Hertz experiment (White *et al* 2012, Robson 2014). In addition, it must be noted that even if we were to start simulation with a Maxwellian distribution and try to follow the thermalization, due to the sharp energy dependence of the processes non-Maxwellian distribution function, it would develop immediately making it necessary to employ a full kinetic treatment. While fluid equations will not work well under the circumstances, and while transport coefficients may be difficult to define and even more difficult to implement in modeling, kinetic (Monte Carlo) modeling is still a typical swarm-like model that needs to be employed. Once we fill the trap with sufficient charge to allow for plasma effects, then we may need to add-in true plasma modeling based on fluid equations and on the calculation of the effective fields.

5. Conclusion

In this review we address three recent examples on how swarm based modeling may connect the microscopic binary processes to the macroscopic behavior of ionized gases, even plasmas. The necessary prerequisite for this approach to be effective is that the systems belong to the so-called collisional plasmas (also known as the non-equilibrium or low-temperature plasmas). The examples are chosen to reveal three different aspects of swarm modeling: (a) that based on transport coefficients and fluid models and how they may be improved, (b) a system that may be described by both fluid models and simulations where simulations are used here to verify the more basic modeling, while the fluid modeling is allowing us to extend predictions further to plasma conditions, and, finally, (c) for the situation where full kinetic modeling is required. Thus, these examples should be viewed as confirmation of the validity and usefulness of the swarm models that are often overlooked by plasma modelers. Swarm models are sometimes regarded as a limit that is unrealistic and useful only to describe well-designed experiments that provide swarm data. One subscribing to that view would then need to reply to why the use of swarm data and also swarm data based fluid equations is so successful. In fact, we believe that often an ‘overkill’ is performed by using plasma models to describe inherently swarm-like conditions. One such example is the popular modeling of breakdown by PIC of hybrid codes. If done properly, it is all fine, although less transparent due to a more complex nature of the codes. However, at the same time such complexity does not allow us to add special tests or sampling that may reveal more insight into the pertinent physical processes. Examples may include details of the energy distribution function, adjusting boundary conditions to include detailed representation of surface processes and observation and inclusion of the kinetic phenomena.

In doing modeling of low-temperature plasmas that may need to go both more towards the swarm-like and plasma conditions we would strongly recommend that all the plasma codes need to be verified against swarm benchmarks and

include sampling of relevant data. It all may become more and more difficult as one develops codes for inhomogeneous systems with complex geometry, but in the limit of a simple geometry and simple swarm conditions all swarm benchmarks should be satisfied to the highest of accuracy.

This article may be viewed as an extension of an article that has been recently submitted for a special issue on plasma modeling covering physical situations where swarm type models are valid and useful and accurate. There is no overlap of the two papers, although a common idea of the need to present the usefulness of the swarm model is obvious. The focus here is more on how elementary processes are producing an intermediate realm of phenomenology (swarm models and properties) that then clearly point at the macroscopic behavior. Be it sprite propagation or positron traps these connections not only reveal relevant physics, but also provide a means to tailor applications based on elementary processes and low-temperature plasmas.

Acknowledgment

This work was supported by the Grants No. ON171037 and III41011 from the Ministry of Education, Science and Technological Development of the Republic of Serbia and also by the project 155 of the Serbian Academy of Sciences and Arts.

References

- Banković A, Dujko S, White R D, Marler J P, Buckman S J, Marjanović S, Malović G, Garcia G and Petrović Z Lj 2012 *New J. Phys.* **14** 035003
- Banković A, Petrović Z Lj, Robson R E, Marler J P, Dujko S and Malović G 2009 *Nucl. Instrum. Methods Phys. Res. B* **267** 350–3
- Barut A O and Raczka R 1980 *Theory of Group Representations and Applications* (Warszawa, PWN: Polish Scientific Publishers)
- Blevin H A, Fletcher J and Hunter S R 1976 *J. Phys. D: Appl. Phys.* **9** 471
- Blevin H A, Fletcher J and Hunter S R 1978 *Aust. J. Phys.* **31** 299
- Bošnjaković D, Petrović Z Lj and Dujko S 2014b *J. Instrum.* **9** P09012
- Bošnjaković D, Petrović Z Lj and Dujko S 2016 *J. Phys. D: Appl. Phys.* **49** 405201
- Bošnjaković D, Petrović Z Lj, White R D and Dujko S 2014a *J. Phys. D: Appl. Phys.* **47** 435203
- Cassidy D B, Deng S H M, Greaves R G and Mills A P 2006 *Rev. Sci. Instrum.* **77** 073106
- Charlton M and Humberston J 2000 *Positron Physics* (New York: Cambridge University)
- Clarke J, van der Werf D P, Griffiths B, Beddows D C S, Charlton M, Telle H H and Watkeys P R 2006 *Rev. Sci. Instrum.* **77** 063302
- Danielson J R, Dubin D H E, Greaves R G and Surko C M 2015 *Rev. Mod. Phys.* **87** 247–306
- Denman C A and Schlie L A 1990 Nonequilibrium effects in ion and electron transport *Proc. of the 6th Int. Swarm Seminar (Glen Cove, NY, 1989)* ed J W Gallagher *et al* (New York: Springer)
- Dujko S, Markosyan A H, White R D and Ebert U 2013 *J. Phys. D: Appl. Phys.* **46** 475202
- Dujko S, Raspopović Z M and Petrović Z Lj 2005 *J. Phys. D: Appl. Phys.* **38** 2952–66

- Dujko S, Raspopović Z M, White R D, Makabe T and Petrović Z Lj 2014 *Eur. Phys. J. D* **68** 166
- Dujko S, White R D, Petrović Z Lj and Robson R E 2010 *Phys. Rev. E* **81** 046403
- Fletcher J 1985 *J. Phys. D: Appl. Phys.* **18** 221–8
- Hayashi M 1982 *J. Phys. D: Appl. Phys.* **15** 1411–8
- Hunter S R 1977 *PhD Thesis* Flinders University, Adelaide, Australia unpublished
- Koutselos A D 1997 *J. Chem. Phys.* **106** 7117–23
- Koutselos A D 2001 *Chem. Phys.* **270** 165–175
- Lippmann C and Riegler W 2004 *Nucl. Instrum. Methods Phys. Res. A* **533** 11–5
- Lucas J and Saelee H T 1975 *J. Phys. D: Appl. Phys.* **8** 640–50
- Marjanović S, Banković A, Cassidy D, Cooper B, Deller A, Dujko S and Petrović Z Lj 2016 *J. Phys. B: At. Mol. Opt. Phys.* **49** 215001
- Marjanovic S, Šuvakov M, Bankovic A, Savic M, Malovic G, Buckman S J and Petrovic Z Lj 2011 *IEEE Trans. Plasma Sci.* **39** 2614–5
- Marjanović S and Petrović Z Lj 2016 *Plasma Sources Sci. Technol.* submitted
- Moshaii A, Khosravi Khorashad L, Eskandari M and Hosseini S 2012 *Nucl. Instrum. Methods Phys. Res. A* **661** S168–71
- Murphy T J and Surko C M 1992 *Phys. Rev. A* **46** 5696–705
- Natisin M R, Danielson J R and Surko C M 2015 *Phys. Plasmas* **22** 033501
- Ness K F, Robson R E 1986 *Transp. Theor. Stat. Phys.* **14** 257–90
- Penetrante B M and Bardsley J N 1990 *Nonequilibrium Effects in Ion and Electron Transport* ed J W Gallagher et al pp 49–66 (New York: Plenum)
- Petrović Z Lj, Dujko S, Marić D, Malović G, Nikitović Ž, Šašić O, Jovanović J, Stojanović V and Radmilović-Rađenović M 2009 *J. Phys. D: Appl. Phys.* **42** 194002
- Petrović Z Lj et al 2014 *J. Phys.: Conf. Ser.* **488** 012047
- Raspopović Z M, Sakadžić S, Bzenić S and Petrović Z Lj 1999 *IEEE Trans. Plasma Sci.* **27** 1241–8
- Reid I D 1979 *Aust. J. Phys.* **32** 231–54
- Robson R E, White R D and Hildebrandt M 2014 *Euro. Phys. J. D* **68** 188
- Robson R E, White R D and Petrović Z Lj 2005 *Rev. Mod. Phys.* **77** 1303
- Santonico R 2012 *Nucl. Instrum. Methods Phys. Res. A* **661** S2–5
- Simonović I et al 2016 unpublished
- Šašić O, Malović G, Strinić A, Nikitović Ž and Petrović Z Lj 2004 *New J. Phys.* **6** 74–85
- Sullivan J P, Jones A, Caradonna P, Makochekanwa C and Buckman S J 2008 *Rev. Sci. Instrum.* **79** 113105
- Wheaton J H and Mason E A 1974 *Ann. Phys.* **84** 8–38
- White R D, Robson R E, Nicoletopoulos P and Dujko S 2012 *Eur. Phys. J. D* **66** 117
- The ATLAS Collaboration 2008 *J. Instrum.* **3** S08003
- Tung W-K 1984 *Group Theory in Physics* (Singapore: World Scientific Publishing)
- Vrhovac S B, Petrović Z Lj, Viehland L A and Santhanam T S 1999 *J. Chem. Phys.* **110** 2423–30

Fluid modeling of resistive plate chambers: impact of transport data on development of streamers and induced signals

D Bošnjaković¹, Z Lj Petrović^{1,2} and S Dujko¹

¹ Institute of Physics, University of Belgrade, Pregrevica 118, 11080 Belgrade, Serbia

² Serbian Academy of Sciences and Arts, Knez Mihailova 35, 11001 Belgrade, Serbia

E-mail: dbosnjak@ipb.ac.rs

Received 13 May 2016, revised 29 July 2016

Accepted for publication 12 August 2016

Published 9 September 2016



Abstract

We discuss the implementation of transport data in modeling of resistive plate chambers (RPCs), which are used for timing and triggering purposes in many high energy physics experiments. Particularly, we stress the importance of making a distinction between flux and bulk transport data when non-conservative collisions, such as attachment and/or ionization, are present. A 1.5-dimensional fluid model with photoionization is employed to demonstrate how the duality of transport data affects the calculated signals of the ATLAS triggering RPC and ALICE timing RPC used at CERN, and also a timing RPC with high SF₆ content. It is shown that in the case of timing RPCs, the difference between the induced charges calculated using flux and bulk transport data can reach several hundred percent at lower operating electric fields. The effects of photoionization and space charge are also discussed.

Keywords: resistive plate chambers, fluid models, electron avalanche, streamers, photoionization, C₂H₂F₄

(Some figures may appear in colour only in the online journal)

1. Introduction

Introduced in the 1980s [1, 2], resistive plate chambers (RPCs) became widely used particle detectors for large area timing and triggering purposes in high energy physics experiments [3–5]. They consist of one or many gas gaps between electrodes of high resistivity such as glass or bakelite. Owing to their low cost, good efficiency and outstanding timing resolution [6, 7], RPCs found their way into other areas of fundamental physics and technology, including cosmic ray physics [8], geophysics [9] and medical imaging [10].

There have been many approaches to modeling of RPCs. Analytical methods [11, 12], while often approximate, can provide general conclusions about the influence of various parameters on the RPC performance. Monte Carlo simulations [13–15] are useful for calculating RPC performance characteristics, such as timing resolution and efficiency, which depend on the stochastic nature of primary ionization and electron avalanche development. On the other hand,

numerical models based on fluid equations [16, 17] can only provide the mean values of RPC signals. Still, they are frequently used for studying various physical phenomena in RPC operation, in a computationally efficient manner.

All RPC models, except the microscopic Monte Carlo model [15], rely on accurate electron transport and reaction data in gases [18]. These data can be obtained from swarm experiments [19, 20] but are usually calculated from the electron impact cross sections using either the Monte Carlo technique [21, 22] or Boltzmann equation analysis [23–25]. MAGBOLTZ [26] is a Monte Carlo tool for such a task and is routinely used by the particle detector community. However, there seems to be a lack of awareness of the two types of transport data named ‘flux’ and ‘bulk’ [19, 27]. The difference between the two can be elucidated by the explicit effects of non-conservative collisions. Every collision which results in changing of the number of electrons in the ensemble (e.g. ionization, attachment, electron–ion recombination) is regarded as non-conservative. In RPC

modeling, flux data were assumed systematically. Still, to our knowledge, MAGBOLTZ can compute the bulk data and considers them as ‘time of flight’ data, in the framework of the so-called ‘Tagashira convention’ [28]. Furthermore, most swarm experiments measure bulk properties [19, 25] and as of recently, BOLSIG + [29]—a publicly available two term Boltzmann equation solver—can also compute the bulk data. Differences between two sets of data are often significant, ranging from a few percent to a few orders of magnitude. In some cases, bulk and flux transport coefficients may exhibit entirely different qualitative behavior, as in case of negative absolute electron flux mobility [30] in mixtures of noble and strongly attaching gases and negative differential conductivity (NDC) for electron bulk drift velocity in strongly attaching gases [31]. A question may be raised as to which data, under which conditions, are appropriate in modeling of RPCs. The aim of this paper is to discuss this issue and also to demonstrate the difference one might induce by implementation with the bulk and flux data in fluid modeling of RPCs. With that motivation, we have developed a fluid model based on a drift-diffusion equation in a 1.5-dimensional framework. This numerical model is also used to investigate streamer development in RPCs under the influence of space charge effects and photoionization. Particularly, we focus on the signal formation in three RPC configurations with different SF₆ content, where duality of transport data should not be neglected.

In the present paper, we extend the previous fluid-equation based models of RPCs [16, 17] by including the diffusion term in the fluid model. In addition to ATLAS triggering RPC, we present what we believe to be the first systematic calculation of the induced signals in the ALICE timing RPC and timing RPC [32] for a wide range of the applied electric fields. Electron transport coefficients as a function of the reduced electric field are required as input in fluid equations. A Monte Carlo simulation technique is used to calculate these transport coefficients in the gas mixtures considered in this work. In particular, a new set of cross sections for electron scattering in C₂H₂F₄ is developed and considered in the calculations.

This paper is organized as follows. In section 2.1 we give a brief overview and theoretical basis of electron transport in gases under the hydrodynamic assumption and highlight those aspects relevant for modeling. The numerical model used to study the signal formation in ATLAS triggering RPC, ALICE timing RPC and timing RPC [32] is described in section 2.3. Calculated transport data used as input in this model are presented in section 2.2. Finally, in section 3 we show how different transport data affect the calculated signals for the three RPC configurations.

2. Theoretical methods

2.1. Hydrodynamic modeling of electron transport in gases

The starting point of our electron transport analysis is the equation of continuity

$$\frac{\partial n_e(\mathbf{r}, t)}{\partial t} + \nabla \cdot \mathbf{\Gamma}(\mathbf{r}, t) = S(\mathbf{r}, t), \quad (1)$$

where $n_e(\mathbf{r}, t)$ is the electron number density, $\mathbf{\Gamma}(\mathbf{r}, t) = n_e \langle \mathbf{v} \rangle$ is the electron flux, $\langle \mathbf{v} \rangle$ is the average electron velocity and $S(\mathbf{r}, t)$ represents the electron production rate per unit volume arising from non-conservative collisions. Away from electrodes, sources and sinks of electrons, the hydrodynamic conditions can be assumed [22, 33]. Under these conditions, the phase-space distribution function can be expressed as

$$f(\mathbf{r}, \mathbf{v}, t) = \sum_{k=0}^{\infty} f^{(k)}(\mathbf{v}) \odot (-\nabla)^k n_e(\mathbf{r}, t), \quad (2)$$

where $f^{(k)}(\mathbf{v})$ are tensors of rank k and \odot denotes a k -scalar product. This functional relationship, which is valid for weak gradients, is known as the hydrodynamic approximation [33]. Using the expansion (2), after truncation, the flux $\mathbf{\Gamma}(\mathbf{r}, t)$ and source term $S(\mathbf{r}, t)$ in the continuity equation (1) can be written as

$$\mathbf{\Gamma}(\mathbf{r}, t) = \mathbf{W}_F n_e(\mathbf{r}, t) - \mathbf{D}_F \cdot \nabla n_e(\mathbf{r}, t), \quad (3)$$

$$S(\mathbf{r}, t) = S^{(0)} n_e(\mathbf{r}, t) - \mathbf{S}^{(1)} \cdot \nabla n_e(\mathbf{r}, t) + \mathbf{S}^{(2)} : \nabla \nabla n_e(\mathbf{r}, t), \quad (4)$$

where \mathbf{W}_F is the flux drift velocity and \mathbf{D}_F is the flux diffusion tensor. Substituting the expressions for the flux (3) and source term (4) into the continuity equation (1) we obtain

$$\frac{\partial n_e(\mathbf{r}, t)}{\partial t} + \nabla \cdot (\mathbf{W}_B n_e(\mathbf{r}, t) - \mathbf{D}_B \cdot \nabla n_e(\mathbf{r}, t)) = S^{(0)} n_e(\mathbf{r}, t), \quad (5)$$

where

$$\mathbf{W}_B = \mathbf{W}_F + \mathbf{S}^{(1)} \quad (\text{bulk drift velocity}), \quad (6)$$

$$\mathbf{D}_B = \mathbf{D}_F + \mathbf{S}^{(2)} \quad (\text{bulk diffusion tensor}). \quad (7)$$

The equation (5) is strictly valid only when $\nabla \mathbf{S}^{(1)} n_e - \nabla \mathbf{S}^{(2)} \nabla n_e = 0$. This assumption holds when the electric field is spatially homogeneous as in the avalanche phase of streamer development in RPCs. It is possible to avoid this assumption, and this analysis is deferred to a future paper. Our preliminary results, obtained under conditions found in RPCs suggest that equation (5) is valid even for the streamer phase where the space charge effects control the electric field. From definitions (6) and (7), it is evident that the difference between the flux and bulk transport coefficients arises only due to presence of non-conservative collisions. It is shown [33, 34] that the bulk drift velocity can also be defined as

$$\mathbf{W}_B = \frac{d}{dt} \langle \mathbf{r} \rangle, \quad (8)$$

and the bulk diffusion tensor as

$$\mathbf{D}_B = \frac{1}{2} \frac{d}{dt} \langle \mathbf{r}^* \mathbf{r}^* \rangle. \quad (9)$$

Here $\mathbf{r}^* = \mathbf{r} - \langle \mathbf{r} \rangle$ where $\langle \mathbf{r} \rangle$ is the mean position of the swarm. Similarly, the flux drift velocity components and the flux diagonal elements of the diffusion tensor are defined as

$$\mathbf{W}_F = \left\langle \frac{d\mathbf{r}}{dt} \right\rangle = \langle \mathbf{v} \rangle, \quad (10)$$

$$\mathbf{D}_{F,ii} = \langle \mathbf{r}_i \mathbf{v}_i \rangle - \langle \mathbf{r}_i \rangle \langle \mathbf{v}_i \rangle, \quad (11)$$

where $\langle \mathbf{v}_i \rangle$ is the mean electron velocity and $i = x, y, z$. The definitions (8)–(11) are useful for direct sampling in Monte Carlo simulations. Also, the electron production rate $S^{(0)}$ can be calculated as

$$S^{(0)} = \frac{1}{N_e} \frac{dN_e}{dt}, \quad (12)$$

where $N_e(t)$ is the number of electrons in the swarm.

One should be aware of the differences between the bulk drift velocity and flux drift velocity. The bulk drift velocity (8) is the velocity of centre of mass of the swarm, while the flux drift velocity (10) is the mean velocity of electrons. It can be easily illustrated why the two velocities may differ in presence of non-conservative collisions. Even under hydrodynamic conditions, in constant electric field, the mean energy of electrons is not constant throughout the swarm [24, 25, 31]. Electrons at the front of the swarm generally have higher energy than those at the back. If the collision frequency for ionization increases with the electron energy, then electrons are predominantly created in regions of higher energy, resulting in a shift of the centre of mass of the swarm. A similar physical picture can be applied for electron attachment: if there is an attachment process which occurs at higher collision energies, it will naturally tend to affect the leading edge of the swarm. This results in a backwards shift of the swarm's centre of mass, which is observable as a reduction of the bulk drift velocity (as compared to the flux drift velocity). This process is known as attachment cooling [35, 36]. Conversely, if collision frequency for electron attachment decreases with the electron energy, then it is more likely that electrons will be more efficiently consumed at the back than on the leading edge of the swarm. This in turn shifts the swarm's centre of mass forward. This phenomenon is observable as an increase of the bulk drift velocity and is usually known in the literature as attachment heating [35, 36]. The distinction between the two velocity components has important implications in modeling of electron avalanches. One should take into account that the avalanche (i.e. its centre of mass) progresses in space with bulk drift velocity. For example, when Legler's model [37], or any other model of avalanche fluctuations is employed as a function of avalanche path length [14, 38], bulk drift velocity should be used to evaluate the ionization and attachment coefficients.

Transport quantities (8)–(12) can be considered as fundamental data. They are strictly defined under hydrodynamic conditions and are not an artifact of a particular theoretical model or method of analysis. They are measurable and independent of the experimental arrangement. Most swarm experiments involve determination of bulk transport properties. Typical examples are the pulsed-Townsend experiment and time-of-flight experiment [19, 27]. These experiments assume hydrodynamic conditions, which means that the measured quantities correspond to the bulk properties appearing in the diffusion equation (5). The bulk transport properties can be used to normalize the sets of cross sections using the so-called swarm procedure. The normalized set of cross sections for electron scattering provides transport and reaction data

which are in a good agreement with the measured data. The standard swarm procedure was used by our group with the aim of deriving the cross sections for electron scattering $C_2H_2F_4$ (section 2.2). As a result of this procedure, the calculated transport coefficients agree very well with those measured under the pulsed-Townsend conditions [39, 40].

Equation (5) coupled with the Poisson equation using a local field approximation forms the basis of the fluid model considered in this work. Local field approximation assumes that the electrons are in equilibrium with the local electric field and thus the properly defined transport coefficients are only functions of the local electric field. The equation (5) also assumes hydrodynamic conditions and the approximation concerning the source term. However, for homogeneous electric field, this model gives the correct avalanche velocity and ionization per avalanche path length. The same might not be true for fluid models of RPCs [16–18] where the type of transport data used as input is not discussed. Equation (5) with flux transport coefficients instead of bulk, forms the basis of the first-order fluid model. The designation 'first-order' implies that it can be derived from the Boltzmann transport equation using first-order velocity moments of the phase-space distribution function and several approximations [41]. In general, fluid models can be derived as moment equations of the variable order but they usually require many simplifying and closure assumptions. For example, the fluid model of the second-order is truncated at the level of the mean energy where fluid equations are closed in the so-called local mean energy approximation [41, 42]. Higher-order models introduce even more equations and have been used for studying the non-local effects in streamer dynamics [41, 42]. The application of high-order fluid models for analysis of RPCs is a subject of our forthcoming paper. In this paper, however, we only consider the first-order model with flux transport data and model based on equation (5) with bulk transport data. Since both models are mathematically the same, with the only difference being the transport data used as input, we shall refer to them as a single model which uses either flux or bulk transport data.

2.2. Electron transport data in RPC gases

In this section we present the calculated transport and rate coefficients for fluid modeling of the three RPC configurations. The data are calculated using our Monte Carlo technique based on tracking of individual electrons and their collisions with the background gas. We assume that the electron scattering is isotropic for each type of collision. While the inclusion of anisotropy of electron scattering is important for modeling of the transport and discharges in some molecules under mostly high energy conditions no such conditions were found in the present work that would justify the need to include the differential cross sections and also that would be supported by the available data to a sufficient degree. The background gas temperature is set to 293 K. The transport coefficients are sampled using definitions (8)–(11). For more details about our Monte Carlo code the reader is referred to [21, 34, 43].

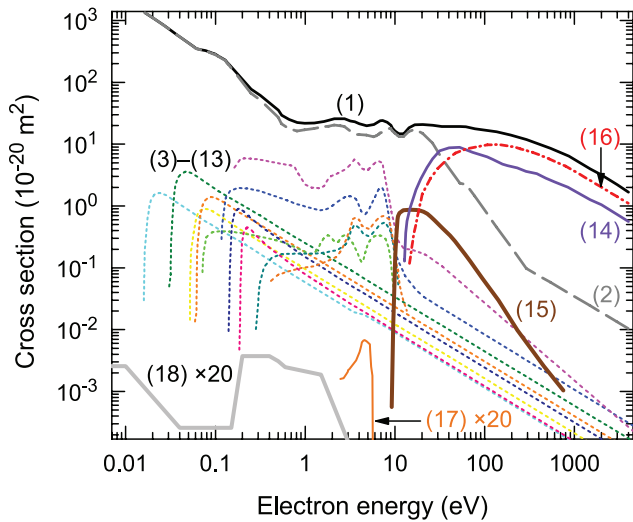


Figure 1. Cross sections for electron scattering in $C_2H_2F_4$ [44]: (1) total momentum transfer, (2) elastic momentum transfer, (3)–(13) vibrational excitations, (14) dissociative excitation, (15) effective electronic excitation, (16) ionization, (17) dissociative attachment, (18) 3-body attachment assuming pressure of 1 atm and temperature of 293 K. For display, the attachment cross sections (17) and (18) are multiplied by factor 20.

The transport and rate coefficients are calculated for gas mixtures employed in: (1) ATLAS triggering RPC [3] 94.7% $C_2H_2F_4$ + 5% iso- C_4H_{10} + 0.3% SF_6 , (2) ALICE timing RPC [4] 90% $C_2H_2F_4$ + 5% iso- C_4H_{10} + 5% SF_6 , and (3) timing RPC [32] 85% $C_2H_2F_4$ + 5% iso- C_4H_{10} + 10% SF_6 . The data are calculated using a new cross section set for electron scattering in $C_2H_2F_4$ (figure 1) developed by our group [44]. This cross section set is based on an updated version of our previous set [45] with additional vibrational excitations, electronic excitation and three-body attachment. The transport and rate coefficients obtained using this set are in good agreement with measurements by Urquijo *et al* [40] and Basile *et al* [39]. The cross sections for iso- C_4H_{10} are taken from MAGBOLTZ 7.1. There is an updated set for iso- C_4H_{10} in newer versions of MAGBOLTZ but the ionization coefficient obtained using the older set from MAGBOLTZ 7.1 is in better agreement with measurements [46]. Finally, the cross section set for electron scattering in SF_6 is taken from Itoh *et al* [47].

Figure 2 shows the flux and bulk drift velocities calculated over a range of reduced electric field strengths for three RPC gas mixtures. The reduced electric field E/N is expressed in Td ($1 \text{ Td} = 10^{-21} \text{ Vm}^2$). We observe that the ALICE timing RPC and timing RPC [32] gas mixtures exhibit the greatest overall difference between bulk and flux components of drift velocity. The difference is larger than two orders of magnitude in the limit of the lowest fields considered in this work (1–3 Td) and an order of magnitude between 10–30 Td. In both of these E/N ranges we see that the bulk drift velocity is reduced for an increasing E/N . This phenomenon is termed negative differential conductivity (NDC) and has been studied many times in the past [48, 49]. In particular, the occurrence of NDC in the bulk drift velocity in the ALICE timing RPC gas mixture has already been investigated in [31]. Still, the largest differences between the flux and bulk components are in the attachment

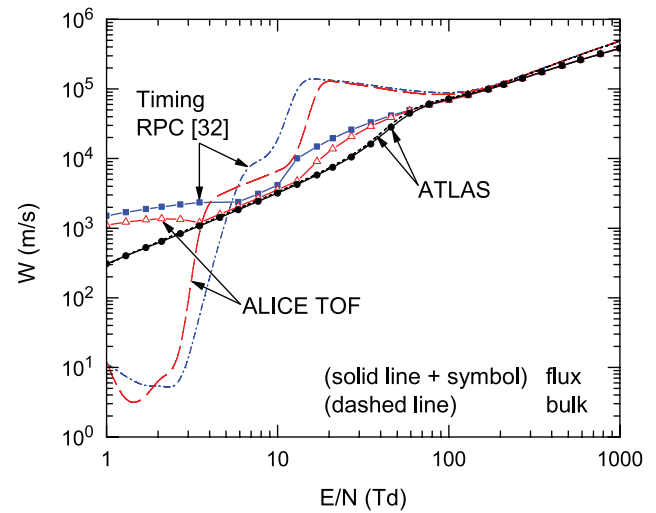


Figure 2. Bulk and flux drift velocities calculated for gas mixtures used in ATLAS triggering RPC, ALICE timing RPC and timing RPC [32].

dominated region below 100 Td (figure 3). In the ionization dominated region, at RPC operating fields of 200–400 Td, the difference ranges between 5% and 15%. A similar behavior is observed in the longitudinal component of the diffusion tensor (figure 4).

2.3. Numerical model

Assuming one-dimensional scenario $n_e(\mathbf{r}, t) = n_e(x, t)$ and the electric field $\mathbf{E} = E \mathbf{e}_x$ (where \mathbf{e}_x is the unit vector in the x direction), with addition of the photoionization source term (S_{ph}), the equation (5) reduces to

$$\frac{\partial n_e}{\partial t} = \frac{\partial}{\partial x} \left(W \operatorname{sgn}(E) n_e + D_L \frac{\partial n_e}{\partial x} \right) + (\nu_i - \nu_a) n_e + S_{ph}, \quad (13)$$

where ν_i and ν_a are the ionization and attachment frequencies (figure 3) respectively. The drift velocity W is defined as positive (figure 2) and $\operatorname{sgn}(E)$ is the sign (signum) function. Both transport and reaction data are considered as functions of $|E(x, t)|$. The continuity equations for the number densities of positive (n_p) and negative ions (n_n) are written as

$$\frac{\partial n_p}{\partial t} = \nu_i n_e + S_{ph} \quad \text{and} \quad \frac{\partial n_n}{\partial t} = \nu_a n_e, \quad (14)$$

since the ions can be considered as immobile on the timescale of fast electron signals.

The electric field is calculated assuming that the charge is contained inside a cylinder, with radius R_0 along the x axis, and distributed uniformly in the radial direction. In this case, similar to [50], the electric field along the x axis is given by

$$E(x, t) = E_0 + \frac{e_0}{2\epsilon_0} \int_0^d (n_p(x', t) - n_n(x', t) - n_e(x', t)) \cdot \left(\operatorname{sgn}(x - x') - \frac{x - x'}{\sqrt{(x - x')^2 + R_0^2}} \right) dx', \quad (15)$$

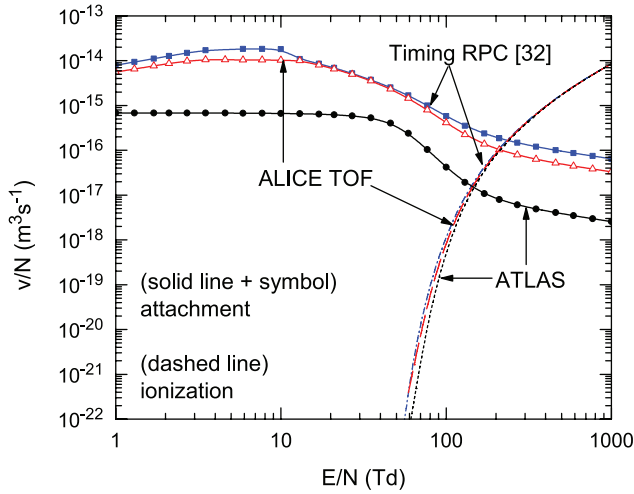


Figure 3. Ionization and attachment rate coefficients calculated for gas mixtures used in ATLAS triggering RPC, ALICE timing RPC and timing RPC [32].

where E_0 , d , e_0 and ε_0 are the external (applied) electric field, gas gap length, elementary charge and vacuum permittivity respectively.

The photoionization source term is defined as [51, 52]

$$S_{\text{ph}}(x, t) = \frac{M}{2\lambda} \int_0^d \nu_i(|E(x', t)|) n_e(x', t) \Omega(x - x') \cdot \exp\left(-\frac{|x - x'|}{\lambda}\right) dx', \quad (16)$$

where factor $M \equiv Q\nu_{\text{ph}}/\nu_i$ is the global photoionization efficiency. As an approximation, the model assumes that the photon production frequency ν_{ph} is proportional to the ionization frequency ν_i . The photon mean free path λ and the photoionization quantum efficiency Q are considered as effective values, averaged over the relevant photoemission bands. The function

$$\Omega(x - x') = \frac{1}{2} \left(1 - \frac{|x - x'|}{\sqrt{(x - x')^2 + R_0^2}} \right), \quad (17)$$

represents fraction of the solid angle centred at the emission point x' and covering the cross section area at x .

Equations (13) and (14) are solved numerically, imposing boundary conditions for absorbing electrodes

$$n_e(x = 0, t) = 0, \quad n_e(x = d, t) = 0, \quad (18)$$

and initial conditions

$$n_e(x, t = 0) = \frac{N_{e0}}{\pi R_0^2 \sigma_0 \sqrt{2\pi}} \exp\left(-\frac{(x - x_0)^2}{\sigma_0^2}\right), \quad (19)$$

$$n_p(x, t = 0) = n_e(x, t = 0), \quad n_n(x, t = 0) = 0. \quad (20)$$

Here N_{e0} is the initial number of electrons with Gaussian distribution centered at x_0 and standard deviation σ_0 . The numerical scheme uses second-order central finite differences for discretization of spatial derivatives and classical fourth-order Runge–Kutta 4 scheme for integration in time. With such an

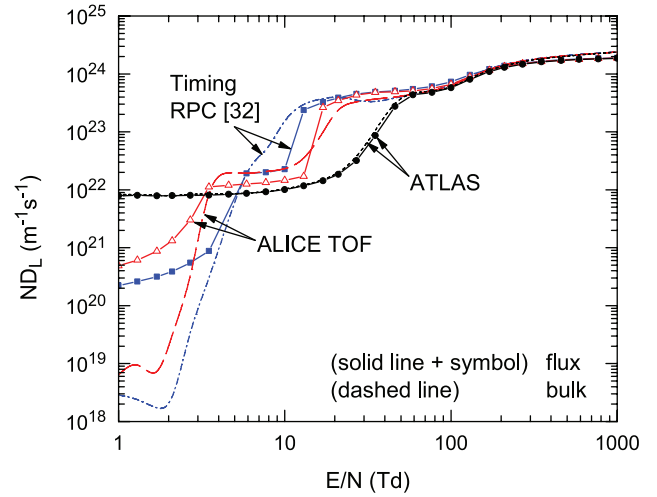


Figure 4. Bulk and flux density-normalized longitudinal diffusion coefficient calculated for gas mixtures used in ATLAS triggering RPC, ALICE timing RPC and timing RPC [32].

explicit method there are at least two stability conditions for the time step [53]:

$$\Delta t < C_a \Delta x / W \quad (\text{CFL condition}), \quad (21)$$

$$\Delta t < C_d (\Delta x)^2 / D_L \quad (\text{explicit diffusion limit}), \quad (22)$$

where Δx is the spatial grid step. C_a and C_d are the maximum Courant numbers for advection and diffusion equations [54], which generally depend on the particular time integration scheme and spatial discretization. In our calculations, we use a small constant time step which meets the above criteria.

Finally, the induced current is calculated using Ramo's theorem [55]

$$i(t) = e_0 \pi R_0^2 \frac{E_w}{V_w} \int_0^d n_e(x, t) W_F(|E(x, t)|) \text{sgn}(E(x, t)) dx, \quad (23)$$

where E_w/V_w is the weighting field and W_F is the flux drift velocity [27].

3. Results and discussion

3.1. Preliminaries

The results for three RPC configurations considered in this section are obtained using the model described in section 2.3. Electron transport data required by this model are presented in section 2.2. Parameter values for the radius of cylindrical charge distribution R_0 , photon mean free path λ and photoionization factor M , should generally require careful consideration. For example, the ‘range’ of the space charge field depends on R_0 which, on the other hand, is determined by the lateral spread of the primary ionization and transverse diffusion. Also, photoionization is a complex process, especially in the case of these RPC gas mixtures, and cannot be fully described by the effective parameters introduced in section 2.3. However, it is not the aim of this work to model the exact experimental conditions. The values for these parameters

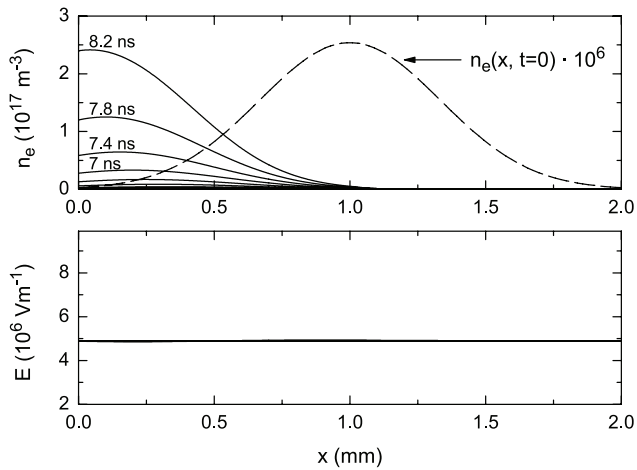


Figure 5. Electron number density and electric field during avalanche development in ATLAS triggering RPC (0–8.2 ns in steps of 0.4 ns). The applied electric field $E_0 = 4.9 \text{ MV m}^{-1}$ (196 Td) is oriented in the x direction.

are taken from [51], since they seem realistic: $R_0 = 0.3 \text{ mm}$, $\lambda = 500 \text{ }\mu\text{m}$ and $M = 10^{-6}$.

Other parameters—gas gap length d , number of spatial cells m , initial number of electrons N_{e0} —are specific for each RPC configuration:

- (i) ATLAS triggering RPC [3] with a gas mixture of 94.7% $\text{C}_2\text{H}_2\text{F}_4$ + 5% iso- C_4H_{10} + 0.3% SF_6 ($d = 2 \text{ mm}$, $m = 3000$, $N_{e0} = 60$).
- (ii) A single gas gap of the ALICE timing RPC [4] with a gas mixture of 90% $\text{C}_2\text{H}_2\text{F}_4$ + 5% iso- C_4H_{10} + 5% SF_6 ($d = 0.25 \text{ mm}$, $m = 2000$, $N_{e0} = 6$).
- (iii) Timing RPC [32] with a gas mixture of 85% $\text{C}_2\text{H}_2\text{F}_4$ + 5% iso- C_4H_{10} + 10% SF_6 ($d = 0.3 \text{ mm}$, $m = 2000$, $N_{e0} = 9$).

Numbers for N_{e0} correspond to approximately 10 primary clusters mm^{-1} and 3 electrons/cluster, which are realistic average values. We assume that the initial electron distribution is a Gaussian (19) centred in the gas gap i.e. $x_0 = d/2$, with $\sigma_0 = d/6$. For simplicity, the weighting field is set to $E_w/V_w = 1/d$ as in the parallel plate chamber. We assume that the gas number density $N = 2.505 \cdot 10^{25} \text{ m}^{-3}$, which corresponds to the pressure of 1 atm and temperature of 293 K.

3.2. Electron avalanche and streamer development

We now consider the electron avalanche and streamer development in ATLAS triggering RPC. The applied electric field $E_0 = 4.9 \text{ MV m}^{-1}$ ($E_0/N = 196 \text{ Td}$) is oriented along the x -axis and corresponds to the operating point voltage $U = 9.8 \text{ kV}$ [3]. Bulk transport data are employed in the model. The initial conditions assume 60 electrons with Gaussian distribution, as described in sections 2.3 and 3.1.

During the first 8.2 ns (figure 5), the electron avalanche exhibits typical exponential growth without noticeable space charge effects. Still, about half of the electrons have reached the anode. While electrons are being consumed at the anode the ions remain immobile. As a result, the space charge field

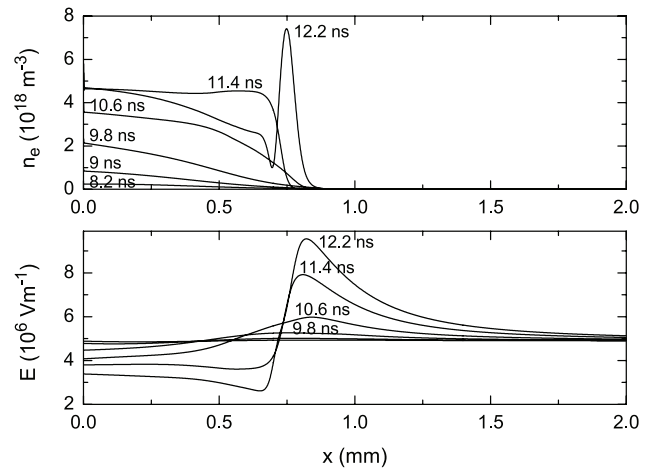


Figure 6. Electron number density and electric field during positive streamer formation in ATLAS triggering RPC (8.2–12.2 ns in steps of 0.8 ns). The applied electric field $E_0 = 4.9 \text{ MV m}^{-1}$ (196 Td) is oriented in the x direction.

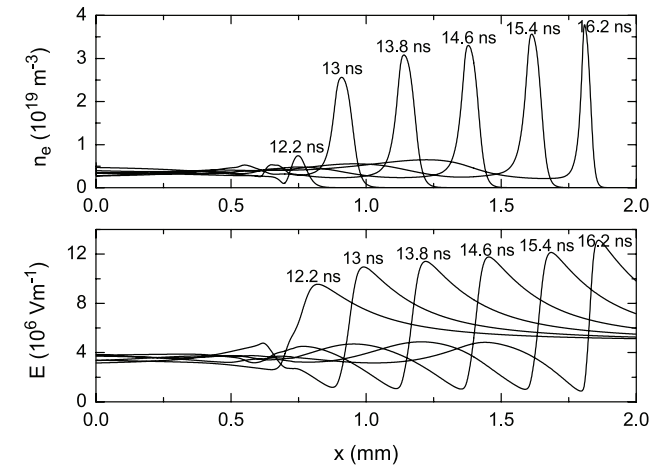


Figure 7. Electron number density and electric field during positive streamer propagation in ATLAS triggering RPC (12.2–16.2 ns in steps of 0.8 ns). The applied electric field $E_0 = 4.9 \text{ MV m}^{-1}$ (196 Td) is oriented in the x direction.

begins to grow and reaches 10% of the external field at about 10.6 ns (figure 6). Due to space charge, the external field is suppressed near the anode and enhanced at the tail of electron distribution. In this region of enhanced field a positive streamer is formed as a peak in the electron distribution (12.2 ns). At this moment, the space charge field reaches almost 100% of the external field, leading to high photon production. Due to photoionization, the positive streamer progresses toward the cathode (figure 7). After about 16.2 ns, the streamer peak becomes narrower and starts to diminish slowly.

The development of the electron avalanche and streamer is tightly related to the induced current, which is considered in the next section. It is interesting to note that in this case of ATLAS triggering RPC, but also in other RPC configurations considered in this work, the enhancement of the electric field which leads to the positive streamer formation is mainly due to electron absorption effect of the anode. A similar behavior was also observed in a parallel plate chamber [51].

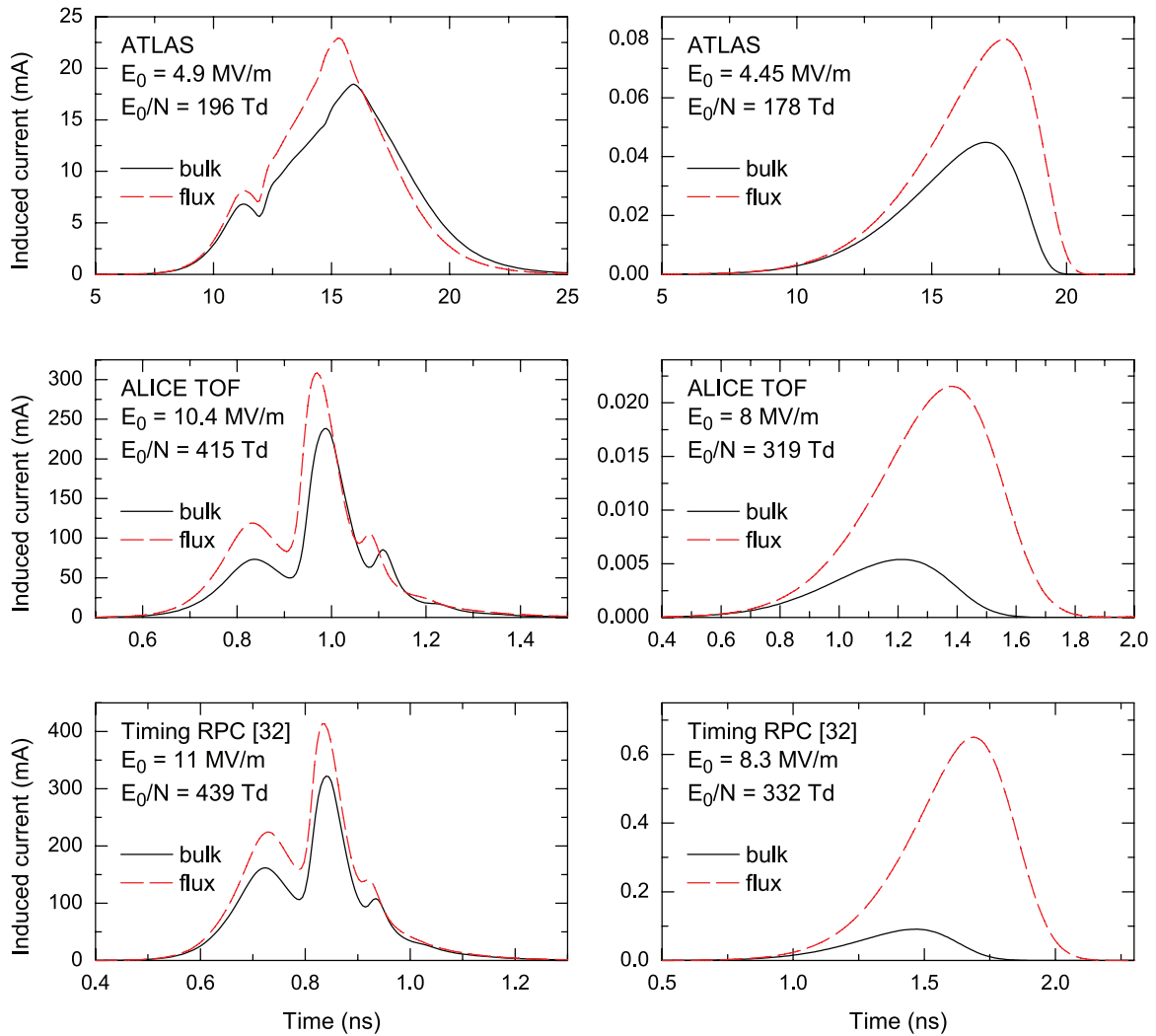


Figure 8. Induced signals in ATLAS triggering RPC, ALICE timing RPC (ALICE TOF) and timing RPC [32] calculated using flux and bulk transport data. Calculations are made for different applied electric fields E_0 : realistic operating fields (left) and low operating fields leading to saturated avalanche without positive streamer formation (right).

3.3. Induced current

Figure 8 (top left, solid line) shows the induced current calculated for the case of ATLAS triggering RPC discussed in section 3.2. We observe a small precursor signal followed by a large peak. The occurrence of the precursor was also noticed in many experiments [56–58]. According to equation (23), the signal development can be interpreted knowing the electron number density and flux drift velocity. In our case, the flux drift velocity increases monotonically with the electric field strength (figure 2). We now recall the characteristic time intervals for the avalanche development (0–8.2 ns), streamer development (8.2–12.2 ns) and positive streamer propagation (12.2–16.2 ns) described by the electron number density and electric field strength in figures 5–7 respectively. During the avalanche phase, the induced current grows exponentially until the electrons reach the anode. Eventually, the exponential rise stops and becomes linear due to both electron absorption and space charge effects, which begin at about 10 ns. The induced current peaks at 11.3 ns and starts to drop off forming the characteristic precursor shape. Another rise begins when

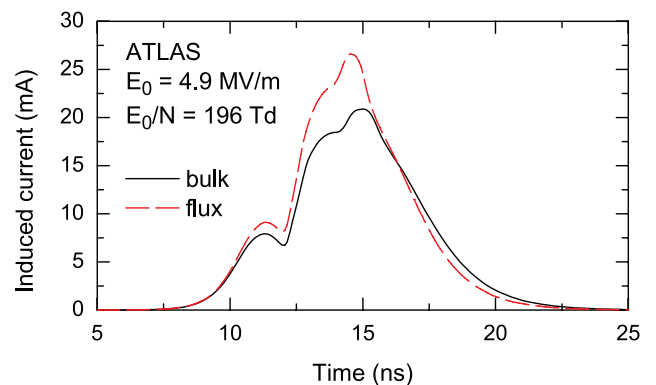


Figure 9. Induced signal in ATLAS triggering RPC calculated assuming the initial electron distribution with 10 equally spaced Gaussian clusters per mm, and 3 electrons per cluster. Calculations are made using flux and bulk transport data.

photoionization takes place in the region of enhanced electric field. The positive streamer is formed at 12.2 ns and the current rises while the positive streamer grows and propagates toward the cathode. At 16.2 ns the positive streamer stops

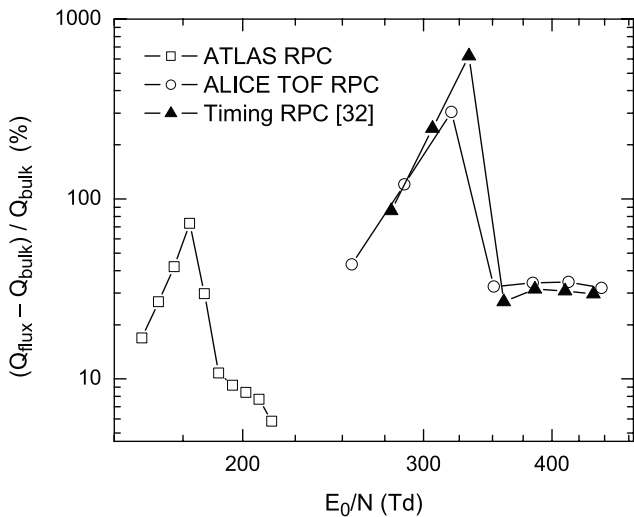


Figure 10. Percentage difference between the induced charges Q_{flux} and Q_{bulk} , calculated over a range of applied electric fields for ATLAS triggering RPC, ALICE timing RPC (ALICE TOF) and timing RPC [32].

right before reaching the cathode and starts to diminish, while the induced current slowly drops to zero.

The induced current for the ATLAS RPC calculated using flux transport data is also shown in figure 8 (top left, dashed line). In this case, the induced current is slightly larger than when bulk transport data are employed. Clearly, the difference between the two cases arises from the drift-diffusion equation (13) and not Ramo’s theorem (23) where only flux drift velocity is used. This difference can be understood by considering a simple avalanche growth with multiplication factor $\exp((\nu_i - \nu_a)l/W)$ where l is the distance to the anode. Indeed, since in RPC gases the bulk drift velocity is higher than flux drift velocity (figure 2), the avalanche multiplication factor will be higher in the flux case. The difference is even more pronounced at lower electric field of 178 Td where saturated avalanche does not progress into positive streamer (figure 8, top right).

In addition to single Gaussian initial conditions, we have also calculated the induced current in the case of ATLAS RPC with $E_0/N = 196$ Td, where the initial distribution consists of multiple Gaussians representing primary ionization with 10 clusters mm^{-1} and 3 electrons/cluster. The distribution is given as $n_e(x, t = 0) = \sum_{i=0}^{20} G(i \cdot 0.1 \text{ mm}, \sigma_0)$ where $G(x_0, \sigma_0)$ is a Gaussian defined in (19) with $N_{e0} = 3$ electrons and $\sigma_0 = 0.1 \text{ mm}/6$. The results with this initial condition are shown in figure 9. Compared to the single Gaussian case, the induced current has a similar shape but with steeper rising edge and slightly rounded peak. These differences are mainly due to clusters near the cathode, which form a tail of the single Gaussian made by merging of small clusters during the avalanche and streamer formation phase.

Figure 8 shows the induced currents for ALICE timing RPC and timing RPC [32]. In contrast to ATLAS triggering RPC, the induced signals of timing RPCs at their operating fields are larger in amplitude, shorter in duration and rise faster as a consequence of higher electric fields and smaller gas gaps. For example, in case of ALICE timing RPC (figure 8, middle left),

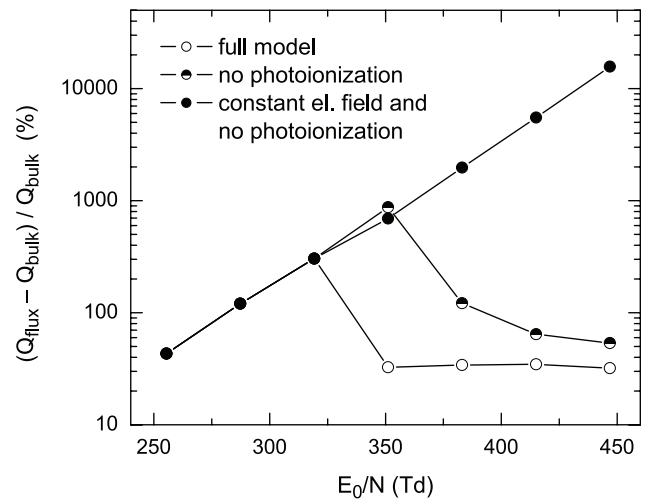


Figure 11. Percentage difference between the induced charges Q_{flux} and Q_{bulk} for the ALICE timing RPC. The difference is calculated over a range of applied electric fields for three modeling scenarios: (1) full model, (2) no photoionization, and (3) constant electric field and no photoionization.

the peak due to positive streamer is smaller and has a faster rising edge than in case of ATLAS RPC. It is also followed by a small peculiar peak after about 0.1 ns. We have not fully investigated the origin of this small peak but it shows no sign of numerical artifact. Also, due to greater difference between flux and bulk transport data (figures 2 and 4) the difference between corresponding signals is larger compared to ATLAS RPC, especially at lower electric field (figure 8, middle right).

The results for the three RPC configurations and gas mixtures presented in this section show an interesting behavior—the discrepancy between the induced currents, calculated with flux and bulk transport data, decreases with the applied electric field strength. One should expect the opposite, knowing that the difference between the flux and bulk transport data increases with the electric field in RPC operating range (figures 2 and 4). This phenomenon is discussed in the following section.

3.4. Induced charge

In this section, we investigate the impact of electron transport data on the fast component of the induced charge. The induced charge is calculated as an integral of the induced current i.e.

$Q = \int_0^{+\infty} i(t) dt$. Figure 10 shows the percentage difference between the induced charges Q_{flux} and Q_{bulk} , obtained using flux and bulk transport data, respectively. The difference is calculated over a range of operating electric fields for the three RPC configurations. The difference ranges from 6% for the ATLAS RPC up to 600% for the timing RPC [32]. This is understandable considering the corresponding transport data. However, for each of these RPC configurations, the difference grows with the electric field up to a certain point when it drops abruptly. We note that the induced currents on the left side of the figure 8 are calculated using the applied fields above this threshold, while figures on the right side are calculated using applied fields below the threshold. This behavior seems

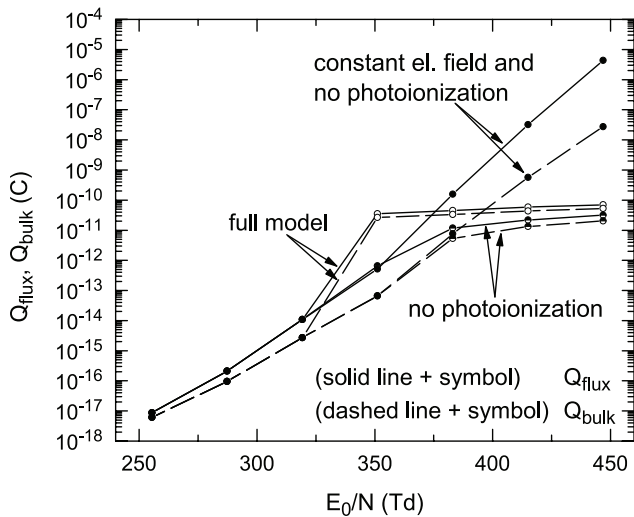


Figure 12. Induced charges Q_{flux} and Q_{bulk} calculated over a range of applied electric fields for the ALICE timing RPC using three modeling scenarios: (1) full model, (2) no photoionization and (3) constant electric field and no photoionization.

counter-intuitive considering that above ~ 100 Td the difference between flux and bulk transport data grows monotonically with the electric field. Moreover, the space charge effects can increase this difference even further through enhancement or reduction of the electric field toward the regions where flux and bulk transport data differ considerably (figures 2 and 4).

In order to investigate this effect, we modify our model from section 2.3 to include two more scenarios: (1) no photoionization ($S_{\text{ph}}(x, t) \equiv 0$), and (2) constant electric field i.e. no space charge effects, and no photoionization ($E(x, t) \equiv E_0$, $S_{\text{ph}}(x, t) \equiv 0$). These two scenarios in addition to the full model are used to calculate the percentage difference between the induced charges Q_{flux} and Q_{bulk} for the ALICE timing RPC (figure 11). It is evident that without space charge effects and photoionization the difference grows steadily with the electric field. Without photoionization, the space charge effects slightly enhance the difference at 351 Td. Above this electric field, the difference decreases continuously due to space charge effects alone. The photoionization only suppresses the difference more rapidly since it produces additional space charge.

Figure 12 shows the induced charges Q_{flux} and Q_{bulk} for the ALICE timing RPC calculated using the three modeling scenarios. The saturation effect induced by the space charge is clearly visible. Since $Q_{\text{flux}} > Q_{\text{bulk}}$, more space charge is produced in the flux case. Therefore, Q_{flux} saturates faster with the electric field than Q_{bulk} and the difference between them starts to drop. The inclusion of photoionization results in more space charge and consequently faster saturation. It is also seen that, in an isolated case of Q_{flux} at 351 Td, the space charge effects can slightly increase the induced charge. We should also note that the calculated induced charge seems unrealistically large compared to some experimental data for the fast component of the induced charge [32, 58]. This can be due to many reasons including the constraints of the 1.5D model itself, but also its parameters which are not determined accurately such as radius R_0 and photoionization parameters δ , λ

and Q . Still, the most obvious factor is the weighting field E_w/V_w which we assume as $1/d$. Depending on the electrode permittivity and thickness, the weighting field for some RPC geometries can be a few times smaller than $1/d$.

4. Conclusion

In this work we have discussed some aspects of electron transport in gases relevant for modeling of RPCs. Under hydrodynamic conditions, we have shown how the difference between flux and bulk transport data arises due to presence of non-conservative collisions. The duality of transport data was clearly visible in case of three RPC gas mixtures with different SF_6 content. One important implication is that in modeling of electron avalanches, bulk data should generally be used. A fluid model with photoionization was developed in order to demonstrate how the transport data used as input affect the results of RPC modeling. Using this model we have investigated the streamer development in ATLAS triggering RPC. It was found that the electron absorption on the anode has large influence on the space charge effects and positive streamer formation. The model was also used to calculate the induced signals for ATLAS triggering RPC, ALICE timing RPC and timing RPC [32]. The most striking observation is the difference between the induced charges calculated using flux and bulk data. This difference can reach up to 80% in case of ATLAS RPC or several hundred percent in case of timing RPCs at lower operating fields. However, at higher electric fields the saturation effect due to space charge and photoionization lowers the difference to about 6% for the ATLAS RPC and 30% for the timing RPCs. This illustrates the importance of correct implementation of data in modeling. One should be aware of the origin of the transport data and the type of transport data required in modeling.

The formalism and methodology presented in this paper are valid for other types of gaseous particle detectors. Many of the methods and techniques developed in the framework of swarm physics directly carry over to the particle detectors. We are currently working on extending the fluid treatment of RPCs to include more balance equations and utilizing momentum transfer theory [25] to evaluate the collisional terms. This will facilitate a full fluid treatment of RPCs using state-of-the-art theory.

Acknowledgments

This work was supported by MPNTRRS Projects OI171037 and III41011.

References

- [1] Santonico R and Cardarelli R 1981 *Nucl. Instrum. Methods* **187** 377–80
- [2] Cardarelli R, Santonico R, Di Biagio A and Lucci A 1988 *Nucl. Instrum. Methods A* **263** 20–5
- [3] The ATLAS Collaboration 2008 *J. Instrum.* **3** S08003
- [4] The ALICE Collaboration 2008 *J. Instrum.* **3** S08002
- [5] The CMS Collaboration 2008 *J. Instrum.* **3** S08004

- [6] Santonico R 2012 *Nucl. Instrum. Methods A* **661** S2–5
- [7] Fonte P 2002 *IEEE Trans. Nucl. Sci.* **49** 881–7
- [8] Iuppa R 2015 *J. Instrum.* **10** C04044
- [9] Cârloganu C et al 2013 *Geosci. Instrum. Methods Data Syst.* **2** 55–60
- [10] Couceiro M, Crespo P, Mendes L, Ferreira N, Ferreira Marques R and Fonte P 2012 *Nucl. Instrum. Methods A* **661** S156–8
- [11] Mangiarotti A, Fonte P and Gobbi A 2004 *Nucl. Instrum. Methods A* **533** 16–21
- [12] Riegler W 2009 *Nucl. Instrum. Methods A* **602** 377–90
- [13] Riegler W and Lippmann C 2004 *Nucl. Instrum. Methods A* **518** 86–90
- [14] Salim M, Hasan R, Majumdar N, Mukhopadhyay S and Satyanarayana B 2012 *J. Instrum.* **7** P11019
- [15] Bošnjaković D, Petrović Z Lj and Dujko S 2014 *J. Instrum.* **9** P09012
- [16] Khosravi Khorashad L, Moshaii A and Hosseini S 2011 *Europhys. Lett.* **96** 45002
- [17] Moshaii A, Khosravi Khorashad L, Eskandari M and Hosseini S 2012 *Nucl. Instrum. Methods A* **661** S168–71
- [18] Fonte P 2013 *J. Instrum.* **8** P11001
- [19] Petrović Z Lj, Dujko S, Marić D, Malović G, Nikitović Ž, Šašić O, Jovanović J, Stojanović V and Radmilović-Raenović M 2009 *J. Phys. D: Appl. Phys.* **42** 194002
- [20] Petrović Z Lj, Švakov M, Nikitović Ž, Dujko S, Šašić O, Jovanović J, Malović G and Stojanović V 2007 *Plasma Sources Sci. Technol.* **16** S1–12
- [21] Dujko S, White R D and Petrović Z Lj 2008 *J. Phys. D: Appl. Phys.* **41** 245205
- [22] Dujko S, White R D, Raspopović Z M and Petrović Z Lj 2012 *Nucl. Instrum. Methods B* **279** 84–91
- [23] White R D, Dujko S, Ness K F, Robson R E, Raspopović Z and Petrović Z Lj 2008 *J. Phys. D: Appl. Phys.* **41** 025206
- [24] Dujko S, White R D, Petrović Z Lj and Robson R E 2010 *Phys. Rev. E* **81** 046403
- [25] White R D, Robson R E, Dujko S, Nicoletopoulos P and Li B 2009 *J. Phys. D: Appl. Phys.* **42** 194001
- [26] Biagi S F 1999 *Nucl. Instrum. Methods A* **421** 234–40
- [27] Robson R E 1991 *Aust. J. Phys.* **44** 685
- [28] Sakai Y, Tagashira H and Sakamoto S 1977 *J. Phys. D: Appl. Phys.* **10** 1035–49
- [29] BOLSIG + www.bolsig.laplace.univ-tlse.fr version: 07/2015
- [30] Dujko S, Raspopović Z M, Petrović Z Lj and Makabe T 2003 *IEEE Trans. Plasma Sci.* **31** 711–6
- [31] Bošnjaković D, Petrović Z Lj, White R D and Dujko S 2014 *J. Phys. D: Appl. Phys.* **47** 435203
- [32] Lopes L, Fonte P and Mangiarotti A 2012 *Nucl. Instrum. Methods A* **661** S194–7
- [33] Kumar K, Skullerud H R and Robson R E 1980 *Aust. J. Phys.* **33** 343
- [34] Dujko S, White R D, Ness K F, Petrović Z Lj and Robson R E 2006 *J. Phys. D: Appl. Phys.* **39** 4788–98
- [35] Ness K F and Robson R E 1986 *Phys. Rev. A* **34** 2185–209
- [36] Nolan A M, Brennan M J, Ness K F and Wedding A B 1997 *J. Phys. D: Appl. Phys.* **30** 2865–71
- [37] Legler W 1961 *Z. Naturforsch.* **16a** 253
- [38] Riegler W, Lippmann C and Veenhof R 2003 *Nucl. Instrum. Methods A* **500** 144–62
- [39] Basile G, Gallimberti I, Stangherlin S and Teich T H 1991 Swarm parameters for tetrafluoroethane (HFA 134a) *Proc. XX Int. Conf. on Phenomena in Ionized Gases* vol 2, ed M Vaselli p 361
- [40] de Urquijo J, Juárez A M, Basurto E and Hernández-Ávila J L 2009 *Eur. Phys. J. D* **51** 241–6
- [41] Dujko S, Markosyan A H, White R D and Ebert U 2013 *J. Phys. D: Appl. Phys.* **46** 475202
- [42] Markosyan A H, Teunissen J, Dujko S and Ebert U 2015 *Plasma Sources Sci. Technol.* **24** 065002
- [43] Dujko S, Raspopović Z M and Petrović Z Lj 2005 *J. Phys. D: Appl. Phys.* **38** 2952–66
- [44] Šašić O et al 2016 *Eur. Phys. J. D* to be submitted
- [45] Šašić O, Dupljanin S, de Urquijo J and Petrović Z Lj 2013 *J. Phys. D: Appl. Phys.* **46** 325201
- [46] Lima I B, Mangiarotti A, Vivaldini T C, Gonçalves J A C, Botelho S, Fonte P, Takahashi J, Tarelho L V and Bueno C C 2012 *Nucl. Instrum. Methods A* **670** 55–60
- [47] Itoh H, Matsumura T, Satoh K, Date H, Nakao Y and Tagashira H 1993 *J. Phys. D: Appl. Phys.* **26** 1975–9
- [48] Petrović Z Lj, Crompton R W and Haddad G N 1984 *Aust. J. Phys.* **37** 23
- [49] Robson R E 1984 *Aust. J. Phys.* **37** 35
- [50] Davies A J, Evans C J and Jones F L 1964 *Proc. R. Soc. A* **281** 164–83
- [51] Fonte P 1996 *IEEE Trans. Nucl. Sci.* **43** 2135–40
- [52] Kline L E 1974 *J. Appl. Phys.* **45** 2046
- [53] Hundsdorfer W and Verwer J 2003 *Numerical Solution of Time-Dependent Advection-Diffusion-Reaction Equations (Springer Series in Computational Mathematics vol 33)* (Berlin: Springer)
- [54] Courant R, Friedrichs K and Lewy H 1928 *Math. Ann.* **100** 32–74
- [55] Ramo S 1939 *Proc. IRE* **27** 584
- [56] Anderson D F, Kwan S and Peskov V 1994 *Nucl. Instrum. Methods A* **348** 324–8
- [57] Cardarelli R, Makeev V and Santonico R 1996 *Nucl. Instrum. Methods A* **382** 470–4
- [58] Fonte P, Smirnitski A and Williams M C S 2000 *Nucl. Instrum. Methods A* **443** 201–4

Electron swarm properties under the influence of a very strong attachment in SF₆ and CF₃I obtained by Monte Carlo rescaling procedures

J Mirić¹, D Bošnjaković¹, I Simonović¹, Z Lj Petrović^{1,2} and S Dujko¹

¹ Institute of Physics, University of Belgrade, PO Box 68, 11080 Belgrade, Serbia

² Serbian Academy of Sciences and Arts, Knez Mihailova 35, 11001 Belgrade, Serbia

E-mail: sasa.dujko@ipb.ac.rs

Received 13 May 2016, revised 28 July 2016

Accepted for publication 19 September 2016

Published 14 October 2016



Abstract

Electron attachment often imposes practical difficulties in Monte Carlo simulations, particularly under conditions of extensive losses of seed electrons. In this paper, we discuss two rescaling procedures for Monte Carlo simulations of electron transport in strongly attaching gases: (1) discrete rescaling, and (2) continuous rescaling. The two procedures are implemented in our Monte Carlo code with an aim of analyzing electron transport processes and attachment induced phenomena in sulfur-hexafluoride (SF₆) and trifluoroiodomethane (CF₃I). Though calculations have been performed over the entire range of reduced electric fields E/n_0 (where n_0 is the gas number density) where experimental data are available, the emphasis is placed on the analysis below critical (electric gas breakdown) fields and under conditions when transport properties are greatly affected by electron attachment. The present calculations of electron transport data for SF₆ and CF₃I at low E/n_0 take into account the full extent of the influence of electron attachment and spatially selective electron losses along the profile of electron swarm and attempts to produce data that may be used to model this range of conditions. The results of Monte Carlo simulations are compared to those predicted by the publicly available two term Boltzmann solver BOLSIG+. A multitude of kinetic phenomena in electron transport has been observed and discussed using physical arguments. In particular, we discuss two important phenomena: (1) the reduction of the mean energy with increasing E/n_0 for electrons in SF₆ and (2) the occurrence of negative differential conductivity (NDC) in the bulk drift velocity only for electrons in both SF₆ and CF₃I. The electron energy distribution function, spatial variations of the rate coefficient for electron attachment and average energy as well as spatial profile of the swarm are calculated and used to understand these phenomena.

Keywords: Monte Carlo, electron transport, electron attachment, SF₆, CF₃I

(Some figures may appear in colour only in the online journal)

1. Introduction

Electron transport in strongly attaching gases has long been of interest, with applications in many areas of fundamental physics and technology. Electron attaching gases support key processes for plasma etching and cleaning in semiconductor

fabrication [1, 2], high-voltage gas insulation [3] and particle detectors in high energy physics [4–6]. The importance of studies of electron attachment has also been recognized in other fields, including planetary atmospheres, excimer lasers, plasma medicine and lighting applications, as well as in life science for understanding radiation damage in biological matter.

The fundamental importance of electron attachment processes has led to many experimental and theoretical swarm studies. For some gases the cross sections for attachment may be very large resulting in a rapid disappearance of free electrons that greatly complicates the measurements of transport coefficients [1, 7–9]. The pioneering studies date back to the 1970s, and the well-known swarm method of deriving cross section for electron attachment developed by Christophorou and his co-workers [10]. According to this method, trace amounts of an electron attaching gas are mixed into the buffer gases, typically nitrogen to scan the lower mean energies and argon to scan the higher mean energies. This technique results in the removal of electrons without disturbing the electron energy distribution function. In such mixtures the losses depend only on the very small amount of the added gas and we may measure the density reduced electron attachment rate coefficient. Electron attachment cross sections can be determined by deconvoluting the mixture data, since the electron energy distribution function is a known function of E/n_0 as calculated for the pure buffer gas. Examples of this procedure are cross sections for electron attachment in SF₆ and SF₆-related molecules [11–15] as well as cross sections and rate coefficients for a range of fluorocarbons [1, 12, 16–18] and other relevant gases for applications [1, 19–22]. In addition to non-equilibrium data, there is a separate category of experiments, including flowing afterglow, the Cavalleri diffusion experiment [9, 23, 24], and others that provide attachment rates for thermal equilibrium (i.e. without an applied electric field). These may be taken at different temperatures, but the range of energies covered by this technique is very narrow. These two techniques have been used to evaluate the cross sections for SF₆ and CF₃I, always under the assumption that the effect of attachment is merely on the number of particles and not on any other swarm properties.

A thorough understanding of the influence of attachment on the drift and diffusion of the electrons provides information which could be used in analysis of kinetic phenomena in complex electronegative gases and related plasmas. The attachment cooling and heating [25, 26], negative absolute electron flux mobility [27, 60] and anomalous phase shifts of drift velocity in AC electric fields [28] are some examples of these phenomena in strongly attaching gases, which may not be trivially predicted on the basis of individual collision events and external fields. Negative differential conductivity (NDC) induced by 3-body attachment for lower E/n_0 and higher pressures in molecular oxygen and its mixture with other gases is another example of phenomena induced by strong electron attachment [29]. The duality in transport coefficients, e.g. the existence of two fundamentally different families of transport coefficients, the bulk and flux, is caused by the explicit effects of electron impact ionization and electron attachment [7, 30–32]. The differences between two sets of data vary from a few percents to a few orders of magnitude and hence a special care is needed in the implementation of data in fluid models of plasma discharges [7, 31, 33–35]. On one hand, most plasma modeling is based on flux quantities while experiments aimed at yielding cross section data provide mostly but not uniquely the bulk transport data. This differentiation between flux and

bulk transport properties is not merely a whimsey of theorists, but it is essential in obtaining and applying the basic swarm data. In addition, the production of negative ions has a large effect on the transport and spatial distribution of other charged particle species as well as on the structure of the sheath and occurrence of relaxation oscillations in charged particle densities [36–41].

There are three main approaches to the theoretical description of electron transport in gases: the kinetic Boltzmann equation, the stochastic particle simulation by the Monte Carlo method and semi-quantitative momentum transfer theory. Restrictions on the accuracy of momentum transfer theory for studies of electron transport in attaching gases, particularly under non-hydrodynamic conditions, have already been discussed and illustrated [31, 42, 43]. Boltzmann equation analyses for SF₆ and its mixtures with other gases (see for example [11, 44–50]) have been performed several times in the past. Two important studies devoted to the calculation of electron swarm parameters based on a Boltzmann equation have also been performed for CF₃I [51, 52]. Theories for solving the Boltzmann equation were usually restricted to low-order truncations in the Legendre expansions of the velocity dependence assuming quasi-isotropy in velocity space. The explicit effects of electron attachment were also neglected and electron transport was studied usually in terms of the flux data only. These theories had also restricted domains of validity on the applied E/n_0 in spite of their coverage of a considerably broader range. One thing that strikes the reader surveying the literature on electron transport in SF₆ is the systematic lack of reliable data for electron transport coefficients for E/n_0 less than 50 Td. Contemporary moment methods for solving Boltzmann's equation [31, 53] are also faced with a lot of systematic difficulties, particularly under conditions of the predominant removal of the lower energy electrons which results in an increase in the mean energy, i.e. attachment heating. Under these conditions the bulk of the distribution function is shifted towards a higher energy which in turn results in the high energy tail falling off much slower than a Maxwellian. This is exactly what may happen in the analysis of electron transport in strongly attaching gases such as SF₆ or CF₃I for lower E/n_0 . The moment method for solving Boltzmann's equation under these circumstances usually requires the prohibitive number of basis functions for resolving the speed/energy dependency of the distribution function and/or unrealistically large computation time. As a consequence, the standard numerical schemes employed within the framework of moment methods usually fail.

The present investigation is thus mainly concerned with the Monte Carlo simulations of electron transport in strongly attaching gases. Monte Carlo simulations have also been employed for the analysis of electron transport in the mixtures of SF₆ [46, 54–57] and CF₃I [58] with other gases usually with an aim of evaluating the insulation strength and critical electric fields. However, electron attachment in strongly electronegative gases often imposes practical difficulties in Monte Carlo simulations. This is especially noticeable at lower E/n_0 , where electron attachment is one of the dominant processes which may lead to the extensive vanishing of the seed electrons and

consequently to the decrease of the statistical accuracy of the output results. In extreme cases, the entire electron swarm might be consumed by attachment way before the equilibrated (steady-state regime) is achieved. An obvious solution would be to use a very large number of initial electrons, but this often leads to a dramatic increase of computation time and/or required memory/computing resources which are beyond practical limits. Given the computation restrictions of the time, the workers were forced to develop methods to combat the computational difficulties induced by the extensive vanishing of the seed electrons. Two general methods were developed: (1) addition of new electrons by uniform scaling of the electron swarm at certain time instants under hydrodynamic conditions [26, 59] or at certain positions under steady-state Townsend conditions [60], when number of electrons reaches a pre-defined threshold, and (2) implementation of an additional fictitious ionization channel/process with a constant collision frequency (providing that the corresponding ionization rate is chosen to be approximately equal to the attachment rate) [54]. On the other hand, similar rescaling may be applied for the increasing number of electrons as has been tested at the larger E/n_0 by Li *et al* [61]. Further distinction and specification between methods developed by Nolan *et al* [26] and Dyatko *et al* [60] on one hand and Raspopović *et al* [59] on the other, will be discussed in later sections. These methods have not been compared to each other in a comprehensive and rigorous manner. This raises a number of questions. How accurate, these methods are? Which is the more efficient? Which is easier for implementation? What is their relationship to each other? Which one is more flexible? In this paper, we will try to address some of these issues. In particular, the present paper serves to summarize the salient features of these methods in a way which we hope will be of benefit to all present and future developers of Monte Carlo codes. Finally, it is also important to note that in the present paper we extend the method initially developed by Yousfi *et al* [54], by introducing time-dependent collision frequency for the fictitious ionization process.

This paper is organized as follows: in section 2, we briefly review the basic elements of our Monte Carlo code, before detailing the rescaling procedures employed to combat the computational difficulties initiated by the rapid disappearance of electrons. In the same section, we illustrate the issue of electron losses by considering the evolution of the number of electrons for a range of E/n_0 in SF₆ and CF₃I. In section 3, we evaluate the performance of rescaling procedures by simulating electron transport in SF₆ and CF₃I over a wide range of E/n_0 . We will also highlight the substantial difference between the bulk and flux transport coefficients in SF₆ and CF₃I. Special attention will be paid to the occurrence of negative differential conductivity (NDC) in the profile of the bulk drift velocity. For electrons in SF₆ another phenomenon arises: for certain reduced electric fields we find regions where the swarm mean energy decreases with increasing E/n_0 . In the last segment of the section 3, we discuss two important issues: (1) how to use the rescaling procedures in Monte Carlo codes, and (2) rescaling procedures as a tool in the modeling of non-hydrodynamic effects in swarm experiments. In section 4, we present our conclusions and recommendations.

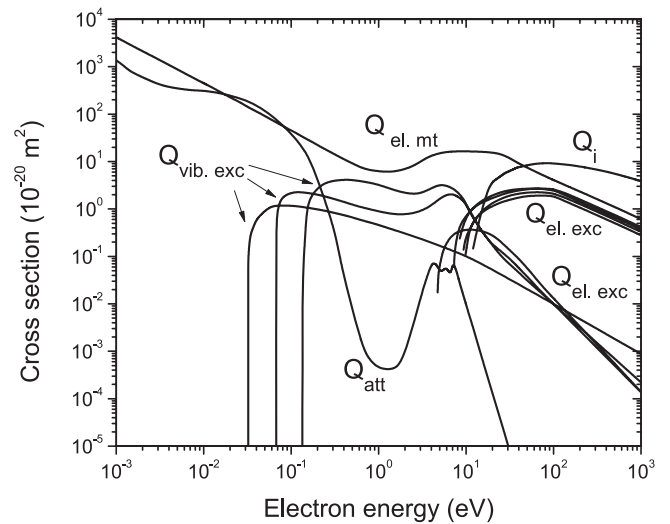


Figure 1. Electron impact cross-sections for CF₃I used in this study [62]: $Q_{el, mt}$ momentum transfer in elastic collisions, $Q_{vib, exc}$ vibrational excitation, $Q_{el, exc}$ electronic excitation, Q_{att} dissociative attachment and Q_i electron-impact ionization.

2. Input data and computational methods

2.1. Cross sections for electron scattering and simulation conditions

We begin this section with a brief description of cross sections for electron scattering in SF₆ and CF₃I. For the SF₆ cross sections we use the set developed by Itoh *et al* [47]. This set was initially based on published measurements of cross sections for individual collision processes. Using the standard swarm procedure, the initial set was modified to improve agreement between the calculated swarm parameters and the experimental values. The set includes one vibrational channel, one electronic excitation channel, as well as elastic, ionization and five different attachment channels.

This study considers electron transport in CF₃I using the cross section set developed in our laboratory [62]. This set of cross sections is shown in figure 1. It should be noted that this set is similar but not identical to that developed by Kimura and Nakamura [63]. We have used the measured data under pulsed Townsend conditions for pure CF₃I and its mixtures with Ar and CO₂ in a standard swarm procedure with the aim of improving the accuracy and completeness of a set of cross sections. It consists of the elastic momentum transfer cross section, three cross sections for vibrational and five cross sections for electronic excitations as well as one cross section for electron-impact ionization with a threshold of 10.4 eV and one cross section for dissociative attachment. For more details the reader is referred to our future paper [64].

For both SF₆ and CF₃I all electron scattering are assumed isotropic and hence the elastic cross section is the same as the elastic momentum transfer cross section. Simulations have been performed for E/n_0 ranging from 1 to 1000 Td. The pressure and temperature of the background gas are 1 Torr and 300 K, respectively. It should be mentioned that special care in our Monte Carlo code has been paid to proper treatment of the thermal motion of the host gas molecules and their influence

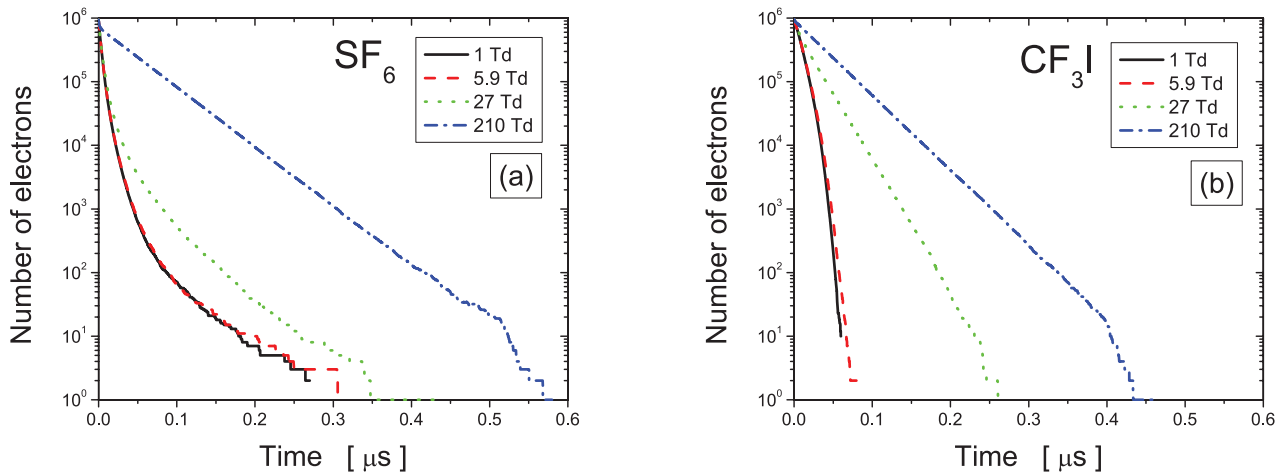


Figure 2. Electron number density decay for four different reduced electric fields as indicated on the graph. Calculations are performed for SF₆ (a) and CF₃I (b).

on electrons, which is very important at low electric fields, when the mean electron energy is comparable to the thermal energy of the host gas [65]. After ionization, the available energy is partitioned between two electrons in such a way that all fractions of the distribution are equally probable.

2.2. Monte Carlo method

The Monte Carlo simulation technique used in the present work is described at length in our previous publications [32, 53, 59, 66, 67]. In brief, we follow the spatiotemporal evolution of each electron through time steps which are fractions of the mean collision time. In association with random numbers, these finite time steps are used to solve the integral equation for the collision probability in order to determine the time of the next collision. The number of time steps is determined in such a way as to optimize the performance of the Monte Carlo code without reducing the accuracy of the final results. When the moment of the next collision is established, the additional sequences of random numbers are used, first to determine the nature of a collision, taking into account the relative probabilities of the various collision types, and second to determine the change in the direction of the electron velocity. All dynamic properties of each electron such as position, velocity, and energy are updated between and after the collisions. Sampling of electron dynamic properties is not correlated to the time of the next collision and is performed in a way that ensemble averages can be taken in both the velocity and configuration space. Explicit formulas for the bulk and flux transport properties have been given in our previous publications [59, 66]. To evaluate the accuracy of the Monte Carlo code, Boltzmann analyses were performed in parallel with the Monte Carlo calculations using the multi term method described in detail by Dujko *et al* [53]. In addition, we use the BOLSIG+, a publicly available Boltzmann solver based on a two term theory [68]. The most recent version of this code might be used to study the electron transport in terms of both the flux and bulk data which is very useful for some aspects of plasma modeling [7]. At the same time, the comparison between our results and those computed by BOLSIG+ which is presented in this paper, should

be viewed as the first benchmark for the bulk BOLSIG+ data. Our Monte Carlo code and multi term codes for solving the Boltzmann equation have been subject of a detailed testing for a wide range of model and real gases [31, 53, 59, 67].

In figure 2 we illustrate the losses of electrons during the evolution of the swarm towards the steady-state. The initial number of electrons is set to 1×10^6 and calculations are performed for a range of reduced electric fields E/n_0 as indicated on the graphs. For both SF₆ and CF₃I, we observe that at small E/n_0 , i.e. at low mean energies, the number of electrons decreases much faster. This is a clear sign that collision frequency for electron attachment increases with decreasing E/n_0 . Electrons in CF₃I are lost continuously and consequently the number of electrons in the swarm decreases exponentially with time. The same trend may be observed for electrons in SF₆ at 210 Td. For the remaining E/n_0 the number of electrons is reduced with time even faster. Comparing SF₆ and CF₃I, it is evident that the electrons are more efficiently consumed by electron attachment in SF₆ in the early stage of the simulation. Conversely, in the last stage of simulation the electrons are more consumed by electron attachment in CF₃I than in SF₆. In any case, the electron swarms in both cases are entirely consumed by attachment way before the steady-state regime and hence the simulations are stopped. In other words, the number density drops down by six orders of magnitude over the course of several hundred nanoseconds in both gases. To facilitate the numerical simulation, it is clear that some kind of rescaling of the number density is necessary to compensate for the electrons consumed by electron attachment. This procedure should not in any way disrupt the spatial gradients in the distribution function. On the other hand, releasing electrons with some fixed arbitrary initial condition would require that they equilibrate with the electric field during which time again majority of such additional electrons would be lost.

2.3. Rescaling procedures

To counteract the effect of attachment in an optimal fashion while keeping the statistical accuracy, the following rescaling procedures were proposed and applied so far:

- (1) Uniform generation of new electrons with initial properties taken from the remaining electrons thus taking advantage of the equilibration that has been achieved so far [59]. To make this procedure effective i.e. to avoid losing population in some smaller pockets of the ensemble the population should be allowed to oscillate between N_1 and N_0 , where $N_1 > N_0$ but their difference is relatively small. Here N_0 is minimum allowed number of electrons while N_1 is maximum number of electrons in the simulation after rescaling.
- (2) Uniform scaling of an electron swarm by a factor of 2 or 3 at certain instants of time [26] or distance [60] depending on the simulation conditions where the probability of scaling for each electron is set to unity.
- (3) Introduction of an additional fictitious ionization process with a constant ionization frequency (that is close to the rate for attachment), which artificially increases the number of simulated electrons [54, 61]. Uniform rescaling of the swarm is done by randomly choosing the electrons which are to be ‘duplicated’. The newborn electron has the same initial dynamic properties, coordinates, velocity, and energy as the original. Following the creation of a new electron their further histories diverge according to the independently selected random numbers.

Comparing the procedures (1) and (2), it is clear that there are no essential differences between them. The only difference lies in the fact that in the procedure (2) duplicating is performed for all the electrons in the simulation while according the procedure (1), the probability of duplication is determined by the current ratio of the number of electrons to the desired number of electrons in the simulation, which is specified in advance. On the other hand, fictitious ionization collision generates a new electron which is given the same position, velocity and energy as the primary electron that is not necessarily the electron lost in attachment. In this paper, we shall refer to the procedure (1) as *discrete rescaling*, since the procedure is applied at discrete time instants. The procedure (2) shall be termed as *swarm duplication* and finally we shall refer to the procedure (3) as the *continuous rescaling* since the rescaling is done during the entire simulation. An important requirement is that the rescaling must not perturb/change/disturb the normalized electron distribution function and its evolution. Li *et al* [61] showed that the continuous rescaling procedure meets this requirement. In case of discrete rescaling as applied to the symmetrical yet different problem of excessive ionization, it was argued that one cannot be absolutely confident that the rescaled distribution is a good representation of the original [69], except when steady state is achieved [70].

In what follows, we discuss the continuous rescaling. Following the previous works [54, 61], the Boltzmann equation for the distribution function $f(\mathbf{r}, \mathbf{c}, t)$ without rescaling and $f^*(\mathbf{r}, \mathbf{c}, t)$ with rescaling are given by:

$$(\partial_t + \mathbf{c} \cdot \nabla_{\mathbf{r}} + \mathbf{a} \cdot \nabla_{\mathbf{c}})f(\mathbf{r}, \mathbf{c}, t) = -J(f), \quad (1)$$

and

$$(\partial_t + \mathbf{c} \cdot \nabla_{\mathbf{r}} + \mathbf{a} \cdot \nabla_{\mathbf{c}})f^*(\mathbf{r}, \mathbf{c}, t) = -J(f^*) + \nu_{\text{fi}}(t)f^*, \quad (2)$$

where \mathbf{a} is the acceleration due to the external fields, $J(f)$ is the collision operator for electron-neutral collisions and ν_{fi} is time-dependent fictitious ionization rate. If the collision operator is linear (i.e. if electron–electron collisions are negligible) and if the initial distributions (at time $t = 0$) are the same, it can be easily shown that the following relationship holds

$$f^*(\mathbf{r}, \mathbf{c}, t) = f(\mathbf{r}, \mathbf{c}, t) \exp\left(\int_0^t \nu_{\text{fi}}(\tau) d\tau\right). \quad (3)$$

Substituting equation (3) into equation (2) and using the linearity of the collision operator yields the following equation

$$J(f^*) = \exp\left(\int_0^t \nu_{\text{fi}}(\tau) d\tau\right) J(f). \quad (4)$$

Note that in contrast to Li *et al* [61] the collision frequency for the fictitious ionization is now a time-dependent function. In terms of numerical implementation, the only difference between our continuous rescaling procedure and the one described in [54, 61] is that we do not need to provide the fictitious ionization rate which is estimated by trial and error, in advance (*a priori*). Instead, our fictitious ionization rate is initially chosen to be equal to the calculated attachment rate at the beginning of the simulation. Afterwards, it is recalculated at fixed time instants in order to match the newly developed attachment rates. As a result, the number of electrons during the simulation usually does not differ from the initial one by more than 10%. It should be noted that the fictitious ionization process must not in any way be linked to the process of real ionization. It was introduced only as a way to scale the distribution function, or in other words, as a way of duplicating the electrons.

3. Results and discussion

In this section the rescaling procedures and associated Monte Carlo code outlined in the previous section are applied to investigate transport properties and attachment induced phenomena for electrons in SF₆ and CF₃I. Electron transport in these two strongly attaching gases provides a good test of different rescaling procedures, particularly for lower E/n_0 where electron attachment is the dominant non-conservative process. In addition to comparisons between different rescaling procedures, the emphasis of this section is the observation and physical interpretation of the attachment induced phenomena in the E/n_0 -profiles of mean energy, drift velocity and diffusion coefficients. In particular, we investigate the differences between the bulk and flux transport coefficients. We do not compare our results with experimentally measured data as it would distract the reader’s attention to the problems associated with the quality of the sets of the cross sections for electron scattering. There are no new experimental measurements of transport coefficients for electrons in SF₆, particularly for E/n_0 less than 50 Td and thus we have deliberately chosen not to display the comparison. On the other hand, one cannot expect the multi term results to be useful here as the conditions with excessive attachment would make convergence difficult in the low E/n_0 region, where comparison would be of

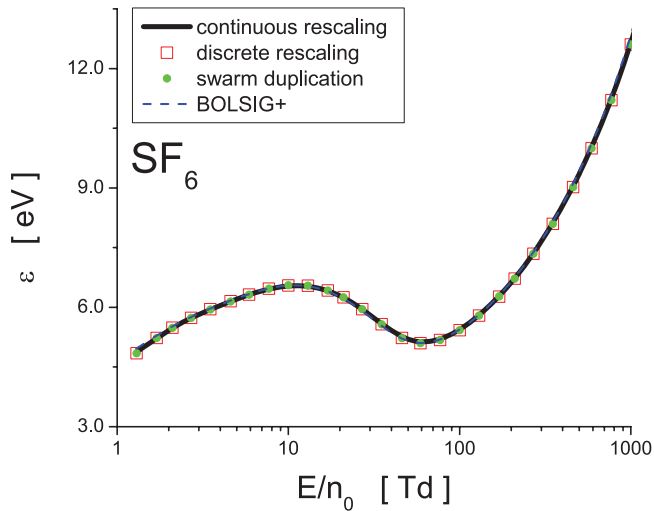


Figure 3. Variation of the mean energy with E/n_0 for electrons in SF_6 . Monte Carlo results using three different techniques for electron number density compensation (rescaling) are compared with the BOLSIG+ results.

interest. Thus, for clarity the multi term results are omitted. Both experimental and theoretical work on electron swarms in SF_6 prior to 1990 is summarized in the papers of Phelps and van Brunt [11], Gallagher *et al* [71] and Morrow [72]. Recent results can be found in the book by Raju [22] and the review article of Christophorou and Olthoff [12]. The swarm analysis and further improvements of the cross sections for electron scattering in CF_3I is a subject of our future work [64].

3.1. Transport properties for electrons in SF_6 and CF_3I

3.1.1. Mean energy. In figure 3 we show the variation of the mean energy with E/n_0 for electrons in SF_6 . The agreement between different rescaling procedures is excellent. This suggests that all rescaling procedures are equally valid for calculation of the mean energy (provided that rescaling is performed carefully). In addition, the BOLSIG+ results agree very well with those calculated by a Monte Carlo simulation technique. For lower E/n_0 , the mean energy initially increases with E/n_0 , reaching a peak at about 10 Td, and then surprisingly it starts to decrease with E/n_0 . The minimum of mean energy occurs at approximately 60 Td. For higher E/n_0 the mean energy monotonically increases with E/n_0 . The reduction in the mean energy with increasing E/n_0 has been reported for electrons in Ar [73] and O_2 [74] but in the presence of very strong magnetic fields. In the present work, however, the mean energy is reduced in absence of magnetic field which certainly represents one of the most striking and anomalous effects observed in this study. Moreover, this behavior is contrary to previous experiences in swarm physics as one would expect the mean swarm energy to increase with increasing E/n_0 . This is discussed in detail below.

In order to understand the anomalous behavior of the mean energy of electrons in SF_6 , in figure 4 we display the electron energy distribution functions for E/n_0 at 10, 27, 59 and 210 Td. Cross sections for some of the more relevant collision processes are also included, as indicated in the graph.

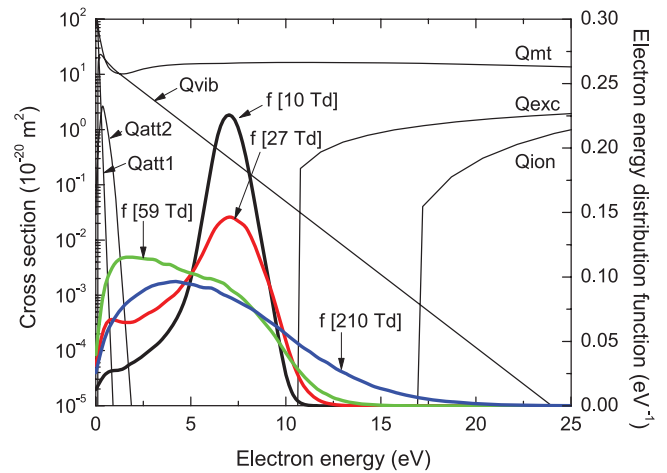


Figure 4. Electron energy distribution functions for E/n_0 of 10, 27, 59 and 210 Td. Cross sections for elastic momentum transfer (Qmt), electronic excitation (Qexc) and ionization (Qion) as well as for attachments that lead to the formation of SF_6^- (Qatt1) and SF_5^- (Qatt2) ions, are also included.

For clarity, the attachment cross sections for the formation of SF_4^- , F_2^- and F^- are omitted in the figure. For E/n_0 of 10 and 27 Td we observe the clear signs of ‘hole burning’ in the electron energy distribution function (EEDF). This phenomenon has been extensively discussed for electrons in O_2 [75, 76], O_2 mixtures [29, 77] and under conditions leading to the phenomenon of absolute negative electron mobility [27, 60] as well as for electrons in the gas mixtures of $\text{C}_2\text{H}_2\text{F}_4$, iso- C_4H_{10} and SF_6 used in resistive plate chambers in various high energy physics experiments at CERN [6]. For electrons in SF_6 , the collision frequency for electron attachment decreases with energy and hence the slower electrons at the trailing edge of the swarm are preferentially attached. As a consequence, the electrons are ‘bunched’ in the high-energy part of the distribution function which in turn moves the bulk of the distribution function to higher energies. This is the well-known phenomenon of attachment heating which has already been discussed in the literature for model [25, 26] and real gases [6, 29]. In the limit of the lowest E/n_0 we see that due to attachment heating the mean energy attains the unusually high value of almost 5 eV. For a majority of molecular gases, however, the mean energy is significantly reduced for lower E/n_0 due to presence of rotational, vibrational and electronic excitations which have threshold energies over a wide range. As E/n_0 further increases the mean energy is also increased as electrons are accelerated through a larger potential. However, in case of SF_6 , for E/n_0 increasing beyond 10 Td the mean energy is reduced. This atypical situation follows from the combined effects of attachment heating and inelastic cooling. From figure 4 we see that for E/n_0 of 27 and 59 Td the electrons from the tail of the corresponding distribution functions have enough energy to undergo the electronic excitation. Whenever an electron undergoes electronic excitations (or ionization) it loses the threshold energy of 9.8 eV (or 15.8 eV in case of ionization) and emerges from the collision with a reduced energy. This in turn diminishes the phenomenon of ‘hole burning’ in the distribution function by repopulating

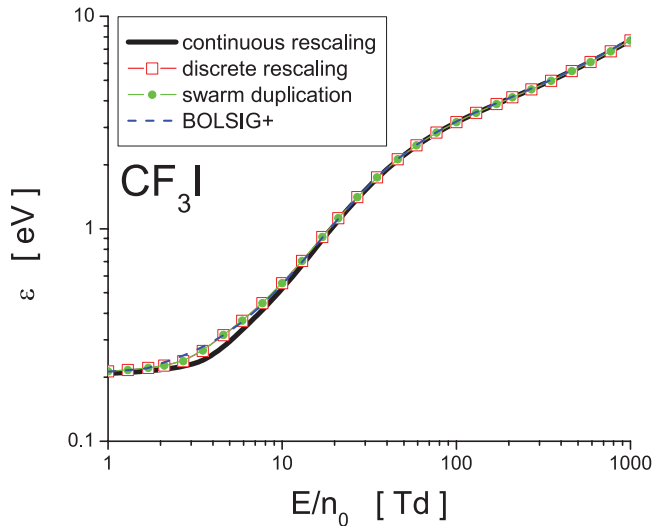


Figure 5. Variation of the mean energy with E/n_0 for electrons in CF_3I . Monte Carlo results using three different techniques for electron compensation are compared with the BOLSIG+ results.

the distribution function at the lower energy. The combined effects of attachment heating and inelastic cooling and subsequent redistribution of low-energy electrons are more significant for the energy balance than the energy gain from electric field and losses in other collisions. The vibrational excitation with the threshold of 0.098 eV is of less importance having in mind the actual values of the mean energy. For E/n_0 higher than 60 Td, the dominant part in the energy balance is the energy gain from the electric field while attachment heating and induced phenomena are significantly suppressed. Thus, for E/n_0 higher than 60 Td the mean energy monotonically increases with increasing E/n_0 .

The variation of the mean energy with E/n_0 for electrons in CF_3I is shown in figure 5. The agreement between different rescaling procedures is very good. Small deviations between discrete rescaling and swarm duplication from one side and continuous rescaling from the other side are present between approximately 3 and 20 Td. BOLSIG+ slightly overestimates the mean energy only in the limit of the lowest E/n_0 . In contrast to mean energy of the electrons in SF_6 , the mean energy of the electrons in CF_3I monotonically increases with E/n_0 without signs of anomalous behavior. If we take a careful look, then we can isolate three distinct regions of electron transport in CF_3I as E/n_0 increases. First, there is an initial region where the mean energy raises relatively slowly due to large energy loss of the electrons in low-threshold vibrational excitations. In this region the mean energy of the electrons is well above the thermal energy due to extensive attachment heating. The mean energy is raised much sharper between approximately 5 and 50 Td, indicating that electrons become able to overcome low-threshold vibrational excitations. The following region of slower rise follows from the explicit cooling of other inelastic processes, including electronic excitations and ionization, as these processes are now turned on. In conclusion, the nature of cross sections for electron scattering in CF_3I and their energy dependence as well as their mutual relations do not favor the development of the anomalous behavior of the swarm mean energy.

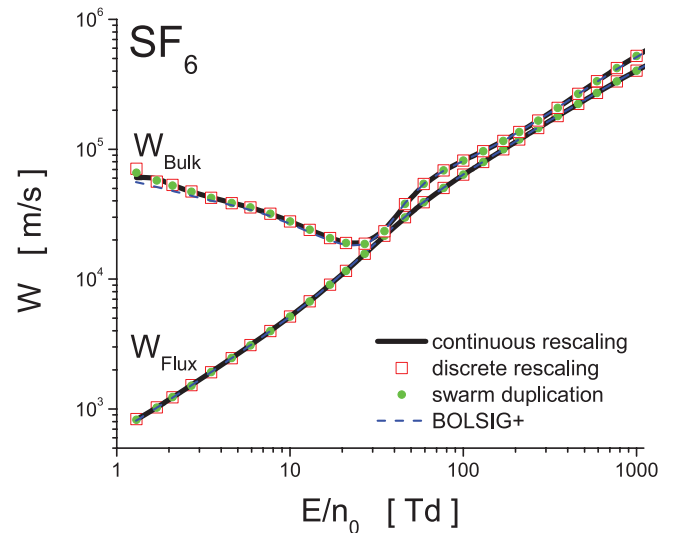


Figure 6. Variation of the drift velocity with E/n_0 for electrons in SF_6 . Monte Carlo results using three different techniques for electron number density compensation are compared with the BOLSIG+ results.

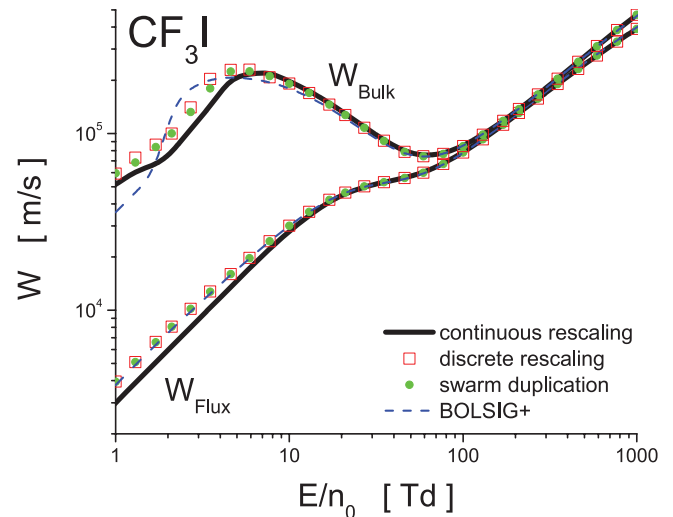


Figure 7. Variation of the drift velocity with E/n_0 for electrons in CF_3I . Monte Carlo results using three different techniques for electron number density compensation are compared with the BOLSIG+ results.

3.1.2. Drift velocity. In figures 6 and 7 we show variation of the bulk and flux drift velocity with E/n_0 for electrons in SF_6 and CF_3I , respectively. For electrons in SF_6 the agreement between different rescaling procedures for electron compensation is excellent for both the bulk and flux drift velocity over the entire E/n_0 range considered in this work. The BOLSIG+ bulk results slightly underestimate the corresponding bulk Monte Carlo results in the limit of the lowest E/n_0 . For electrons in CF_3I , the agreement among different rescaling procedures for electron compensation is also good except for lower E/n_0 where the continuous rescaling gives somewhat lower results than other techniques.

For both SF_6 and CF_3I , we see that the bulk dominates the flux drift velocity over the entire E/n_0 range considered in this work. For lower E/n_0 this is a consequence of a very intense

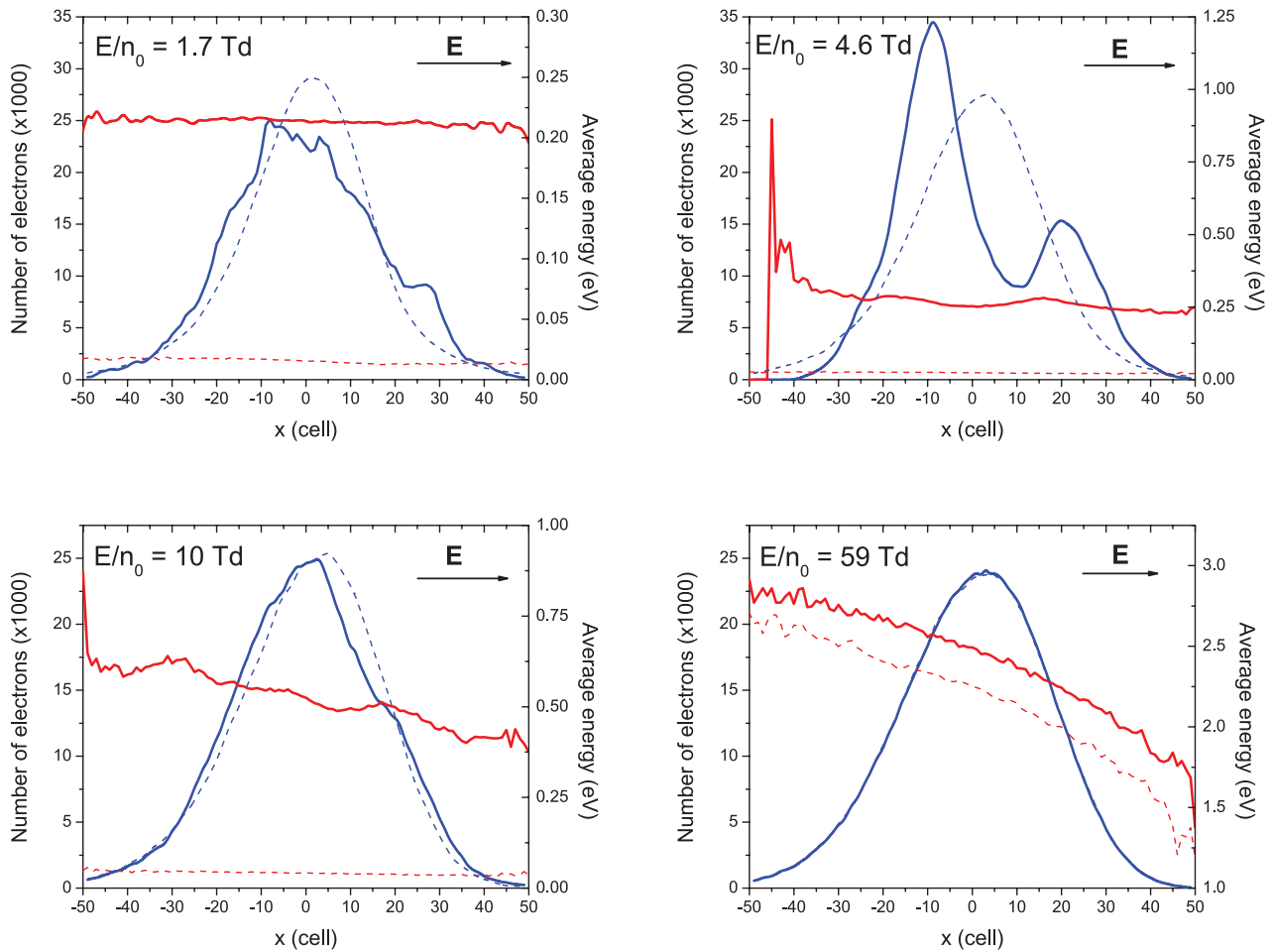


Figure 8. Spatial profile of electrons (blue curves) and spatially resolved averaged energy (red curves) at four different E/n_0 in CF_3I . Full lines denote the results when electron attachment is treated as a non-conservative process, while the dashed lines represent our results when electron attachment is treated as a conservative inelastic process with zero energy loss.

attachment heating while for higher E/n_0 this follows from the explicit effects of ionization. As mentioned above, when transport processes are greatly affected by attachment heating the slower electrons at the back of the swarm are consumed at a faster rate than those at the front of the swarm. Thus, in the case of drift, the electron attachment acts to push the centre of mass forward, increasing the bulk drift velocity above its flux component. For higher E/n_0 when ionization takes place, the ionization rate is higher for faster electrons at the front of the swarm than for slower electrons at the back of the swarm. As a result, electrons are preferentially created at the front of the swarm which results in a shift in the centre of mass. Of course, this physical picture is valid if collision frequency for ionization is an increasing function of electron energy. This is true for electrons in both SF_6 and CF_3I . The explicit effects of electron attachment are much stronger than those induced by ionization. When ionization is dominant non-conservative process, the differences between two sets of data are within 30% for both gases. When attachment dominates ionization, however, then the discrepancy between two sets of data might be almost two orders of magnitude, as for electrons in SF_6 in the limit of the lowest E/n_0 .

The flux drift velocity is a monotonically increasing function of E/n_0 while the bulk component behaves in a qualitatively

different fashion. A prominent feature of electron drift in SF_6 and CF_3I is the presence of a very strong NDC in the profile of the bulk drift velocity. On the other hand, a decrease in the flux drift velocity with increasing E/n_0 has not been observed. Such behavior is similar of the recently observed NDC effect for positrons in molecular gases [78, 79] where Positronium (Ps) formation plays the role of electron attachment.

In order to provide physical arguments for an explanation of NDC in the bulk drift velocity, in figure 8 we show the spatial profile and spatially resolved average energy of electrons in CF_3I . Calculations are performed for four different values of E/n_0 as indicated in the graph. The direction of the applied electric field is also shown. Two fundamentally different scenarios are discussed: (1) the electron attachment is treated as a conservative inelastic process with zero energy loss, and (2) the electron attachment is treated regularly, as a true non-conservative process. The first scenario is made with the aim of illustrating that NDC is not primarily caused by the shape of cross section for attachment but rather by the synergism of explicit and the implicit effects of the number changing nature of the process on electron transport. Sampling of spatially resolved data in our Monte Carlo simulations is performed using the continuous rescaling. The continuous rescaling produces smoother curves and in most cases it is more reliable

as compared to the discrete rescaling and swarm duplication. The results of the first scenario are presented by dashed lines while the second scenario where electron attachment is treated as a true non-conservative process, is represented by full lines.

When electron attachment is treated as a conservative inelastic process, the spatial profile of electrons has a well defined Gaussian profile with a small bias induced by the effect of electric field. The non-symmetrical feature of spatial profile is further enhanced with increasing E/n_0 . While for lower E/n_0 the spatial variation of the average energy is relatively low, for higher E/n_0 , e.g. for E/n_0 of 59 Td the slope of the average energy is quite high, indicating that the electron swarm energy distribution is normally spatially anisotropic. It is important to note that there are no imprinted oscillations in the spatial profile of the electrons or in the profile of the average energy which is a clear sign that the collisional energy loss is governed essentially by 'continuous' energy loss processes [32].

When electron attachment is treated as a true non-conservative process, the spatial profile and the average energy of electrons are drastically changed. For all considered reduced electric fields spatially resolved average energy is greater as compared to the case when electron attachment is treated as a conservative inelastic process. For E/n_0 of 1.7 and 4.6 Td the spatial profiles of electrons depart from a typical Gaussian shape. For 1.7 Td there is very little spatial variation in the average energy along the swarm. When $E/n_0 = 4.6$ Td, however, the spatial profile is skewed, asymmetric and shifted to the left. This shift corresponds approximately to the difference between bulk drift velocities in the two scenarios. We observe that the trailing edge of the swarm is dramatically cut off while the average energy remains essentially unaltered. At the leading edge of the swarm, however, we observe a sharp jump in the average energy which is followed by a sharp drop-off. In addition, the height of spatial profile is significantly increased in comparison to the Gaussian profile of the swarm when electron attachment is treated as a conservative inelastic process. For higher E/n_0 the signs of explicit effects of electron attachment are still present but are significantly reduced. For $E/n_0 = 10$ Td the spatial dependence of the average energy is almost linear with a small jump at the leading edge of the swarm. Comparing trailing edges of the swarms at 4.6 and 10 Td we see that for higher electric field the spatial profile of electrons is by far less cut off. This suggests that for increasing E/n_0 there are fewer and fewer electrons that are consumed by electron attachment. Finally, for $E/n_0 = 59$ Td the spatial profile of electrons is exactly the same as the profile obtained under conditions when electron attachment is treated as a conservative inelastic process.

The spatially resolved attachment rates are displayed in figure 9 and are calculated under the same conditions as for the spatial profile of the electrons and spatially averaged energy. We see that the attachment rate peaks at the trailing edge of the swarm where the average energy of the electrons is lower. Attachment loss of these lower energy electrons causes a forward shift to the swarm centre of mass, with a corresponding increase in the bulk drift velocity. For increasing E/n_0 , the spatially resolved attachment rate coefficients are reduced and linearly decrease from the trailing edge towards the leading

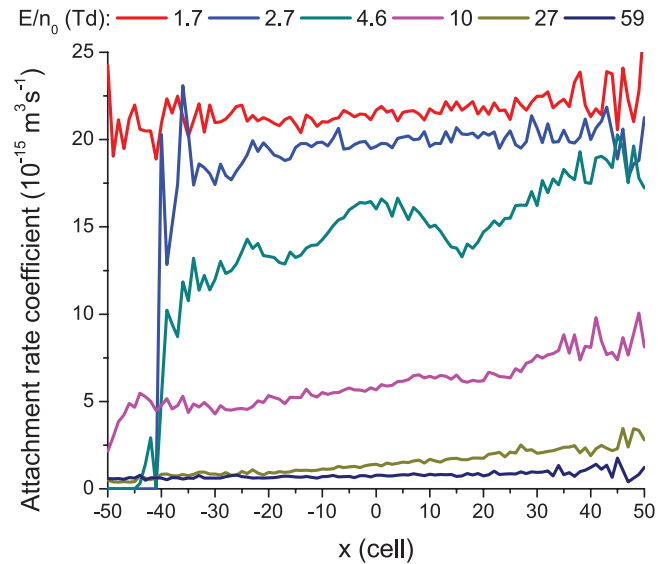


Figure 9. Spatially resolved attachment rate coefficient for a range of E/n_0 as indicated on the graph. Calculations are performed for electrons in CF_3I .

part of the swarm. At the same time the electrons at the leading edge of the swarm have enough energy to undergo ionization. This suggests much less explicit influence of electron attachment on the electron swarm behavior. As a consequence, NDC is removed from the profile of the bulk drift velocity.

In addition to the explicit effects of electron attachment there are implicit effects due to energy specific loss of electrons, which changes the swarm energy distribution as a whole, and thus indirectly changes the swarm flux. Generally speaking, it is not possible to separate the explicit from implicit effects, except by analysis with and without the electron attachment. Using these facts as motivational factors, in figure 10 we show the electron energy distribution functions for the same four values of E/n_0 considered above. The electron energy distribution functions are calculated when electron attachment is treated as a true non-conservative process (full line) and under conditions when electron attachment is assumed to be a conservative inelastic process (dashed line). As for electrons in SF_6 , we observe a 'hole burning' effect in the energy distribution function which is certainly one of the most illustrative examples of the implicit effects. Likewise, we see that the high energy tail of the distribution function falls off very slowly even slower than for Maxwellian. Under these circumstances, when the actual distribution function significantly deviates from a Maxwellian, the numerical schemes for solving the Boltzmann equation in the framework of moment methods usually fail. Indeed, for E/n_0 less than approximately 20 Td we have found a sudden deterioration in the convergence of the transport coefficients which was most pronounced for the bulk properties. Furthermore, we see that the 'hole burning' effect is not present when electron attachment is treated as a conservative inelastic process. The lower energy part of the distribution function is well populated while high energy part falls off rapidly. For increasing E/n_0 and when electron attachment is treated as a true non-conservative process, the effect of hole burning is reduced markedly while

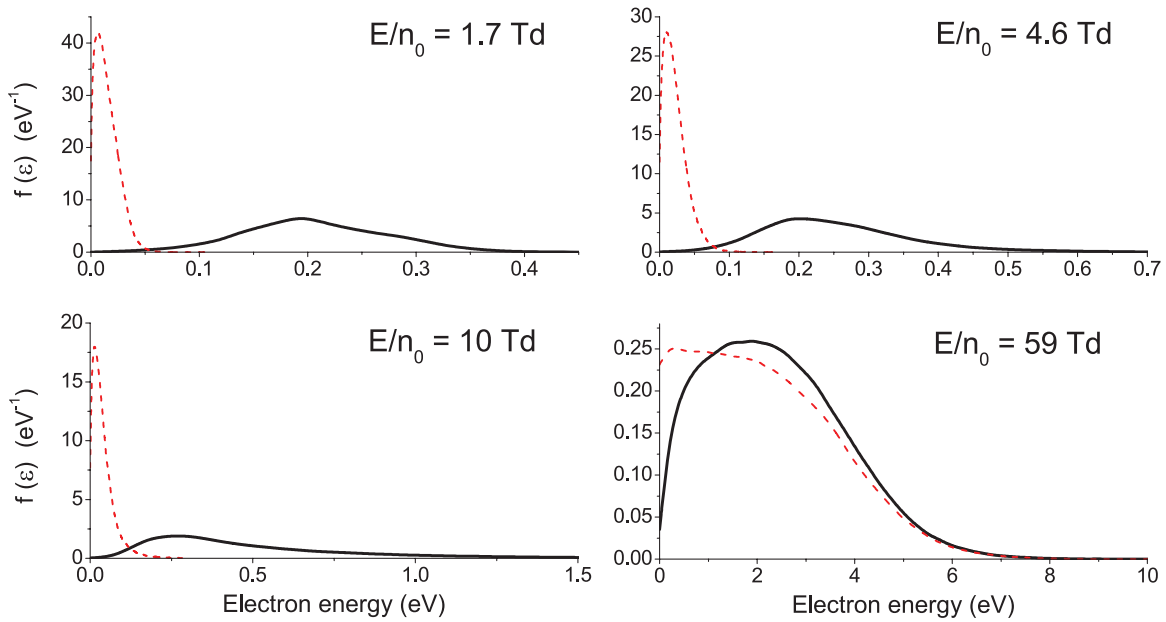


Figure 10. Energy distribution functions for four different E/n_0 for electrons in CF_3I . Black lines denote the results when electron attachment is treated as non-conservative process while dashed red lines represent our results when electron attachment is treated as a conservative inelastic process.

the high energy part of the distribution function coincides with the corresponding one when electron attachment is treated as a conservative inelastic process.

Before embarking on a discussion of our results for diffusion coefficients, one particular point deserves more mention. NDC phenomenon in the bulk drift velocity has not been experimentally verified, neither for SF_6 nor for CF_3I . On the other hand, as we have already seen, the two entirely different theoretical techniques for calculating the drift velocity predict the existence of the phenomenon. Thus, it would be very useful to extend the recent measurements of the drift velocity in both SF_6 and CF_3I to lower E/n_0 with the aim of confirming the existence of NDC. On the other hand, such measurements are most likely very difficult, even impossible due to rapid losses of electron density in experiment.

3.1.3. Diffusion coefficients. Variations of the longitudinal and transverse diffusion coefficients with E/n_0 for electrons in SF_6 are displayed in figures 11 and 12, respectively. From the E/n_0 -profiles of the longitudinal and transverse flux diffusion coefficients, we observe that different rescaling procedures for Monte Carlo simulations agree very well. For the bulk components, the agreement is also very good for intermediate and higher E/n_0 and only in the limit of the lowest E/n_0 the agreement is deteriorated. Over the range of E/n_0 considered we see that there is an excellent agreement between continuous and discrete rescaling.

Comparing Monte Carlo and BOLSIG+ results, the deviations are clearly evident. They might be attributed to the inaccuracy of the two term approximation of the Boltzmann equation which is always considerably higher for diffusion than for the drift velocity. For higher E/n_0 , inelastic collisions are significant and the distribution function deviates substantially from isotropy in velocity space. In these circumstances,

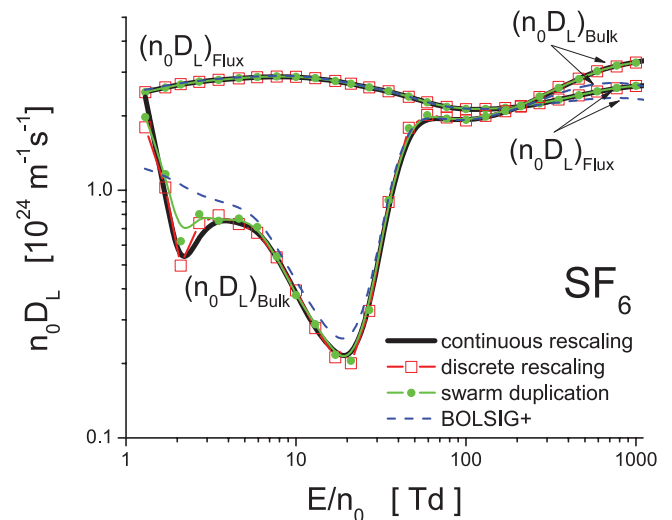


Figure 11. Variation of the longitudinal diffusion coefficient with E/n_0 for electrons in SF_6 . Monte Carlo results using three different techniques for electron number density compensation are compared with the BOLSIG+ results.

the two term approximation of the Boltzmann equation fails and multi-term Boltzmann equation analysis is required. For lower E/n_0 , however, the role of inelastic collisions is of less significance, but still discrepancies between the BOLSIG+ and Monte Carlo results are clearly evident, particularly for the longitudinal diffusion coefficient. This suggests that further analyses of the impact of electron attachment on the distribution function in velocity space of electrons in SF_6 would be very useful.

From the profiles of the longitudinal diffusion coefficient at lower and intermediate values of E/n_0 we observe the following interesting points. In contrast to drift velocity (and transverse diffusion coefficient shown in figure 12) we see

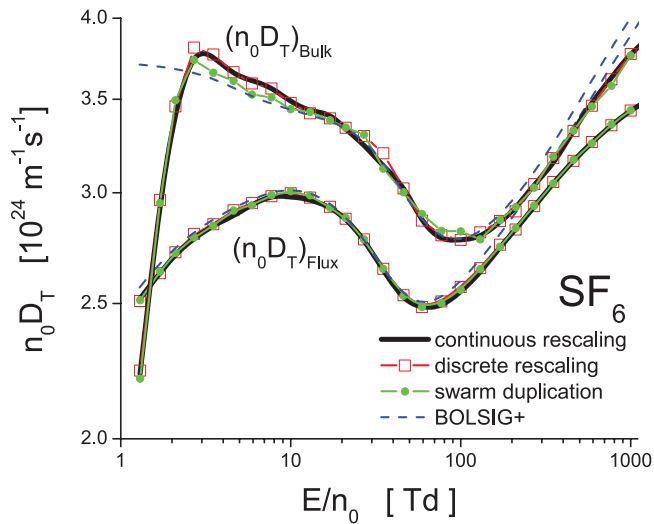


Figure 12. Variation of the transverse diffusion coefficient with E/n_0 for electrons in SF_6 . Monte Carlo results using three different techniques for electron number density compensation are compared with the BOLSIG+ results.

that the bulk diffusion coefficient is smaller than the corresponding flux component. This indicates that the decrease in electron numbers due to attachment weakens diffusion along the field direction. As already discussed, attachment loss of electrons from the trailing edge of the swarm causes a forward shift to the swarm centre of mass, with the corresponding increases in the bulk drift velocity and mean energy. The same effects result in an enhancement of the flux longitudinal diffusion. It should be noted that when attachment heating takes place, the opposite situation (bulk is higher than flux) has also been reported [25]. This is a clear sign that the energy dependence of the cross sections for electron attachment is of primary importance for the analysis of these phenomena. For higher E/n_0 , however, where the contribution of ionization becomes important, we observe that the diffusion is enhanced along the field direction, e.g. the bulk dominates the flux. This is always the case if the collision frequency for ionization is an increasing function of the electron energy, independently of the gaseous medium considered.

From the profiles of the transverse diffusion coefficient the bulk values are greater than the corresponding flux values over the range of E/n_0 considered in this work. Only in the limit of the lowest E/n_0 the opposite situation holds: the flux is greater than the bulk. In contrast to the longitudinal diffusion, spreading along the transverse directions is entirely determined by the thermal motion of the electrons. The flux of the Brownian motion through a transverse plane is proportional to the speed of the electrons passing through the same plane. Therefore, the higher energy electrons contribute the most to the transversal expansion, so attachment heating enhances transverse bulk diffusion coefficient.

Figures 13 and 14 show the variations of the longitudinal and transverse diffusion coefficients with E/n_0 for electrons in CF_3I , respectively. From the E/n_0 -profiles of the bulk diffusion coefficients we observe an excellent agreement between different rescaling procedures for $E/n_0 > 10$ Td. The same applies for the flux component of the longitudinal diffusion.

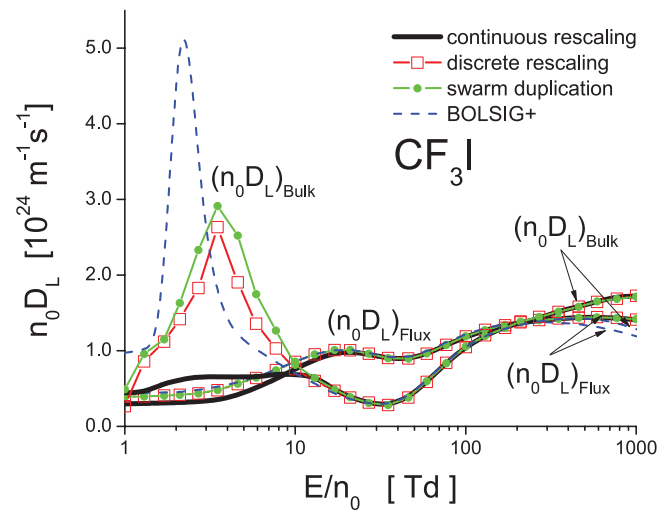


Figure 13. Variation of the longitudinal diffusion coefficient with E/n_0 for electrons in CF_3I . Monte Carlo results using three different techniques for electron number density compensation are compared with the BOLSIG+ results.

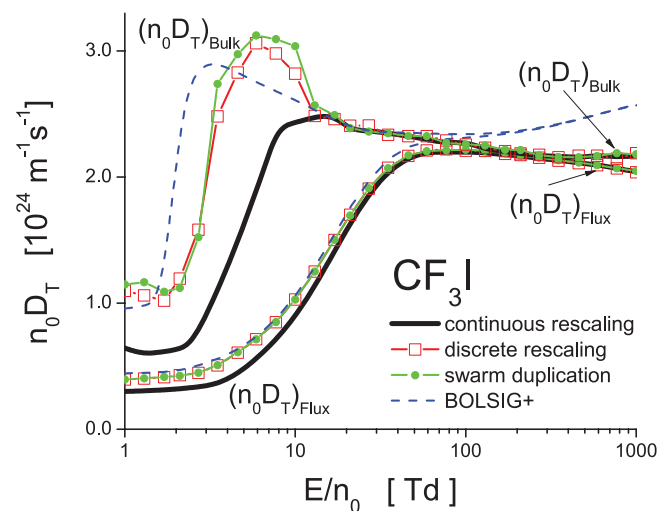


Figure 14. Variation of the transverse diffusion coefficient with E/n_0 for electrons in CF_3I . Monte Carlo results using three different techniques for electron number density compensation are compared with the BOLSIG+ results.

For $E/n_0 < 10$ Td the agreement is poor for bulk components, particularly between the continuous rescaling from one side and discrete rescaling and/or swarm duplication from the other side. The agreement is better for the flux components.

Comparing Monte Carlo and BOLSIG+ results, we see that the maximum error in the two term approximation, for both diffusion coefficients occurs at lower and higher E/n_0 . In contrast to SF_6 , CF_3I has rapidly increasing cross sections for vibrational excitations in the same energy region where the cross section of momentum transfer in elastic collisions decreases with the electron energy. Under these conditions, the energy transfer is increased and collisions no longer have the effect of randomizing the direction of electron motion. As a consequence, the distribution function deviates significantly from isotropy in velocity space and two term approximation of the Boltzmann equation fails.

When considering the differences between the bulk and flux values of diffusion coefficients the situation is much more complex comparing to SF₆. From the E/n_0 -profiles of the longitudinal diffusion coefficient one can immediately see that for lower and higher E/n_0 , the bulk is greater than the corresponding flux values while at intermediate E/n_0 the opposite situation holds: the flux is greater than the bulk. The behavior of the transverse diffusion coefficient is less complex, as over the entire of E/n_0 the bulk is greater than the corresponding flux values.

As we have demonstrated, in contrast to drift velocity the behavior and differences between the bulk and flux diffusion coefficients is somewhat harder to interpret. This follows from the complexity of factors which contribute to or influence the diffusion coefficients. The two most important factors are the following: (a) the thermal anisotropy effect resulting from different random electron motion in different directions; and (b) the anisotropy induced by the electric field resulting from the spatial variation of the average energy and local average velocities throughout the swarm which act so as to either inhibit or enhance diffusion. Additional factors include the effects of collisions, energy-dependent total collision frequency, and presence of non-conservative collisions. Couplings of these individual factors are always present and hence sometimes it is hard to elucidate even the basic trends in the behavior of diffusion coefficients. In particular, to understand the effects of electron attachment on diffusion coefficients and associated differences between bulk and flux components, the variation in the diffusive energy tensor associated with the second-order spatial variation in the average energy with E/n_0 should be studied. This remains the program of our future work.

3.1.4. Rate coefficients. In figure 15 we show the variation of steady-state Townsend ionization and attachment coefficients with E/n_0 for electrons in SF₆. The agreement between different rescaling procedures and BOLSIG+ code is very good. It is important to note that the agreement is very good, even in the limit of the lowest E/n_0 considered in this work where the electron energy distribution function is greatly affected by electron attachment. The curves show expected increase in α/n_0 and expected decrease in η/n_0 , with increasing E/n_0 . The value obtained for critical electric field is 361 Td which is in excellent agreement with experimental measurements of Aschwanden [80].

In figure 16 we show variation of the steady-state Townsend ionization and attachment coefficients with E/n_0 for electrons in CF₃I. The agreement between different rescaling procedure and BOLSIG+ code is excellent for ionization coefficient. From the E/n_0 -profile of attachment coefficient, we see that the continuous rescaling slightly overestimates the remaining scenarios of computation. The critical electric field for CF₃I is higher than for SF₆. This fact has been recently used as a motivational factor for a new wave of studies related to the insulation characteristics of pure CF₃I and its mixture with other gases, in the light of the present search for suitable alternatives to SF₆. The value obtained for critical electric field in our calculations is 440 Td which is in close agreement with experimental measurements under steady-state [63, 81]

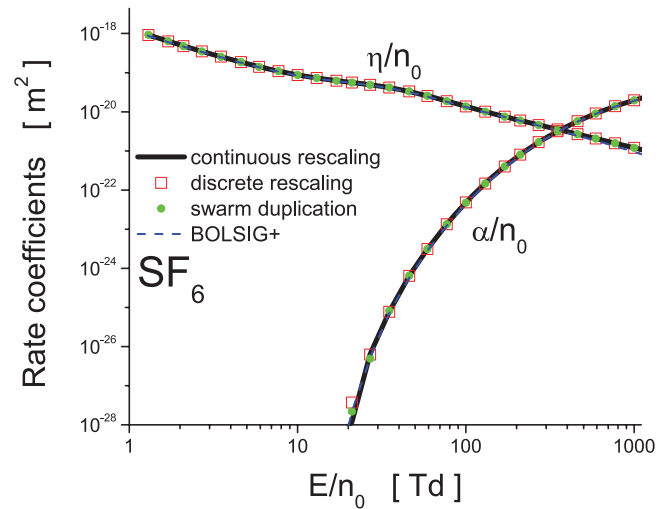


Figure 15. Variation of the rate coefficients with E/n_0 for electrons in SF₆. Monte Carlo results using three different techniques for electron number density compensation are compared with the BOLSIG+ results.

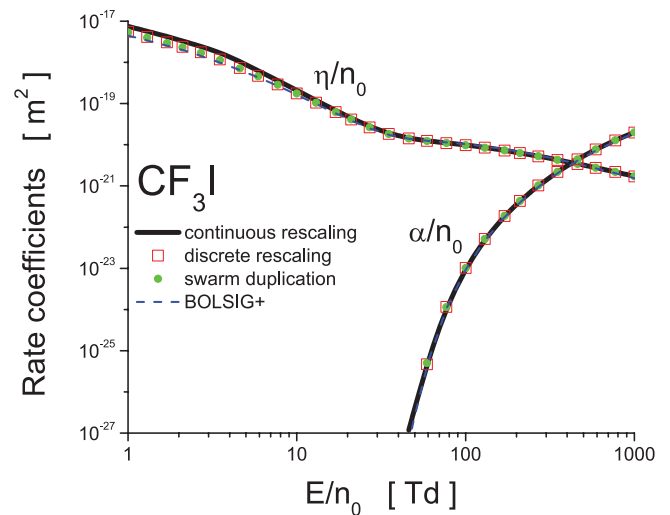


Figure 16. Variation of the rate coefficients with E/n_0 for electrons in CF₃I. Monte Carlo results using three different techniques for electron number density compensation are compared with the BOLSIG+ results.

and pulsed-Townsend [82] conditions, as well as with recent calculations performed by Kawaguchi *et al* [58] and Deng and Xiao [52].

3.2. Recommendations for implementation

In this section, we discuss the main features of the rescaling procedures and we give recommendations on how to use them in future Monte Carlo codes. Based on our experience achieved by simulating the electron transport in SF₆, CF₃I and other attaching gases, we have observed that if correctly implemented the procedures generally agree very well. The agreement between different rescaling procedures is always better for the flux than for the bulk properties. We found a poor agreement for the bulk diffusion coefficients, particularly for the lower E/n_0 while for mean energy, drift velocity and

rate coefficients the agreement is reasonably good. For lower E/n_0 when the distribution function is extremely affected by electron attachment, the agreement between swarm duplication and discrete rescaling is also good. This is not surprising as these two techniques are essentially the same.

In terms of implementation, the Monte Carlo codes can be relatively easily upgraded with the procedures for swarm duplication and/or discrete rescaling. Special attention during the implementation of these procedures should be given to the choice of the length of time steps after which the cloning of the electrons is done. If the length of this time step appears to be too long as compared to the time constant which corresponds to the attachment collision frequency, then the distribution function could be disturbed due to a low statistical accuracy. In other words, depleting certain pockets of the EEDF means that those cannot be recovered at all. On the other hand, if the length of the time steps is too small, the speed of simulation could be significantly reduced. The implementation of the continuous rescaling procedure is somewhat more complicated.

Which procedure is, the most flexible? It is difficult to answer this question because the answer depends on the criteria of flexibility. If the criterion for flexibility is associated with the need for *a priori* estimates which are necessary for setting the simulation, then the technique of continuous rescaling is certainly the most flexible. Once implemented, and thoroughly tested this procedure allows the analysis of electron transport in strongly attaching gases regardless of the energy dependence of the cross section for electron attachment. On the other hand, for the analysis of electron transport in weakly attaching gases, the discrete rescaling is very convenient because it is easier for implementation into the codes and less demanding in terms of the CPU time.

In terms of reliability and accuracy, the comparison of the results obtained for various transport properties using the rescaling procedures for Monte Carlo simulations and the Boltzmann equation codes shows that the rescaling procedures described herein are highly reliable. It should be noted that only the multi term codes for solving the Boltzmann equation may offer the final answer. Restrictions of the TTA for solving the Boltzmann equation were demonstrated many times in the past [7, 31], especially when it comes to the calculations of diffusion coefficients. Testing and benchmarking against other Boltzmann solvers are currently ongoing.

3.3. Experiments in strongly attaching gases: difficulties induced by non-hydrodynamic effects

It must be noted at this point that most processes scale with pressure, so the independence on pressure would be maintained and so would be the equilibration of EEDFs affected by excessive attachment. Most of the processes fall into that category. These processes are best visualized in an infinite uniform environment. Standard swarm experiments are built in such a way that boundaries are not felt over appreciable volume and thus, they mimic hydrodynamic conditions very well. However, going to high E/n_0 requires operating at lower pressures and there the boundaries may be felt over a larger

portion of the volume. In general, whenever boundaries of any kind are introduced selective losses resulting in very different mean free paths of different groups of particles may lead to selective losses. The resulting holes in the distribution may be filled in by collisions, so when considerable selective losses are introduced results may become the pressure dependent (even when the cross section is not dependent on the pressure). The same is true for temporal limitations. For example, if the frequency of collisions is small, so that the mean free time is comparable to the time required to accelerate to energies where cross sections decrease with the electron energy, the runaway effects may be developed. Similar effects may be created due to temporal variations of the field that do not allow full equilibration. The pressure dependence of the results will develop under such conditions (and so would the dependence on the size of the vessel). The development of a non-hydrodynamic theory for solving the Boltzmann equation is difficult and the best solution is a Monte Carlo simulation technique. For that reason, rescaling procedures are essential in modeling of the non-hydrodynamic (non-local) development of charged particle ensembles.

Experiments in gases with a very large attachment (typically at low energies) may be difficult to carry out due to a large loss of electrons. The fact that experiments in diluted gas mixtures of such gases may be feasible, means that cross sections may be obtained. Yet, one should be aware of two main problems. Even in such mixtures and depending on the size of the experiment, attachment may be high enough to induce depletion of the distribution function thus making results pressure dependent or abundance dependent. If one wants to extend the calculations to pure attaching gas for smaller vessels and pressures, one needs to be aware that only techniques that take full non-hydrodynamic description of the swarm development, are required. Similar effects have been observed in gases always associated with strong attachment such as oxygen [76] and water vapor [83]. In any case, the critical effects that include NDC for bulk drift velocity as a result of excessive loss of electrons in attachment can be observed in gases like SF_6 and CF_3I based on hydrodynamic expansion and even based on the two term theory provided that theory takes into account the explicit and implicit non-conservative effects of the attachment.

4. Conclusion

In this paper, we have presented the development, implementation and benchmarking of the rescaling procedures for Monte Carlo simulations of electron transport in strongly attaching gases. The capabilities of the rescaling procedures have been described by systematic investigation of the influence of electron attachment on transport coefficients of electrons in SF_6 and CF_3I . Among many important points, the key results arising from this paper are:

- (1) We have presented two distinctively different methods for compensation of electrons in Monte Carlo simulations of electron transport in strongly attaching gases, e.g. the discrete and the continuous procedures. In order to avoid the

somewhat arbitrary choice of the fictitious ionization rate, we have extended the continuous rescaling procedure, initially developed by Li *et al* [61], by introducing a time-dependent collision frequency for the fictitious ionization process.

- (2) One of the initial motivating factors for this work was to provide accurate data for transport properties of electrons in SF₆ and CF₃I which are required as input in fluid models of plasma discharges. In this work, for the first time, we have calculated the mean energy, drift velocity and diffusion coefficients as well as rate coefficients for lower E/n_0 for electrons in SF₆ and CF₃I.
- (3) We have demonstrated the differences which can exist between the bulk and flux transport coefficients and the origin of these differences. Our study has shown that the flux and bulk transport properties can vary substantially from one another, particularly in the presence of intensive attachment heating. Thus, one of the key messages of this work is that theories which approximate the bulk transport coefficients by the flux are problematic and generally wrong.
- (4) We have demonstrated and interpreted physically the phenomenon of the anomalous behavior of the mean energy of electrons in SF₆, in which the mean energy is reduced for increasing E/n_0 . The phenomenon was associated with the interplay between attachment heating and inelastic cooling. The same phenomenon has not been observed for electrons in CF₃I indicating that the role of the cross sections is vital.
- (5) We have explained and identified a region of NDC in the bulk drift velocity, originating from the explicit influence of electron attachment. The phenomenon has been explained using the concept of spatially-resolved transport properties along the swarm.
- (6) The publicly available two term Boltzmann solver, BOLSIG+, has been shown to be accurate for calculations of mean energy, drift velocity and rate coefficients for electrons in SF₆ and CF₃I. On the other hand, significant differences between our Monte Carlo and BOLSIG+ results for diffusion coefficients have been observed, particularly for electrons in CF₃I in the limit of the lowest E/n_0 considered in this work.

Various rescaling procedures for Monte Carlo simulations described in this work have recently been applied to modeling of electron transport in strongly attaching gases under the influence of time-dependent electric and magnetic fields. It will be challenging to investigate the synergism of magnetic fields and electron attachment in radio-frequency plasmas. Likewise, the remaining step to be taken, is to apply the rescaling procedures presented in this work to investigate the influence of positronium formation on the positron transport properties. This remains the focus of our future investigation. Finally, we hope that this paper will stimulate further discussion on methods of correct representation of the effects induced by electron attachment on transport properties of electrons in strongly attaching gases.

Acknowledgments

The authors acknowledge support from MPNTRRS Projects OI171037 and III41011.

References

- [1] Christophorou L G and Olthoff J K 2004 *Fundamental Electron Interactions with Plasma Processing Gases* (New York: Springer)
- [2] Makabe T and Petrović Z Lj 2014 *Plasma Electronics: Applications in Microelectronic Device Fabrication* (New York: CRC Press)
- [3] Christophorou L G and Pinnaduwege L A 1990 *IEEE Trans. Electr. Insul.* **25** 55
- [4] Rolandi L, Riegler W and Blum W 2008 *Particle Detection with Drift Chambers* (Berlin: Springer)
- [5] Sauli F 2014 *Gaseous Radiation Detectors* (Cambridge: Cambridge University Press)
- [6] Bošnjaković D, Petrović Z Lj, White R D and Dujko S 2014 *J. Phys. D: Appl. Phys.* **47** 435203
- [7] Petrović Z Lj, Dujko S, Marić D, Malović G, Nikitović Ž, Šašić O, Jovanović J, Stojanović V and Radmilović-Radjenić M 2009 *J. Phys. D: Appl. Phys.* **42** 194002
- [8] Petrović Z Lj, Šuvakov M, Nikitović Ž, Dujko S, Šašić O, Jovanović J, Malović G and Stojanović V 2007 *Plasma Sources Sci. Technol.* **16** S1
- [9] Huxley L G H and Crompton R W 1974 *The Drift and Diffusion of Electrons in Gases* (New York: Wiley)
- [10] Christophorou L G, McCorkle D L and Anderson V E 1971 *J. Phys. B: At. Mol. Phys.* **4** 1163
- [11] Phelps A V and van Brunt R J 1988 *J. Appl. Phys.* **64** 4269
- [12] Christophorou L G and Olthoff J K 2000 *J. Phys. Chem. Ref. Data* **29** 267
- [13] Jarvis G K, Kennedy R A and Mayhew C A 2001 *Int. J. Mass Spectrom.* **205** 253
- [14] Dahl D A and Franck C M 2013 *J. Phys. D: Appl. Phys.* **46** 445202
- [15] Rabie M, Haefliger P, Chachereau A and Franck C M 2015 *J. Phys. D: Appl. Phys.* **48** 075201
- [16] Hunter S R and Christophorou L G 1984 *J. Chem. Phys.* **80** 6150
- [17] Novak J P and Frechette M F 1988 *J. Appl. Phys.* **63** 2570
- [18] Hunter S R, Carter J G and Christophorou L G 1988 *Phys. Rev. A* **38** 58
- [19] Petrović Z Lj, Wang W C and Lee L C 1988 *J. Appl. Phys.* **64** 1625
- [20] Petrović Z Lj, Wang W C, Suto M, Han J C and Lee L C 1990 *J. Appl. Phys.* **67** 675
- [21] Raju G G 2006 *Gaseous Electronics: Theory and Practice* (New York: CRC Press)
- [22] Raju G G 2012 *Gaseous Electronics: Tables, Atoms, and Molecules* (New York: CRC Press)
- [23] Cavalleri G 1969 *Phys. Rev.* **179** 186
- [24] Petrović Z Lj and Crompton R W 1985 *J. Phys. B: At. Mol. Phys.* **17** 2777
- [25] Ness K F and Robson R E 1986 *Phys. Rev. A* **34** 2185
- [26] Nolan A M, Brennan M J, Ness K F and Wedding A B 1997 *J. Phys. D: Appl. Phys.* **30** 2865
- [27] Dujko S, Raspopović Z M, Petrović Z Lj and Makabe T 2003 *IEEE Trans. Plasma Sci.* **31** 711
- [28] White R D, Robson R E and Ness K F 1999 *Phys. Rev. E* **60** 7457
- [29] Dujko S, Ebert U, White R D and Petrović Z Lj 2011 *Japan J. Appl. Phys.* **50** 08JC01
- [30] Robson R E 1991 *Aust. J. Phys.* **44** 685

- [31] White R D, Robson R E, Dujko S, Nicoletopoulos P and Li B 2009 *J. Phys. D: Appl. Phys.* **42** 194001
- [32] Dujko S, White R D, Raspopović Z M and Petrović Z Lj 2012 *Nucl. Instrum. Methods Phys. Res. B* **279** 84
- [33] Robson R E, White R D and Petrović Z Lj 2005 *Rev. Mod. Phys.* **77** 1303
- [34] Dujko S, Markosyan A H, White R D and Ebert U 2013 *J. Phys. D: Appl. Phys.* **46** 475202
- [35] Markosyan A H, Dujko S and Ebert U 2013 *J. Phys. D: Appl. Phys.* **46** 475203
- [36] Bletzinger P 1990 *J. Appl. Phys.* **67** 130
- [37] Stoffels E, Stoffels W, Venderm D, Haverlaag M, Kroesen G M W and de Hoog F J 1995 *Contrib. Plasma Phys.* **35** 331
- [38] Chabert P and Sheridan T E 2000 *J. Phys. D: Appl. Phys.* **33** 1854
- [39] Kono A 2002 *Appl. Surf. Sci.* **192** 115
- [40] Zhao S X, Gao F, Wang Y N and Bogaerts A 2012 *Plasma Sources Sci. Technol.* **21** 025008
- [41] Chabert P, Lichtenberg A J, Lieberman M A and Marakhtanov A M 2003 *J. Appl. Phys.* **94** 831
- [42] Robson R E 1986 *J. Chem. Phys.* **85** 4486
- [43] Vrhovac S B and Petrović Z Lj 1996 *Phys. Rev. E* **53** 4012
- [44] Yousfi M, Segur P and Vassiliadis T 1985 *J. Phys. D: Appl. Phys.* **18** 359
- [45] Itoh H, Miurat Y, Ikuta N, Nakao Y and Tagashira H 1988 *J. Phys. D: Appl. Phys.* **21** 922
- [46] Itoh H, Kawaguchi M, Satoh K, Miura Y, Nakano Y and Tagashira H 1990 *J. Phys. D: Appl. Phys.* **23** 299
- [47] Itoh H, Matsumura T, Satoh K, Date H, Nakano Y and Tagashira H 1993 *J. Phys. D: Appl. Phys.* **26** 1975
- [48] Frechette M F and Novak J P 1987 *J. Phys. D: Appl. Phys.* **20** 438
- [49] Pinheiro M J and Loureiro J 2002 *J. Phys. D: Appl. Phys.* **35** 3077
- [50] Tezcan S S, Akcayol M A, Ozerdem O C and Dincer M S 2010 *IEEE Trans. Plasma Sci.* **38** 2332
- [51] Li X, Zhao H, Wu J and Jia S 2013 *J. Phys. D: Appl. Phys.* **46** 345203
- [52] Deng Y and Xiao D 2014 *Japan J. Appl. Phys.* **53** 096201
- [53] Dujko S, White R D, Petrović Z Lj and Robson R E 2010 *Phys. Rev. E* **81** 046403
- [54] Yousfi M, Hennad A and Alkaa A 1994 *Phys. Rev. E* **49** 3264
- [55] Dincer M S and Gaju G R 1983 *J. Appl. Phys.* **54** 6311
- [56] Dincer M S, Ozerdem O C and Bektas S 2007 *IEEE Trans. Plasma Sci.* **35** 1210
- [57] Satoh K, Itoh H, Nakano Y and Tagashira H 1988 *J. Phys. D: Appl. Phys.* **21** 931
- [58] Kawaguchi S, Satoh K and Itoh H 2014 *Eur. Phys. J. D* **68** 100
- [59] Rapopović Z M, Sakadžić S, Bzenić S and Petrović Z Lj 1999 *IEEE Trans. Plasma Sci.* **27** 1241
- [60] Dyatko N A and Napartovich A P 1999 *J. Phys. D: Appl. Phys.* **32** 3169
- [61] Li Y M, Pitchford L C and Moratz T J 1989 *Appl. Phys. Lett.* **54** 1403
- [62] Mirić J, Šašić O, Dujko S and Petrović Z Lj 2014 *Proc. 27th Summer School and Int. Symp. on the Physics of Ionized Gases (Belgrade)* (Belgrade: Institute of Physics) p 122
- [63] Kimura M and Nakamura Y 2010 *J. Phys. D: Appl. Phys.* **43** 145202
- [64] Mirić J, de Urquijo J, Bošnjaković D, Petrović Z Lj and Dujko S 2016 *Plasma Sources Sci. Technol.* submitted
- [65] Ristivojević Z and Petrović Z Lj 2012 *Plasma Sources Sci. Technol.* **21** 035001
- [66] Dujko S, White R D and Petrović Z Lj 2008 *J. Phys. D: Appl. Phys.* **41** 245205
- [67] Petrović Z Lj, Raspopović Z, Dujko S and Makabe T 2002 *Appl. Surf. Sci.* **192** 1
- [68] Hagelaar G J M and Pitchford L C 2005 *Plasma Sources Sci. Technol.* **14** 722
- [69] Kline L and Siambis J 1972 *Phys. Rev. A* **5** 794
- [70] Kunhardt E and Tzeng Y 1986 *J. Comput. Phys.* **67** 279
- [71] Gallagher J W, Beaty E C, Dutton J and Pitchford L C 1983 *J. Phys. Chem. Ref. Data* **12** 109
- [72] Morrow R 1986 *IEEE Trans. Plasma Sci.* **PS-14** 234
- [73] Ness K F and Makabe T 2000 *Phys. Rev. E* **62** 4083
- [74] White R D, Robson R E, Ness K F and Makabe T 2005 *J. Phys. D: Appl. Phys.* **38** 997
- [75] Skullerud H R 1983 *Aust. J. Phys.* **36** 845
- [76] McMahon D R A and Crompton R W 1983 *J. Chem. Phys.* **78** 603
- [77] Hegerberg R and Crompton R W 1983 *Aust. J. Phys.* **36** 831
- [78] Banković A, Dujko S, White R D, Marler J P, Buckman S J, Marjanović S, Malović G, Garcia G and Petrović Z Lj 2012 *New J. Phys.* **14** 035003
- [79] Banković A, Dujko S, White R D, Buckman S J and Petrović Z Lj 2012 *Nucl. Instrum. Methods B* **279** 92
- [80] Aschwanden Th 1984 *Gaseous Dielectrics IV* ed L G Christophorou and M O Pace (New York: Pergamon) p 24
- [81] Hasegawa H, Date H, Shimozuma M and Itoh H 2009 *Appl. Phys. Lett.* **95** 101504
- [82] de Urquijo J, Juarez A M, Basurto E and Hernandez-Avila J L 2007 *J. Phys. D: Appl. Phys.* **40** 2205
- [83] Robson R E, White R D and Ness K F 2011 *J. Chem. Phys.* **134** 064319

Heating mechanisms for electron swarms in radio-frequency electric and magnetic fields

S Dujko¹, D Bošnjaković¹, R D White² and Z Lj Petrović¹

¹ Institute of Physics, University of Belgrade, Pregrevica 118, 11070 Belgrade, Serbia

² College of Science, Technology Engineering, James Cook University, Townsville 4810, Australia

E-mail: sasa.dujko@ipb.ac.rs

Received 27 March 2015, revised 29 June 2015

Accepted for publication 14 August 2015

Published 23 September 2015



CrossMark

Abstract

Starting from analytical and numerical solutions of the equation for collisionless motion of a single electron in time-varying electric and magnetic fields, we investigate the possible mechanisms for power absorption of electron swarms in neutral gases. A multi term theory for solving the Boltzmann equation is used to investigate the power absorption of electrons in radio-frequency (rf) electric and magnetic fields in collision-dominated regime for Reid's inelastic ramp model gas and molecular oxygen. It is found that the effect of resonant absorption of energy in oscillating rf electric and magnetic fields observed under conditions when collisions do not occur, carries directly over to the case where collisions control the swarm behavior. In particular, we have observed the periodic structures in the absorbed power versus amplitude of the applied rf magnetic field curve which have a physical origin similar to the oscillatory phenomena observed for collisionless electron motion. The variation of the absorbed power and other transport properties with the field frequency and field amplitudes in varying configurations of rf electric and magnetic fields is addressed using physical arguments.

Keywords: electron heating, Boltzmann equation, transport coefficients, electron swarms

(Some figures may appear in colour only in the online journal)

1. Introduction

Studies of electron swarms in neutral gases under the influence of varying configurations of electric and magnetic fields are of interest not only from a theoretical viewpoint but have many important applications such as determination of low-energy electron–molecule cross sections [1, 2], modeling of non-equilibrium plasma discharges, including magnetron sputtering [3, 4], plasma propulsion [5, 6] and inductively coupled plasma [7, 8], and modeling of particle detectors in high-energy physics [9, 10]. A swarm of charged particles is usually defined as an ensemble of charged particles, such as electrons or ions, drifting and diffusing in a background gas under the influence of electric and/or magnetic fields. In plasma physics, this is designated as the free diffusion or test particle limit where charged particle–charged particle interactions and space-charge fields are negligible. In plasma modeling, swarm data obtained under the influence of direct current (dc) electric (and rarely magnetic) fields are generally applied as input in fluid models of magnetized plasma

discharges. In swarm experiments, the applied electric and magnetic fields as well as the properties of the background gaseous medium can be very efficiently controlled, enabling one to perform accurate measurements of transport coefficients. Transport coefficients can be then unfolded to yield information about cross sections for electron scattering which are required as input in kinetic models of plasma discharges. The literature of contemporary theoretical investigation on electron transport in electric and magnetic fields has been summarized in the papers of Petrović *et al* [2, 11], White *et al* [12, 13] and Dujko *et al* [14, 15], with particular emphasis on dc electric and magnetic fields.

For the more general case of alternatively current (ac) electric and magnetic fields, particularly in domain of rf fields crossed at arbitrary phases and angles, there has been comparatively less investigation. The reason is twofold: first, the presence of time-varying magnetic field introduces unavoidable mathematical complexity in theories for solving the Boltzmann equation and second, still it is not entirely clear how to implement time-resolved swarm transport data in fluid

models of magnetized plasma discharges properly. In addition, it is very computationally expensive to store space and time-dependent distribution functions and related transport data and usually the cycle-averaged values for these quantities are employed in the models [16]. Nevertheless, the existence of crossed rf electric and magnetic fields in inductively coupled plasmas, rf magnetrons and in some other types of magnetically enhanced plasma sources have triggered a new wave of studies of the equivalent swarm problem. One of the critical problems in these studies was accurate representation of temporal and spatial non-locality of electron transport in various field configurations [17–20]. Certain aspects of the same problem are addressed by plasma modelers without taking advantage of the recent advances in the physics of swarms. In particular, kinetic phenomena induced by temporal non-locality of electron transport in time-varying fields such as anomalous anisotropic diffusion [21, 22], time-resolved negative differential conductivity [23] and transiently negative diffusivity [24, 25], as well as phenomena induced by the explicit influence of non-conservative collisions such as the absolute negative electron mobility [26], are such examples. The influence of a time-varying magnetic field on electron kinetics was also rarely studied in plasma modeling with the exception of some Particle in Cell models [27–29]. A few authors have considered the $\mathbf{E} \times \mathbf{B}$ transport data into plasma models accurately which in turn have led to a better understanding of the plasma heating for some arrangements of magnetically enhanced/assisted plasma reactors [16, 30]. It was also shown that inclusion of the $\mathbf{E} \times \mathbf{B}$ drift may lead to additional heating of inductively coupled plasmas [31, 32]. Kinetic phenomena induced by temporal and spatial non-locality, their interpretation and physical implications which may arise from their explicit inclusion into plasma models, have given rise to a whole new dimension of swarm physics. The literature of theoretical investigation on electron swarms in rf electric and magnetic fields has been recently summarized in the papers [2, 11, 13, 33], textbook [7] and thesis [34].

In this paper, as a part of our on-going investigations of electron transport in spatially uniform rf electric and magnetic fields, we systematically study the origin and physical mechanisms for electron heating assuming swarm conditions. Preliminary results revealed the existence of periodic structures in the variation of the mean energy with the magnetic field amplitude for certain model gases [35]. This phenomenon was related to the resonant absorption of energy from rf fields by electrons. Similar results have never been observed for electrons in dc electric and magnetic fields, where the mean energy of electrons is always a monotonically decreasing function of magnetic field strength, independent of the gas type and field configuration (except for parallel fields) [12, 14, 15, 36–38] and with the exception of one observation of local peaks in energy for electron swarms in argon [39]. This raises a number of questions: Which physical mechanism controls the power absorption in rf electric and magnetic fields? What is the nature of the periodicity and spacing between individual peaks in the profile of the absorbed power? Does the phenomenon occur for real gases or only for less realistic model gases? What are the implications of this phenomenon for analysis of

power absorption in more realistic plasma sources? In this paper we will try to address some of these issues. In particular, here we do not attempt to analyze the ohmic, and stochastic heating by anomalous skin effect [40–44], and related electrodynamics of electrons in realistic rf plasma sources where many parameters and operating conditions such as pressure, coil design [45, 46] and antenna shape [47], and presence of a substrate [48] as well as gas heating [49] may simultaneously affect the mechanisms for power absorption. Examples of these studies include those attempting to understand the non-local power deposition in inductively coupled plasmas [50–52], rf magnetrons [53] and magnetically enhanced plasmas. Instead we isolate and investigate the electron component of these plasmas under the action of spatially uniform rf electric and magnetic fields. We believe that one of the most critical steps in plasma modeling is testing and verification of plasma models and interpretations against swarm-type models and spatially uniform fields. In particular, due to their complexity and due to difficulties associated with the implementation of boundary conditions to solutions of Boltzmann's equation, kinetic treatments of non-equilibrium plasmas sustained by rf electric and magnetic fields should be benchmarked against the swarm results in the free diffusion limit. On the other hand, one ought to mention the recent study on the non-local response and resonance phenomena associated with electrons subjected to an externally prescribed, spatially varying electrostatic field [54].

This work represents the first multi term Boltzmann equation calculation of power absorption of the electrons in rf electric and magnetic fields under swarm conditions. The study is organized as follows. In section 2, we first consider the collisionless motion of a single electron in oscillating rf electric field, then we proceed to a combined rf electric and dc magnetic fields case, and finally we analyze the motion of a single electron in oscillating rf electric and magnetic fields. In this section, particular emphasis is placed upon the derivation of conditions for resonance. The explicit influence and contribution of collisions between electrons and neutral molecules to power absorption is examined via Boltzmann's equation analysis. In the same section we analyze the role of collisions on the power absorption by considering the electron transport in varying configurations of electric and magnetic fields. Our specific interest here is to investigate relations with the collision free case. Temporal profiles and cycle-averaged values of various transport properties are presented as a function of the field frequency and field amplitudes for Reid's inelastic ramp model and molecular oxygen. In section 4 we discuss the periodic resonant structures that exist in the profiles of the absorbed power and mean energy with magnetic field amplitude in rf electric and magnetic fields.

2. Collisionless motion of a single electron in uniform and time-varying electric and magnetic fields

In this section we are concerned with the collisionless motion of electrons in spatially uniform electric and magnetic fields perpendicular to each other. While some of the

issues discussed here may be well known, it is necessary to present them to build a phenomenology for the effect of the magnetic field in collisionless and collisional conditions. The assumption of motion without collisions is applicable when electron performs a large number of oscillations between two successive collisions. Let us assume that the electric field lies along the z -direction while magnetic field is oriented along the y -direction. The equations of collisionless electron motion are then given by:

$$m \frac{dv_x}{dt} = ev_z B(t), \quad (1)$$

$$m \frac{dv_y}{dt} = 0, \quad (2)$$

$$m \frac{dv_z}{dt} = -e(E(t) + v_x B(t)), \quad (3)$$

where e and m are the electron charge and mass. In what follows the subdivision is made by considering the following cases: (1) time-varying electric and no magnetic field, (2) time-varying electric field and static magnetic field, and (3) time-varying electric and time-varying magnetic fields. The detailed consideration of electron orbits in electric and magnetic fields is beyond the scope of this paper and our focus is placed upon the power absorption by electrons.

2.1. Interaction of electrons with a time-varying electric field

Let us consider now the interaction of electrons with a spatially uniform and time-varying electric field, $E = E_0 \cos \omega t$ in magnetic field free case. Solving equations (1)–(3), we obtain for the three velocity components

$$v_x = v_{x0}, \quad v_y = v_{y0}, \quad v_z = -\frac{eE_0}{m\omega} \sin \omega t + v_{z0}, \quad (4)$$

where v_{x0} , v_{y0} and v_{z0} are initial velocities. Integrating equation (4) we obtain for the displacement of the electron the components

$$x = v_{x0}t + x_0, \quad y = v_{y0}t + y_0, \quad z = \frac{eE_0}{m\omega^2} \cos \omega t + v_{z0}t + z_0, \quad (5)$$

where x_0 , y_0 z_0 are initial positions.

From equations (4) and (5) we see that an electron oscillates at the frequency of the field. The displacement is in phase with the field while the velocity is out of phase by $\pi/2$. Thus if collisions do not occur, then the electric field on the average does no work, on an electron. Using the vector notation, equations (4) and (5) imply that

$$\langle -e\mathbf{E} \cdot \mathbf{v} \rangle = \frac{-eE_0^2}{m\omega} \langle \cos \omega t \sin \omega t \rangle - e\mathbf{E}_0 \cdot \mathbf{v}_0 \langle \sin \omega t \rangle = 0, \quad (6)$$

where angle brackets denote time averaging. Therefore, for collisionless electron motion the energy gained during one half of the field cycle is returned to the field in the other half of the cycle, and no energy can be transferred.

For power absorption to occur there must be some randomization mechanisms that break the regularity and coherence of the electron motion and the $\pi/2$ phase shift between the velocity and electric field. As it is well known, phase mixing required for electrons to achieve net mean energy is due to collisions with the neutral background gas. Collisions between the electrons and neutral molecules perturb the phase, thereby disturbing the purely harmonic course of the electron's oscillations. Alternatively, reflection from a moving field gradient which is common in rf plasmas will also lead to heating even without collisions [8].

The time-averaged power absorbed by the swarm (or plasma or any active medium), p_{abs} , is given by

$$\langle p_{\text{abs}} \rangle = \frac{1}{T} \int_0^T -eN \mathbf{W}(t) \cdot \mathbf{E}(t) dt, \quad (7)$$

where N is the number of electrons in the swarm, $T = 2\pi/\omega$ is the period, and $\mathbf{W}(t)$ is the average velocity. It should be noted that the number of electrons N is not generally conserved due to number changing processes such as electron attachment or ionization. From equation (7) we see that in the time intervals when the drift velocity (or current for plasmas) and electric field have the same sign, the instantaneous power is positive and the electric field pumps energy into the system. Conversely, when the drift velocity and electric field have the opposite signs the instantaneous power is negative and the energy is transferred from an active medium to the external circuit. This suggests that a phase difference between the drift velocity and electric field controls the power absorption of the electrons. This is illustrated schematically in figure 1.

2.2. Interaction of electrons with a time-varying electric field and static magnetic field

In this section we analyze the collisionless motion of electrons in time-varying electric $E = E_0 \cos \omega t$ and static magnetic fields. Solving equations (1)–(3), we obtain for the Cartesian components of the velocity

$$v_x(t) = v_{x0} \cos \Omega t + v_{z0} \sin \Omega t + \frac{e}{m} \frac{E_0 \Omega}{\Omega^2 - \omega^2} (\cos \Omega t - \cos \omega t), \quad (8)$$

$$v_y(t) = v_{y0}, \quad (9)$$

$$v_z(t) = v_{z0} \cos \Omega t - v_{x0} \sin \Omega t - \frac{e}{m} \frac{E_0}{\Omega^2 - \omega^2} (\Omega \sin \Omega t - \omega \sin \omega t), \quad (10)$$

where v_{x0} , v_{y0} and v_{z0} are initial velocities and $\Omega = eB/m$ is the cyclotron frequency of gyration of the electrons about the magnetic field lines. Integrating equations (8)–(10) the displacement components of the electron can be derived. In brief, magnetic field rotates electrons which have elliptical orbits in $(\mathbf{E}, \mathbf{E} \times \mathbf{B})$ plane (e.g. in x - z plane) and the motion of electrons has components at both the cyclotron frequency and at the frequency of the electric field ω . The major characteristics

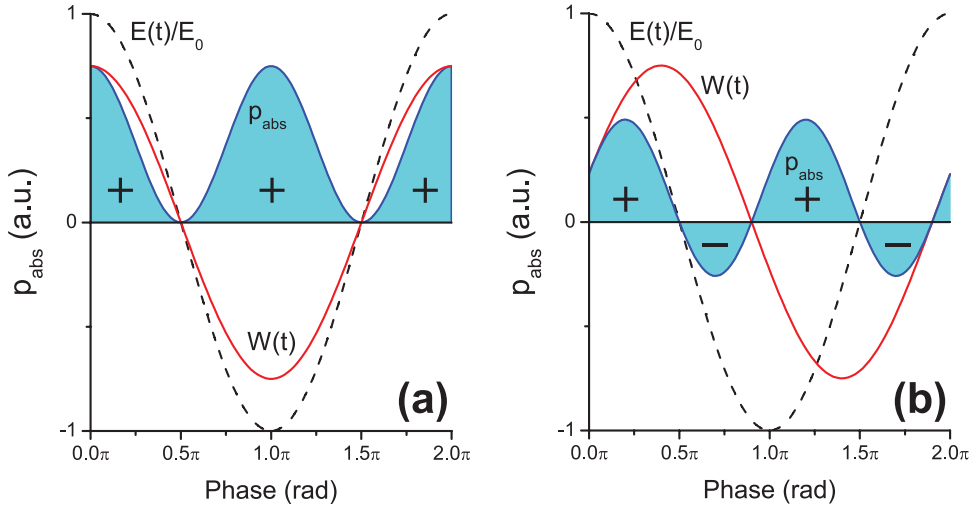


Figure 1. Schematic diagrams of power absorption for charged particle swarms when there is only electric field: (a) no phase difference between the drift velocity and electric field; (b) the phase difference of $2\pi/5$ between the drift velocity and electric field.

of the orbits are dependent on the ratio Ω/ω . In particular for the singular case $\Omega = \omega$, the electron moves in circles of ever increasing radii. This is the well-known cyclotron resonance effect. During this spiral motion the velocity of electron continually increases. Since its kinetic energy increases the electron absorbs energy from the time-varying rf field. This absorption of energy is a resonant process but as we will see later the singular case $\Omega = \omega$ does not correspond to the maximum absorption of energy.

The instantaneous absorbed power for an arbitrary instant of time is given by

$$p_{\text{abs}}(t) = -ev_z(t)E_0 \cos \omega t, \quad (11)$$

while for the time-averaged power absorbed by an electron, we find

$$\langle p_{\text{abs}} \rangle = \frac{1}{T} \int_0^T p_{\text{abs}}(t) dt = \frac{2}{m} \left(\frac{eE_0 \Omega \sin \frac{\pi \Omega}{\omega}}{\Omega^2 - \omega^2} \right)^2. \quad (12)$$

Assuming the field frequency of 500 MHz and an electric field amplitude of 200 Td ($1 \text{ Td} = 1 \times 10^{-21} \text{ Vm}^2$), in figure 2 we display the time-averaged power as a function of the reduced magnetic field strength ($1 \text{ Hx} = 1 \times 10^{-27} \text{ Tm}^3$). In order to facilitate comparisons with the collisional case we shall use E/n_0 and B/n_0 values in both cases to label conditions. Having in mind that when $n_0 = 0$ the ratio E/n_0 and/or B/n_0 is meaningless in collisionless case, it should, however, represent the same field. For example, when $E/n_0 = 200 \text{ Td}$ the electric field is actually 7080 V m^{-1} and when $B/n_0 = 570 \text{ Hx}$ the magnetic field is 20.2 mT. It should be noted that selected values for frequency and field strengths used to calculate the absorbed power, correspond to those used in section 3.4 where collisions occur and where the power absorption is studied for electrons in molecular oxygen.

The resonant and periodic features in the profile of $\langle p_{\text{abs}} \rangle$ with B/n_0 shown in figure 2 are clearly evident. According to equation (12) the positions of minima (or anti-resonances) where the absorbed power is zero, are simply given by

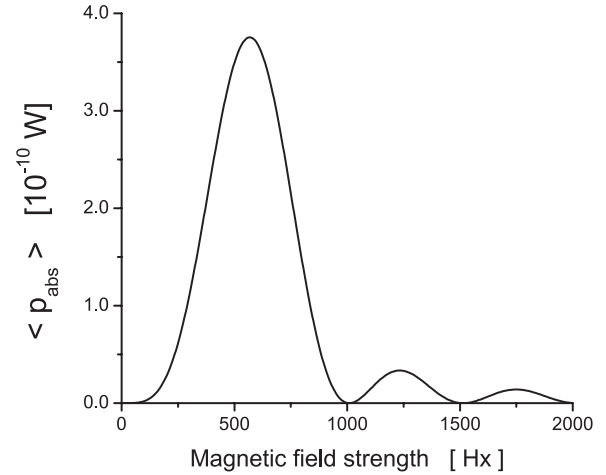


Figure 2. Variation of the time-averaged power for collisionless motion of a single electron with dc magnetic field strength. The amplitude of electric field is 200 Td (which corresponds to 7080 V m^{-1}).

$$\Omega = k \omega, \quad (k \in \mathbf{N}_0 \setminus \{1\}), \quad (13)$$

where $(k \in \mathbf{N}_0 \setminus \{1\})$ indicates all natural numbers including 0 but without 1. This suggests that the spacing in the magnetic fields between two successive minima corresponds to the field frequency.

For positions of peaks we find

$$\frac{\Omega}{\omega} = \frac{1}{\pi} \arccot \left[\frac{\omega(\Omega^2 + \omega^2)}{\pi \Omega(\Omega^2 - \omega^2)} \right] + m, \quad (m \in \mathbf{N}), \quad (14)$$

where m is any natural number. Equation (14) is transcendent and reflect the periodicity of the peak occurrence. It should be noted that the spacing between two successive peaks generally is not constant due to the first term in equation (14). However, if Ω dominates ω the first term approaches to $1/2$ and spacing between two successive peaks now becomes constant. Note that according to equations (13) and (14) the positions of the extremes are determined exclusively by the ratio

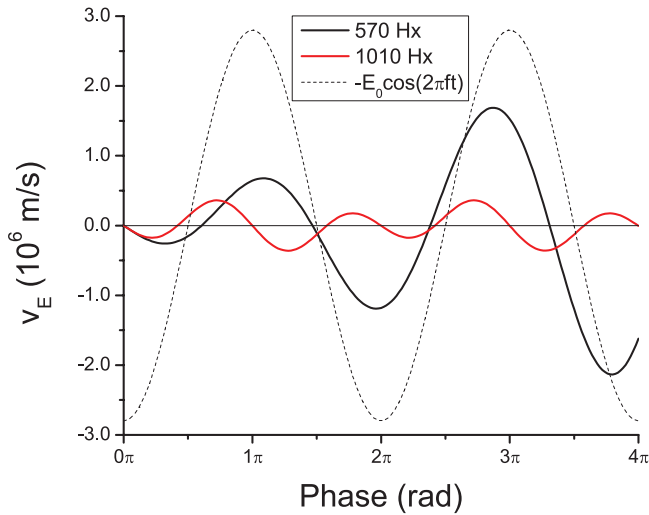


Figure 3. Temporal profiles of the longitudinal velocity for collisionless motion of a single electron in time-varying electric and dc magnetic fields. The amplitude and frequency of the electric field are 200 Td (7080 V m^{-1}) and 500 MHz while magnetic field strengths are 570 (20.2 mT) and 1010 Hx (35.8 mT).

Ω/ω . Moreover, it is interesting to note that for a selected set of initial conditions used to evaluate the power, positions of extremes in variation of $\langle p_{\text{abs}} \rangle$ with B/n_0 are not related to the singular case of cyclotron resonance $\Omega = \omega$.

In figure 3 we show temporal profiles of the longitudinal ($v_E = v_z$) velocity components for magnetic field strengths of 570 and 1010 Hx, respectively. Calculations are performed for the first two periods of the electric field. The values of B/n_0 of 570 and 1010 Hx are deliberately chosen as the first peak and first minimum in the absorbed power versus amplitude of the applied magnetic field curve correspond to these values (see figure 2). For B/n_0 of 1010 Hx, the longitudinal velocity is perfectly periodic, its amplitude stays unaltered and its mean value is zero. Conversely, for B/n_0 of 570 Hx, longitudinal velocity is not periodic, its amplitude continuously increases with time and its mean value is non-zero. This suggests that an electron continuously absorbs the energy from the fields which is demonstrated in figure 4 where the temporal profile of the instantaneous power is shown. In contrast to the $B/n_0 = 570$ Hx case, for B/n_0 which corresponds to the first minimum in the B/n_0 profile of $\langle p_{\text{abs}} \rangle$ (e.g. for 1010 Hx), we see that the mean value of the instantaneous power is zero.

2.3. Interaction of electrons with time-varying electric and time-varying magnetic fields

We now consider the case of time-varying electric and time-varying magnetic fields. The solution of equations (1)–(3) cannot be obtained in a closed-form. Instead, we apply a numerical method described by Dormand and Prince [55] which is based on Runge–Kutta formulas. Various implementations of this method are publicly available. In order to demonstrate the effect of time-varying magnetic fields, equations (1)–(3) are numerically solved assuming $E/n_0 = 200$ Td, $f = 500$ MHz and a range of magnetic field amplitudes

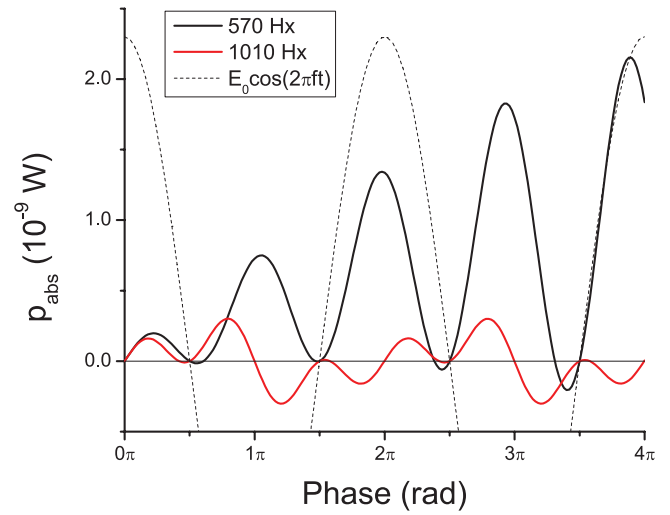


Figure 4. Temporal profiles of the instantaneous power for collisionless motion of a single electron in time-varying electric and dc magnetic fields. The amplitude and frequency of the electric field are 200 Td (7080 V m^{-1}) and 500 MHz while magnetic field strengths are 570 Hx (20.2 mT) and 1010 Hx (35.8 mT).

B_0/n_0 . The same electric field amplitude and field frequency will be applied in section 3.5 where the power absorption is studied for electrons in molecular oxygen under conditions in which the swarm behavior is controlled by collisions.

The solutions calculated using the initial values $v_{x0} = v_{z0} = 0$ are shown in figures 6 and 7. We observe that the mean absorbed power during the first period of the rf field exhibits a strong resonant behavior (figure 5) but the conditions for resonance are not the same as in the case of a static magnetic field. These conditions are discussed in more detail in section 4. The longitudinal velocity (see figure 6) and the instantaneous absorbed power (see figure 7) are calculated using two different magnetic field amplitudes, 950 Hx and 1950 Hx, which correspond to the resonance and anti-resonance, respectively. It is seen that in the case of resonance, the amplitude of the longitudinal velocity (v_E) increases with time and so does the absorbed power. In case of anti-resonance, the energy absorbed during one period is almost zero and the velocity components are periodic functions with essentially constant amplitudes.

3. Motion of electrons in uniform and time-varying electric and magnetic fields in the presence of collisions

3.1. Brief description of theoretical methods

The heating mechanism for electron swarms in the presence of collisions under the action of rf electric and magnetic fields is investigated using a multi term theory for solving the Boltzmann equation. A detail discussion of the Boltzmann equation based calculation used in this work to evaluate power and various electron transport parameters may be found elsewhere [17, 33, 36]. A Monte Carlo simulation technique is also used in this work but as an independent tool with the aim of verifying the sometimes atypical

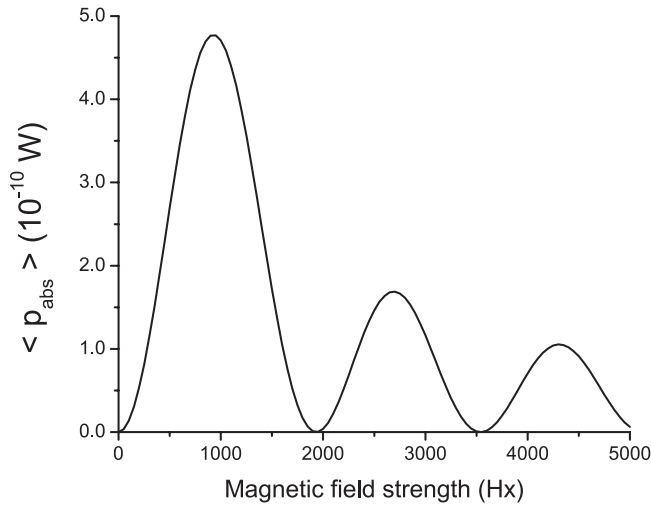


Figure 5. Variation of the time-averaged power for collisionless motion of a single electron with the amplitude of rf magnetic field. The amplitude of the electric field is 200 Td (7080 V m^{-1}) and frequency is set to 500 MHz.

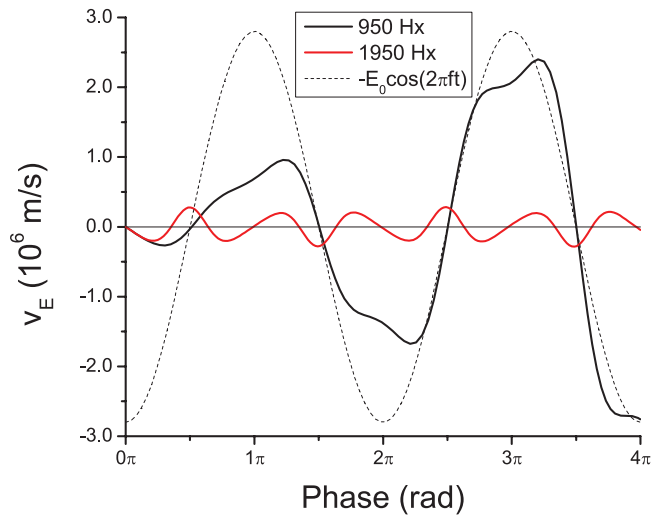


Figure 6. Temporal profiles of the longitudinal velocity for collisionless motion of a single electron in time-varying electric and magnetic fields. The amplitude and frequency of the fields are 200 Td (7080 V m^{-1}) and 500 MHz while magnetic field amplitudes are 950 Hx (33.6 mT) and 1950 Hx (69 mT).

behavior of electron transport properties in rf electric and magnetic fields found in the Boltzmann equation solutions. Some examples of atypical behavior include the negative diffusion coefficients, asymmetry of the drift velocity along the $\mathbf{E} \times \mathbf{B}$ direction with respect to zero value or the presence of additional oscillatory type-behavior in the temporal profiles of drift velocity components and in the profiles of individual diffusion tensor elements. In addition, we use our Monte Carlo method to follow the spatio-temporal development of an electron swarm in the real space which can be very useful to understand the behavior of electron transport properties in rf electric and magnetic fields, particularly if electron transport is greatly affected by non-conservative collisions. For more details on our Monte Carlo technique the reader is referred to [11, 56, 57].

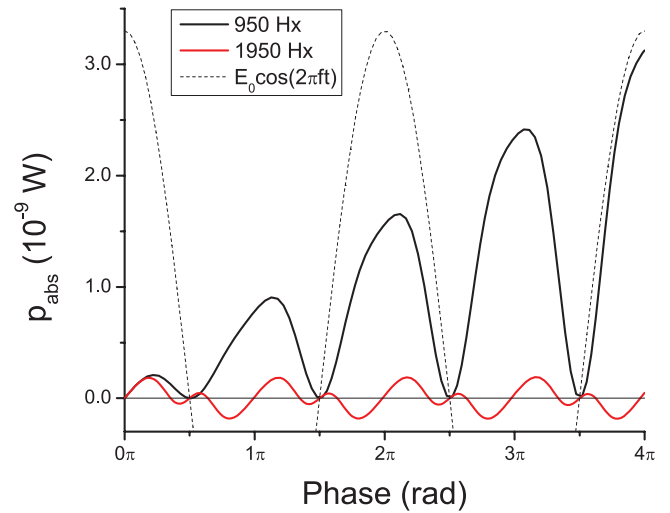


Figure 7. Temporal profiles of the instantaneous power for collisionless motion of a single electron in time-varying electric and magnetic fields. The amplitude and frequency of the electric field are 200 Td (7080 V m^{-1}) and 500 MHz while magnetic field amplitudes are 950 Hx (33.6 mT) and 1950 Hx (69 mT).

3.2. Preliminaries

In order to illustrate the power absorption of electrons in rf electric and magnetic fields under swarm conditions, we first consider Reid's inelastic ramp model [59]. This model has been used many times in the past to test various theories for solving Boltzmann's equation and numerical accuracy of different Monte Carlo codes for electron transport. Various conditions have been considered, including dc electric and magnetic fields [12, 37, 38, 60], as well as time-varying electric and magnetic fields [11, 17, 25, 61] for a variety of field configurations. The details of the model used here are as follows:

$$\begin{aligned} \sigma_m(\epsilon) &= 6 \text{ \AA}^2 \quad (\text{elastic cross section}) \\ \sigma_{inel}(\epsilon) &= \begin{cases} 10(\epsilon - 0.2) \text{ \AA}^2, & \epsilon \geq 0.2 \text{ eV} \quad (\text{inelastic cross section}) \\ 0, & \epsilon < 0.2 \text{ eV} \end{cases} \\ m_0 &= 4 \text{ amu} \\ T_0 &= 0 \text{ K}, \end{aligned} \quad (15)$$

where m_0 and T_0 represent the mass and temperature of the neutral gas particles while ϵ has the units of eV.

The failure of the classical two term approximation for solving Boltzmann's equation for Reid's inelastic ramp model is well-documented [37, 58, 59] and generally $l_{\text{max}} = 4$ is required to achieve convergence of transport coefficients to within 0.5%. On the other hand, as pointed out by White *et al* [66] and Dujko *et al* [17], the application of a magnetic field acts to destroy the anisotropy of the velocity distribution function, consequently inducing enhanced convergence in the l -index. Nevertheless, all calculations are performed assuming $l_{\text{max}} = 4$.

In addition to Reid's inelastic ramp model, we investigate the power absorption of the electrons in molecular oxygen. The cross sections for electron scattering in molecular

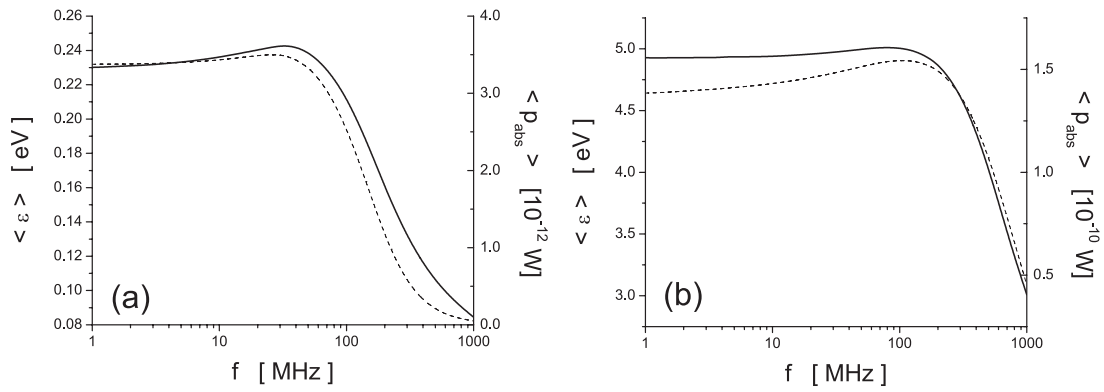


Figure 8. Variation of the cycle-averaged mean energy (full line) and power (dash line) with the frequency of the applied rf electric field. Calculations are performed for (a) Reid's inelastic ramp model ($E_0/n_0 = 14.14$ Td) and (b) molecular oxygen ($E_0/n_0 = 200$ Td).

oxygen are detailed in [62, 63] and displayed in [17]. The same set of cross sections was successfully applied for determination of the steady-state electron transport coefficients and for the studies of the temporal relaxation of electrons when electric and magnetic fields are crossed at arbitrary angles [17, 64]. Calculations are performed for low pressures ($p \leq 1$ Torr) and while the effects of three-body attachment are included in this study, these effects are negligible in the limit of low pressures, as discussed in [65]. The two-term approximation for solving Boltzmann's equation for electrons in molecular oxygen fails due to large cross sections for inelastic collisions and due to their rapid rise with the electron energy. As for Reid's inelastic ramp model, it was found that a value of $l_{\text{max}} = 4$ is required to achieve the convergence to within 1% for the transport properties of interest in the present work.

All calculations are performed for zero gas temperature and the neutral gas number density is fixed to $3.54 \times 10^{22} \text{ m}^{-3}$. The electric field has the following form $E(t)/n_0 = (E_0/n_0) \cos(2\pi ft)$ Td while magnetic field is treated differently. In section 3.3 we consider magnetic field free case while in section 3.4 we consider rf electric and dc magnetic fields. In section 3.5 the electric and magnetic fields are radio-frequency. In particular, if electric and magnetic fields are $\pi/2$ out of phase then magnetic field has the following form $B(t)/n_0 = (B_0/n_0) \sin(2\pi ft)$ Hx, where B_0/n_0 is magnetic field amplitude. All calculations deal exclusively with the $\mathbf{E} \times \mathbf{B}$ configuration.

3.3. Electrons in a time-varying rf electric field in the presence of collisions

In figures 8(a) and (b) we show the cycle-averaged mean energy $\langle \epsilon \rangle$ and cycle-averaged power $\langle p_{\text{abs}} \rangle$ as a function of the frequency of the applied rf electric field for Reid's inelastic ramp model and molecular oxygen, respectively. For both gases the cycle-averaged value of mean energy and the cycle-averaged value of power display a maximal property with frequency. We see that both $\langle \epsilon \rangle$ and $\langle p_{\text{abs}} \rangle$ decrease rapidly for higher frequencies. For Reid's inelastic ramp model the maximum in $\langle \epsilon \rangle$ occurs at approximately 35 MHz while for $\langle p_{\text{abs}} \rangle$ the

maximum is at approximately 27 MHz. For oxygen, the maximum in $\langle \epsilon \rangle$ occurs at higher frequencies, around 100 MHz while $\langle p_{\text{abs}} \rangle$ attains its maximal value around 80 MHz. The instantaneous power relaxes on the time scale of momentum relaxation while the mean energy relaxes according to the time constant for energy transfer in collisions. As discussed by Dujko *et al* [17], for molecular oxygen the relaxation of momentum is a much faster process. As a consequence, the mean energy undergoes a reduction in modulation amplitude and exhibits a phase shift with respect to the electric field in the range of field frequencies for which the drift velocity is almost fully modulated.

Temporal profiles of the mean energy ϵ and drift velocity W as a function of the frequency of the applied rf electric field for electrons in oxygen are shown in figure 9. These profiles are used to evaluate the cycle-averaged values shown in figure 8. For ϵ we note the following: (1) the modulation amplitude decreases with increasing frequency and is essentially time-independent in the limit of the highest frequencies considered in this work; (2) the phase delay of the temporal energy profile with respect to the applied electric field increases with increasing frequency; (3) as already discussed ϵ exhibits a maximal property with frequency; and (4) there is a transition from non-sinusoidal profiles at low frequencies to sinusoidal at higher frequency.

From the profiles of the drift velocity W we note the following: (1) the modulation amplitude shows a maximal property with the field frequency; (2) there are no signs of time-resolved negative differential conductivity; and (3) there is transition from non-sinusoidal profiles at lower frequencies to sinusoidal at higher frequency.

Among the many important points which can be observed in the temporal profiles displayed in figures 9(a) and (b), it is clear that due to collisions between electrons and neutral background molecules the coherence of the electron motion and the $\pi/2$ phase shift between the velocity and electric field is broken. For swarms under the influence of an rf electric field in low-frequency regime, the effective relaxation times for momentum and energy are sufficiently small over all phases of the field, that full relaxation applies and drift velocity follows the field in a quasi-stationary manner. In such a case, the time-averaged power absorbed by the swarm

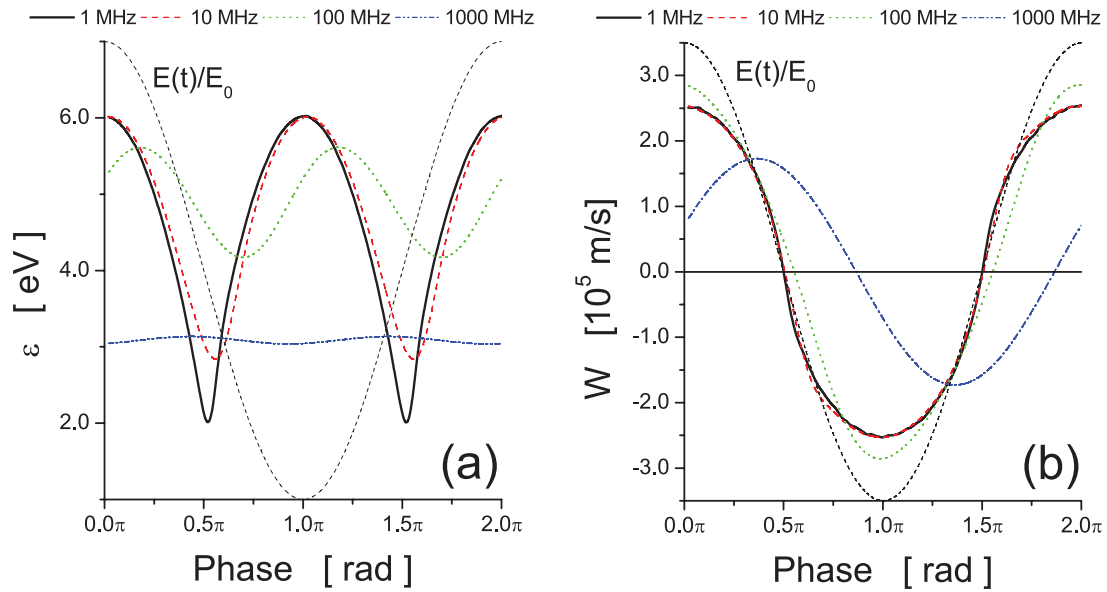


Figure 9. Temporal profiles of the mean energy (a) and drift velocity (b) as a function of the frequency of the applied rf electric field. The amplitude of electric field is 200 Td and calculations are performed for molecular oxygen.

depends on the magnitude of the drift velocity and shape of the drift velocity temporal profile. As proposed by Bzenić *et al* [23], the time-resolved negative differential conductivity in the temporal profiles of the drift velocity can enhance/reduce the overlap between the drift velocity and electric field. As a consequence, the power absorption by the swarm could be increased/reduced. On the other hand, for an increasing field frequency the phase difference between the drift velocity and electric field is increased due to the inability of both momentum and energy to sufficiently relax before the field changes. As a consequence, the drift velocity undergoes a reduction in the modulation and an increase in the phase shift with respect to the field which in turn leads to reduction of the power absorption. It should be noted that various effective field theories for electron transport in rf electric fields such as quasi-stationary or effective field approximations usually fail to accurately describe the power absorption [11, 23].

3.4. Electrons in a time-varying rf electric field and static magnetic field in the presence of collisions

In this section we analyze the power absorption of the electrons in time-varying rf electric and static magnetic fields in the presence of collisions. Figures 10 and 11 display the variation of the cycle-averaged mean energy and cycle-averaged power as a function of the applied magnetic field strengths for Reid's inelastic ramp model and molecular oxygen, respectively. We observe that the positions of peaks in the $\langle \varepsilon \rangle$ approximately correspond to those of the $\langle p_{\text{abs}} \rangle$. For increasing frequency, the peaks in the B/n_0 -profiles of the $\langle \varepsilon \rangle$ and $\langle p_{\text{abs}} \rangle$ are shifted to the right. For each value of the field frequency, $\langle \varepsilon \rangle$ and $\langle p_{\text{abs}} \rangle$ initially increase with B/n_0 , reaching a peak, and then they start to decrease with B/n_0 . This is a typical resonant behavior although additional peaks observed for collisionless motion in the limit of higher B/n_0 are not observed. However, the position of the central and dominant peak in the B/n_0 -profiles of

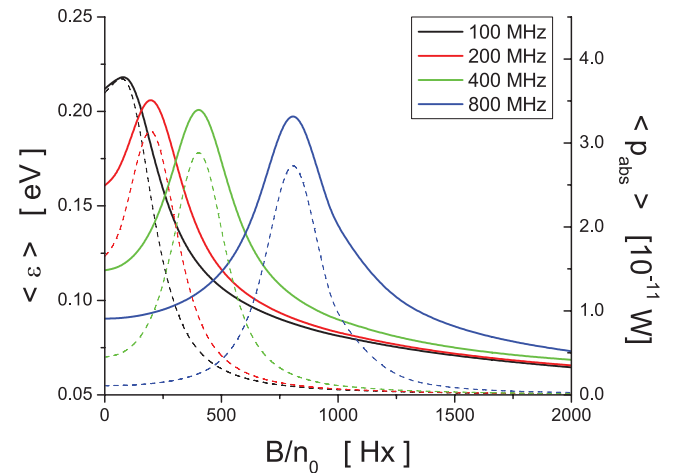


Figure 10. Variation of the cycle-averaged mean energy (full lines) and cycle-averaged absorbed power (dash lines) with B/n_0 for different field frequencies f . Calculations are performed for Reid's inelastic ramp model. The amplitude of electric field is 14.14 Td.

$\langle p_{\text{abs}} \rangle$ for molecular oxygen agree very well with the corresponding peak observed for collisionless motion of a single electron shown in figure 2. This is a clear sign that resonant absorption of the energy for collisionless motion carries over to the situation where collisions control the swarm behavior.

Temporal variations of the longitudinal W_E drift velocity over a range of magnetic fields for electrons in molecular oxygen are shown in figure 12. The electric field amplitude and frequency are set to 200 Td and 500 MHz, respectively. When a dc magnetic field is applied we observe a reduction in modulation amplitude of W_E and the modification of the phase shift between W_E and the electric field. It is interesting to note that for B/n_0 of 750 Hx there is no phase difference between W_E and electric field. However, the maximal absorption of energy occurs for lower B/n_0 , around 550 Hx, as shown in figure 11. This follows from the fact that the modulation amplitude of

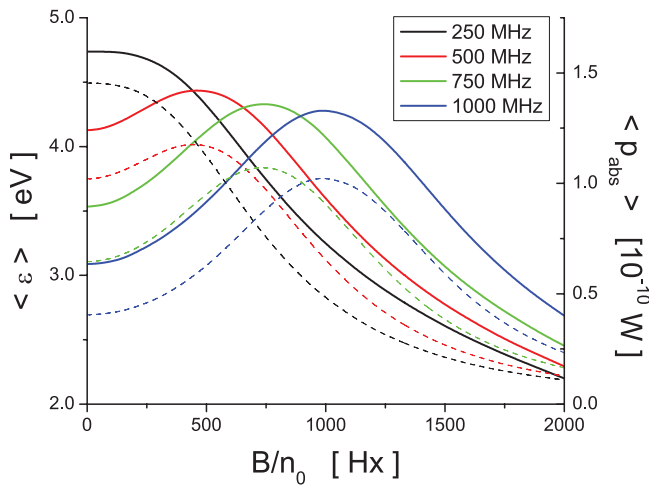


Figure 11. Variation of the cycle-averaged mean energy (full lines) and cycle-averaged power (dash lines) with B/n_0 for different field frequencies f . Calculations are performed for molecular oxygen. The amplitude of electric field is 200 Td.

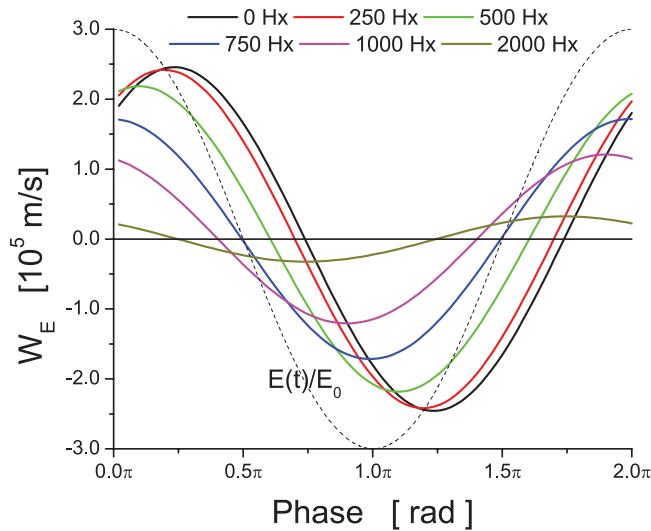


Figure 12. Temporal variations of the longitudinal drift velocity components for a range of magnetic field strengths. Calculations are performed molecular oxygen ($E/n_0 = 200$ Td, $f = 500$ MHz).

W_E is significantly decreased for B/n_0 of 750 Hx and illustrates how the interplay between modulation amplitude of the longitudinal drift velocity and its phase shift with respect to the electric field directly influences the power absorption.

3.5. Electrons in time-varying rf electric and magnetic fields in the presence of collisions

Certainly the most complex situation is the behavior of electrons in rf electric and magnetic fields in the presence of collisions. In figures 13 and 14 we show the variation of the cycle-averaged mean energy and cycle-averaged power as a function of the magnetic field amplitude for Reid's inelastic ramp model and molecular oxygen, respectively. Electric and magnetic fields are in the crossed orientation and $\pi/2$ out of phase. The most prominent property in the B_0/n_0 -profiles of $\langle \varepsilon \rangle$ and $\langle p_{\text{abs}} \rangle$ is the presence of additional periodic

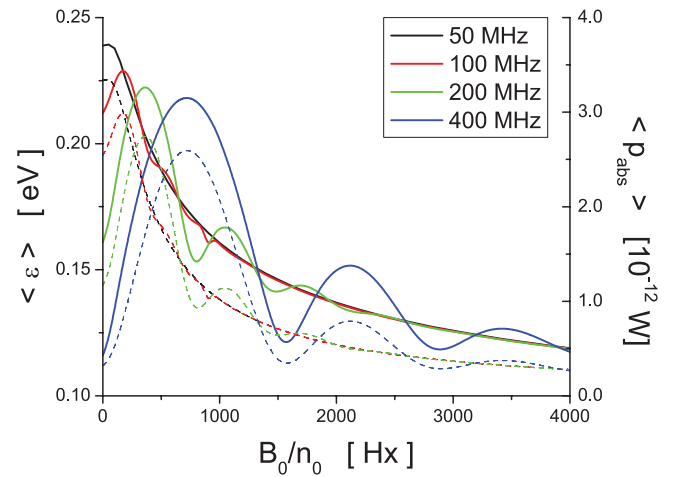


Figure 13. Variation of the cycle-averaged mean energy (full line) and power (dash line) with B_0/n_0 for different field frequencies. Calculations are performed for Reid's inelastic ramp model. The amplitude of electric field is 14.14 Td.

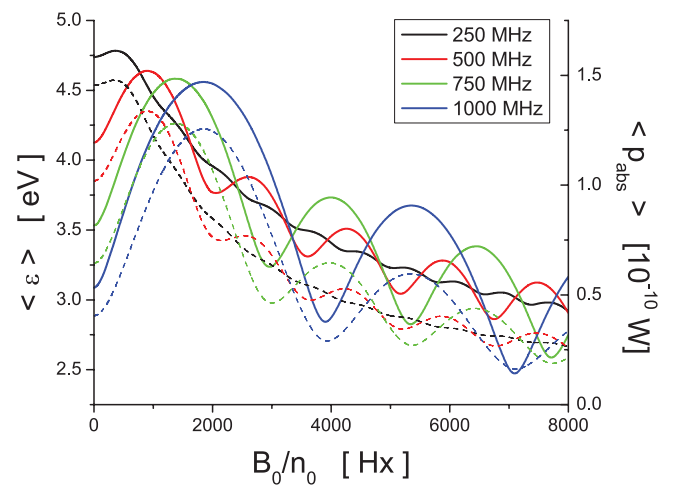


Figure 14. Variation of the cycle-averaged mean energy (full line) and power (dash line) with B_0/n_0 for different field frequencies. Calculations are performed for molecular oxygen. The amplitude of electric field is 200 Td.

structures. The positions of the extremes in $\langle \varepsilon \rangle$ are found to approximately correspond to those of $\langle p_{\text{abs}} \rangle$. For increasing frequency, differences between positions of $\langle \varepsilon \rangle$ and $\langle p_{\text{abs}} \rangle$ are slightly enhanced as the mean energy and drift velocity relax on different time-scales. For Reid's inelastic ramp model and frequencies lower than 50 MHz, $\langle \varepsilon \rangle$ and $\langle p_{\text{abs}} \rangle$ are monotonically decreasing functions of the magnetic field amplitude. For higher frequencies, however, the resonant-type behavior is induced. In contrast to the situation where the electric field is radio-frequency and a magnetic field is static, we observe a multitude of peaks in the B_0/n_0 -profiles of $\langle \varepsilon \rangle$ and $\langle p_{\text{abs}} \rangle$. This is a clear signature of the resonant absorption of energy from the rf electric and magnetic fields. For increasing frequency, the periodic structures become more wider and extremes occur at higher values of B_0/n_0 .

Temporal profiles of the longitudinal drift velocity component as a function of the magnetic field amplitude and

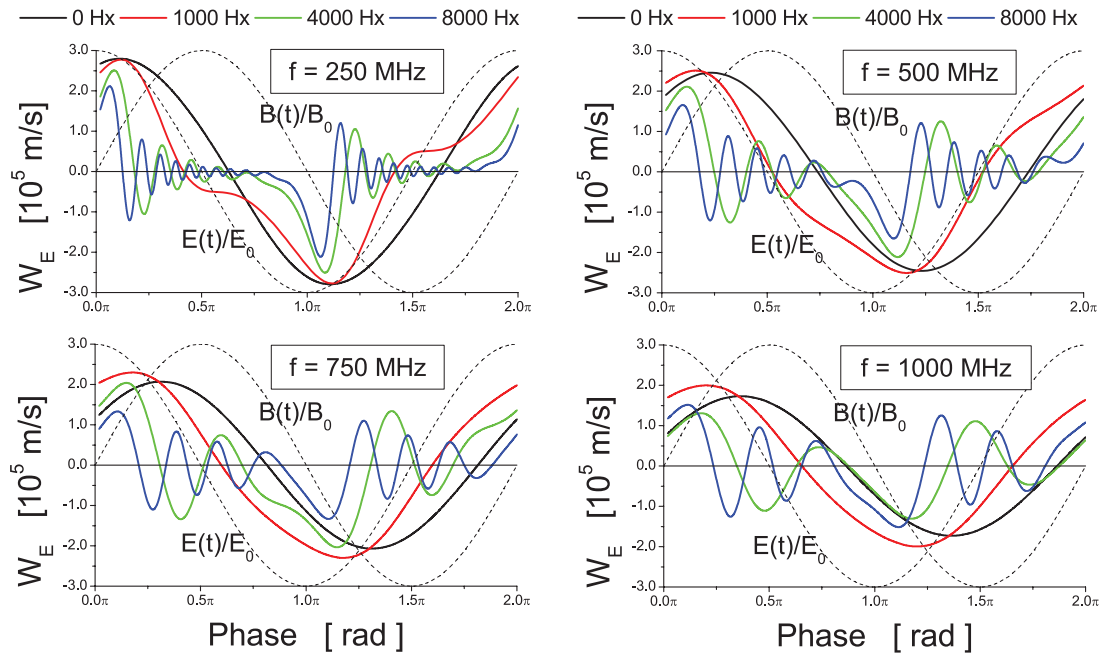


Figure 15. Temporal profiles of the longitudinal drift velocity component as a function of magnetic field amplitude and field frequencies. Calculations are performed for molecular oxygen. The amplitude of electric field is 200 Td.

frequency for electrons in molecular oxygen are shown in figure 15. For increasing B_0/n_0 the additional ‘oscillatory’-type behavior in the W_E profiles is clearly evident for all frequencies considered in this work. For B_0/n_0 of 1000 Hx the modulation amplitude of W_E is increased as compared to the magnetic field free case while the phase shift with respect to the electric field is reduced. This favors the absorption of energy from the fields as shown in figure 14. Further increase of the magnetic field reduces the modulation amplitude and strong oscillations are induced. This is an alternating process which leads to the periodic structures observed in the absorbed power.

4. Discussion

The following question arises from the previous set of results: why do the periodic resonant structures exist for the absorbed power and mean energy in rf electric and magnetic fields? In low-frequency regime when all transport properties have enough time to relax, the physical mechanism of the magnetic cooling in dc electric and magnetic fields [15, 37, 66] is directly carried over to the rf fields. Under these conditions, the absorbed power is a monotonically decreasing function of the applied rf magnetic field amplitude (with the exception of the unusual behavior of mean energy for electrons in pure argon [39]). When the field frequency is increased, however, the phase shift between the drift velocity and electric field is enhanced. The number of electrons traveling against the field is significantly increased and the degree of their ‘synchronization’ with the electric field is reduced. In such a case, if the magnetic field is not too strong, then the action of the magnetic field perpendicular to the electric field (assuming that the electric and magnetic fields are crossed at an arbitrary angle) is to turn those electrons traveling against the electric field to travel with the electric field. In other words, the magnetic field

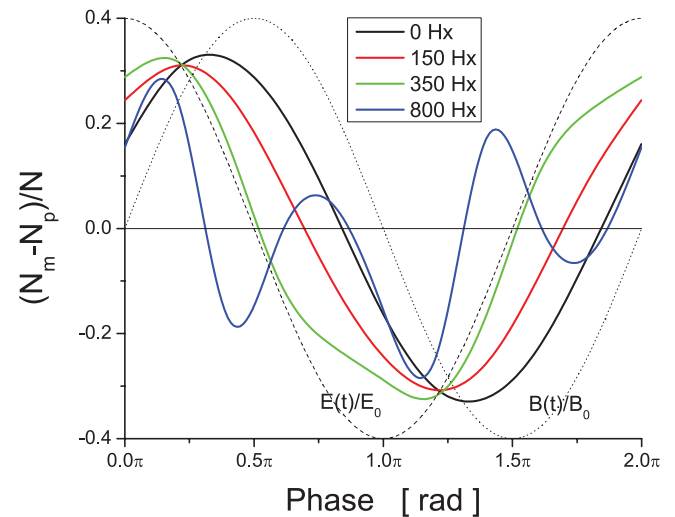


Figure 16. Temporal profiles of the difference between number of electrons traveling along (N_p) and against (N_m) the axis which is defined by the electric field. Calculations are performed for Reid’s inelastic ramp model and N is total number of electrons in simulation. The amplitude and frequency of electric field are 14.14 Td and 200 MHz.

acts in such a manner to ‘synchronize’ electrons with the electric field. This physical picture is valid until reaching the first peak in the absorbed power versus amplitude of the applied rf magnetic field curve (see figures 13 and 14). Further increase of the applied rf magnetic field leads to a decrease of the absorbed power. Some aspects of these physical arguments are illustrated on figure 16 where the temporal profiles of the difference between number of electrons traveling with and against the electric field are calculated for several magnetic field amplitudes. Calculations are performed by our Monte Carlo code for Reid’s inelastic ramp model. The amplitude and frequency are set to 14.14 Td and 200 MHz, respectively.

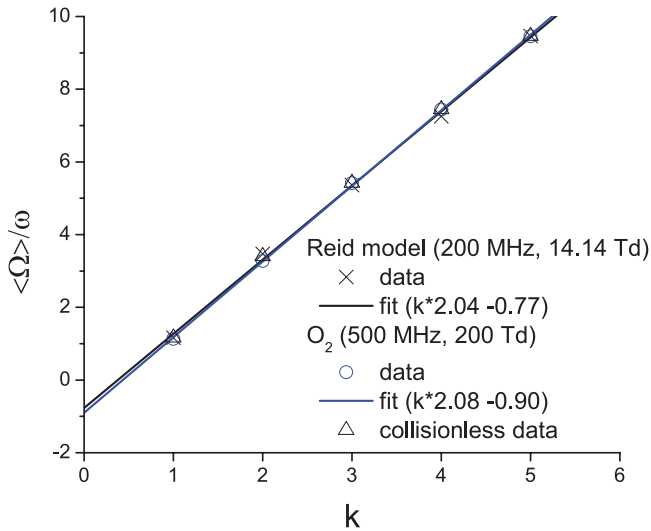


Figure 17. Positions of peaks in the absorbed power versus the ratio of mean cyclotron frequency to driving frequency.

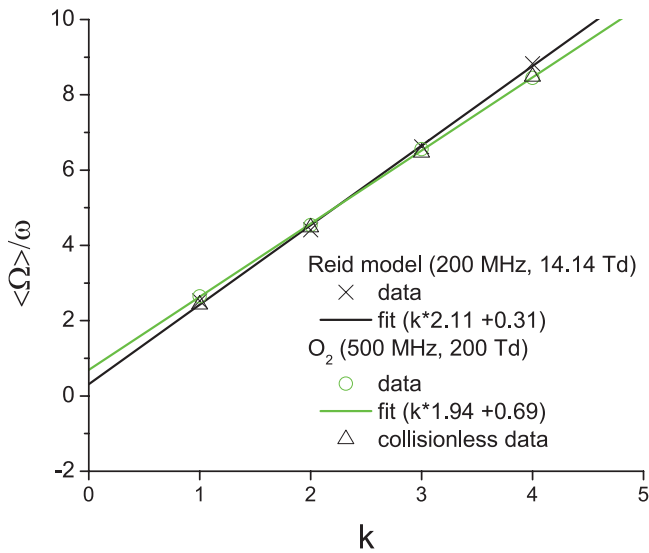


Figure 18. Positions of minima in the absorbed power versus the ratio of mean cyclotron frequency to driving frequency.

We see that the number of electrons traveling along the electric field is much greater for B_0/n_0 of 350 Hx than for the magnetic field free case. The phase shift between their oscillatory motion and oscillating rf electric field is much less comparing to the magnetic field free case and for cases where B_0/n_0 is set to 150 and 800 Hx.

In order to investigate the periodic nature of the resonant structures observed in figures 13 and 14, in figures 17 and 18 we show the positions of extremes in the absorbed power versus the amplitude of the applied rf magnetic field curve. We consider both the collision free case and situation when collisions control the swarm behavior for Reid's inelastic ramp model and molecular oxygen. In addition, we present the results of our linear fitting procedure for both the Reid ramp model and molecular oxygen. The cyclotron frequency is a sinusoidal function and thus we have decided to present its mean value which coincides with the amplitude of cyclotron frequency divided by $\pi/2$. We observe that the spacing between two successive peaks

is constant and is approximately twice the field frequency. In other words, the slope of the fitting curves is approximately 2, as indicating in figures 17 and 18. We have found that the positions of the extremes are exclusively defined by the ratio between the mean cyclotron frequency $\langle \Omega \rangle$ and field frequency ω . As a consequence, the positions of the extremes are not dependent on the nature of the gaseous medium in which electrons drift and diffuse under the influence of rf electric and magnetic fields. Furthermore, we observe that numerical solutions for positions of the extremes in a collision free case agree very well with those obtained by solving Boltzmann's equation when collisions occur. This is a clear sign that even when collisions control the swarm behavior some amount of the energy is transferred to electrons via resonant absorption of the energy from the rf electric and magnetic fields.

5. Conclusion

In this paper we have analyzed, first, the collisionless motion of a single electron in spatially uniform rf electric and magnetic fields. The periodic feature in the absorbed power versus amplitude of the applied rf magnetic field curve has a typical resonant structure. When the power absorption peaks, the longitudinal and transverse velocity components are not periodic, their amplitude continuously increases with time and their mean values are not zero. On the other hand, when the absorbed power is zero, both velocity components are perfectly periodic with constant amplitudes.

Second, using a multi term theory for solving the Boltzmann equation, we have investigated the power absorption of electrons when collisions with neutral molecules occur. Numerical examples are given for electrons moving and diffusing under the action of rf electric and magnetic fields for Reid's inelastic ramp model and molecular oxygen. For magnetic field free case, the absorbed power shows the maximal property with frequency. In domain of rf fields, the absorbed power first increases with frequency, reaching a peak, and then it starts to rapidly decrease in the limit of higher frequencies. When a dc magnetic field is applied, the absorbed power first increases with increasing magnetic field, reaching a peak and then a rapid decrease follows. The maximum absorption of power occurs at magnetic field strengths for which simultaneously the phase shift between the longitudinal drift velocity and electric field is minimal and amplitude of drift velocity component is maximal. The position of the dominant peak on the absorbed power versus magnetic field strength curve coincides with the position of the same peak observed for collisionless motion of a single electron. This is a clear sign that the resonant absorption of energy takes place in both collisionless and collision-dominated regimes for electron swarms in rf electric and dc magnetic fields.

When both electric and magnetic fields are radio-frequency, the periodic structures in the absorbed power versus magnetic field amplitude strength curve are much more complex. We have observed a multitude of peaks in the B_0/n_0 -profiles of the absorbed power and mean energy. Using numerical solutions for collisionless motion of a single electron and multi term

solutions of Boltzmann's equation when collisions occur, we have investigated the synergism of temporal non-locality and resonances and the interplay between these two effects. Perhaps the most striking phenomenon is the independence of the position of the extremes with respect to the gas in which electrons are drifting and diffusing.

In the past most plasma modeling has been carried out on the basis of swarm data for dc fields without any effect of magnetic field. We have tried to show here that the more elaborate representation of swarm transport theory would yield a far richer and more accurate description of heating of electrons in the complex case of combined electric and magnetic fields and their gradients.

There are few possible directions of future work arising from the results presented in this paper. The theory and mathematical machinery briefly presented in this paper, are valid for electric and magnetic fields crossed at arbitrary phases and angles. Therefore, the first logical extension of the current work would be to consider the effects of varying phases and angles between the fields on the power absorption. First steps have already been made towards this direction [34, 67]. Second, the theory and the associated code might be further extended to consider resonances induced by spatial non-locality as considered for electric field only in [54]. The ultimate goal would be to adapt the present theory in a form suitable for practical application to magnetized plasmas. This requires incorporation of the space charge effects through a multi term solution of Boltzmann's equation for both the electron and ion species in the discharge. It would be challenging and instructive to use this plasma-swarm nexus to explore the anomalous skin effect, negative absorption of power and complex electrodynamics of electrons in inductively coupled plasmas.

Acknowledgments

SD, DB and ZLjP acknowledge support from MPNTRRS Projects OI171037 and III41011. RDW is supported by the Australian Research Council.

References

- [1] Petrović Z Lj, Švakov M, Nikitović Ž, Dujko S, Šašić O, Jovanović J, Malović G and Stojanović V 2007 *Plasma Sources Sci. Technol.* **16** S1
- [2] Petrović Z Lj, Dujko S, Marić D, Malović G, Nikitović Ž, Šašić O, Jovanović J, Stojanović V and Radmilović-Radjenović M 2009 *J. Phys. D: Appl. Phys.* **31** 194002
- [3] Shon C H and Lee J K 2002 *Appl. Surf. Sci.* **192** 258
- [4] Shidoji E, Ohtake H, Nakano N and Makabe M 1999 *Japan. J. Appl. Phys.* **38** 2131
- [5] Keidar M, Zhuang T, Shashurin A, Teel G, Chiu D, Lukas J, Haque S and Brieda L 2015 *Plasma Phys. Control. Fusion* **57** 014005
- [6] Ahedo E 2011 *Plasma Phys. Control. Fusion* **53** 124037
- [7] Makabe T and Petrović Z Lj 2015 *Plasma Electronics* 2nd edn (New York: CRC)
- [8] Lieberman M A and Lichtenberg A J 2005 *Principles of Plasma Discharges and Materials Processing* 2nd edn (New York: Wiley)
- [9] Blum W and Rolandi L 1993 *Particle Detection with Drift Chambers* (Berlin: Springer)
- [10] Bošnjaković D, Petrović Z Lj, White R D and Dujko S 2014 *J. Phys. D: Appl. Phys.* **47** 435203
- [11] Petrović Z Lj, Raspopović Z M, Dujko S and Makabe T 2002 *Appl. Surf. Sci.* **192** 1
- [12] White R D, Ness K F, Robson R E and Li B 1999 *Phys. Rev. E* **60** 2231
- [13] White R D, Ness K F and Robson R E 2002 *Appl. Surf. Sci.* **192** 26
- [14] Dujko S, Raspopović Z M and Petrović Z Lj 2005 *J. Phys. D: Appl. Phys.* **38** 2952
- [15] Dujko S, White R D, Ness K F, Petrović Z Lj and Robson R E 2006 *J. Phys. D: Appl. Phys.* **39** 4788
- [16] Sankaran A and Kushner M J 2002 *J. Appl. Phys.* **92** 736
- [17] Dujko S, White R D, Petrović Z Lj and Robson R E 2011 *Plasma Sources Sci. Technol.* **20** 024013
- [18] Loffhagen D and Winkler R 1999 *IEEE Trans. Plasma Sci.* **27** 1262
- [19] Winkler R, Maiorov V A and Sigenefer F 2000 *J. Appl. Phys.* **87** 2708
- [20] Winkler R, Loffhagen D and Sigenefer F 2002 *Appl. Surf. Sci.* **192** 50
- [21] White R D, Robson R E and Ness K F 1995 *Aust. J. Phys.* **48** 925
- [22] Maeda K, Makabe T, Nakano N, Bzenić S and Petrović Z Lj 1997 *Phys. Rev. E* **55** 5901
- [23] Bzenić S, Petrović Z Lj, Raspopović Z M and Makabe T 1999 *Japan. J. Appl. Phys.* **38** 6077
- [24] Raspopović Z, Sakadžić S, Petrović Z Lj and Makabe T 2000 *J. Phys. D: Appl. Phys.* **33** 1298
- [25] White R D, Dujko S, Ness K F, Robson R E, Raspopović Z and Petrović Z Lj 2008 *J. Phys. D: Appl. Phys.* **41** 025206
- [26] Dujko S, Raspopović Z M, Petrović Z Lj and Makabe T 2003 *IEEE Trans. Plasma Sci.* **31** 711
- [27] Kolev St, Hagelaar G J, Fubiani G and Boeuf J-P 2012 *Plasma Sources Sci. Technol.* **21** 025002
- [28] Zhao Y J, Liu H, Yu D R, Hu P and Wu H 2014 *J. Phys. D: Appl. Phys.* **47** 045201
- [29] Benyoucef D and Yousfi M 2014 *Plasma Sources Sci. Technol.* **23** 044007
- [30] Kinder R L and Kushner M J 2001 *J. Appl. Phys.* **90** 3699
- [31] Tadokoro M, Hirata H, Nakano N, Petrović Z Lj and Makabe T 1998 *Phys. Rev. E* **57** R43
- [32] Vasenkov A V and Kushner M J 2003 *J. Appl. Phys.* **94** 5522
- [33] White R D, Robson R E, Dujko S, Nicoletopoulos P and Li B 2009 *J. Phys. D: Appl. Phys.* **42** 194001
- [34] Dujko S 2009 *PhD Thesis* James Cook University, Australia
- [35] Dujko S and White R D 2008 *J. Phys. Conf. Ser.* **133** 012005
- [36] Dujko S, White R D, Petrović Z Lj and Robson R E 2010 *Phys. Rev. E* **81** 046403
- [37] Ness K F 1994 *J. Phys. D: Appl. Phys.* **27** 1848
- [38] Raspopović Z M, Sakažić S, Bzenić S and Petrović Z Lj 1999 *IEEE Trans. Plasma Sci.* **27** 1241
- [39] Ness K F and Makabe T 2000 *Phys. Rev. E* **62** 4083
- [40] Vahedi V, Lieberman M A, DiPeso G, Rognlien T D and Hewett D 1995 *J. Appl. Phys.* **78** 1446
- [41] Tuszewski M 1996 *Phys. Plasma* **4** 1922
- [42] Kolobov V I and Economou D J 1997 *Plasma Sources Sci. Technol.* **6** R1
- [43] Haas F A 2001 *Plasma Sources Sci. Technol.* **10** 440
- [44] Lee H-C, Oh S J and Chin-Wook Chung C-W 2012 *Plasma Sources Sci. Technol.* **21** 035003
- [45] Kushner M J, Collision W Z, Grapperhaus M J, Holland J P and Barnes M S 1996 *J. Appl. Phys.* **80** 1337
- [46] Lloyd S, Shaw D M, Watanabe M and Collins G J 1999 *Japan. J. Appl. Phys.* **38** 4275

- [47] Hollenstein Ch, Guittienne Ph and Howling A A 2013 *Plasma Sources Sci. Technol.* **22** 055021
- [48] Scheubert P, Fantz U, Awakowicz P and Paulin H 2001 *J. Appl. Phys.* **90** 587
- [49] Hash D B, Bose D, Rao M V V S, Cruden B A, Meyyappan M and Sharma S P 2001 *J. Appl. Phys.* **90** 2148
- [50] Godyak V A, Piejak R B and Alexandrovich B M 1999 *J. Appl. Phys.* **85** 3081
- [51] Cunge G, Crowley B, Vender D and Turner M M 2001 *J. Appl. Phys.* **89** 3580
- [52] Vasenkov V A and Kushner M J 2002 *Phys. Rev. E* **66** 066411
- [53] Minea T M and Bretagne J 2003 *Plasma Sources Sci. Technol.* **12** 97
- [54] Nicoletopoulos P, Robson R E and White R D 2012 *Phys. Rev. E* **85** 046404
- [55] Dormand J R and Prince P J 1980 *J. Comput. Appl. Math.* **6** 19
- [56] Dujko S, White R D and Petrović Z Lj 2008 *J. Phys. D: Appl. Phys.* **41** 245205
- [57] Dujko S, White R D, Raspopović and Petrović Z Lj 2012 *Nucl. Instrum. Methods Phys. Res. B* **279** 84
- [58] Ness K F and Robson R E 1986 *Phys. Rev. A* **34** 2185
- [59] Reid I 1979 *Aust. J. Phys.* **32** 231
- [60] White R D, Brennan M J and Ness K F 1997 *J. Phys. D: Appl. Phys.* **30** 810
- [61] White R D, Dujko S, Robson R E, Petrović Z Lj and McEachran R P 2010 *Plasma Sources Sci. Technol.* **19** 034001
- [62] Itikawa Y, Ichimura A, Onda K, Sakimoto K, Takayanagi K, Hatano Y, Hayashi M, Nishimura H and Tsurubuchi S 1989 *J. Phys. Chem. Ref. Data* **18** 23
- [63] Itikawa Y 2009 *J. Phys. Chem. Ref. Data* **38** 1
- [64] White R D, Robson R E, Ness K F and Makabe T 2005 *J. Phys. D: Appl. Phys.* **38** 997
- [65] Dujko S, White R D, Petrović Z Lj and Ebert U 2011 *Japan. J. Appl. Phys.* **50** 08JC01
- [66] White R D, Ness K F and Robson R E 1999 *J. Phys. D: Appl. Phys.* **32** 1842
- [67] Dujko S, Bošnjaković D, White R D and Petrović Z Lj 2015 in preparation

Boltzmann equation and Monte Carlo studies of electron transport in resistive plate chambers

D Bošnjaković^{1,2}, Z Lj Petrović^{1,2}, R D White³ and S Dujko¹

¹ Institute of Physics, University of Belgrade, Pregrevica 118, 11070 Belgrade, Serbia

² Faculty of Electrical Engineering, University of Belgrade, Bulevar kralja Aleksandra 73, 11120 Belgrade, Serbia

³ ARC Centre for Antimatter-Matter Studies, School of Engineering and Physical Sciences, James Cook University, 4811 Townsville, Australia

E-mail: dbosnjak@ipb.ac.rs

Received 18 June 2014, revised 25 August 2014

Accepted for publication 3 September 2014

Published 3 October 2014

Abstract

A multi term theory for solving the Boltzmann equation and Monte Carlo simulation technique are used to investigate electron transport in Resistive Plate Chambers (RPCs) that are used for timing and triggering purposes in many high energy physics experiments at CERN and elsewhere. Using cross sections for electron scattering in $C_2H_2F_4$, iso- C_4H_{10} and SF_6 as an input in our Boltzmann and Monte Carlo codes, we have calculated data for electron transport as a function of reduced electric field E/N in various $C_2H_2F_4$ /iso- C_4H_{10} / SF_6 gas mixtures used in RPCs in the ALICE, CMS and ATLAS experiments. Emphasis is placed upon the explicit and implicit effects of non-conservative collisions (e.g. electron attachment and/or ionization) on the drift and diffusion. Among many interesting and atypical phenomena induced by the explicit effects of non-conservative collisions, we note the existence of negative differential conductivity (NDC) in the bulk drift velocity component with no indication of any NDC for the flux component in the ALICE timing RPC system. We systematically study the origin and mechanisms for such phenomena as well as the possible physical implications which arise from their explicit inclusion into models of RPCs. Spatially-resolved electron transport properties are calculated using a Monte Carlo simulation technique in order to understand these phenomena.

Keywords: resistive plate chambers, Boltzmann equation, Monte Carlo simulation, electron transport coefficients, negative differential conductivity

(Some figures may appear in colour only in the online journal)

1. Introduction

Resistive Plate Chambers (RPCs) are widely used particle detectors due to their simple construction, good detection efficiency, good spatial resolution and excellent timing resolution [1–6]. They are mainly utilized in large high-energy physics experiments for timing and triggering purposes [7–9] but they found their way into applications in other fields, including medical imaging [10, 11] and geophysics [12].

Depending on the applied electric field strength, geometry and gas mixture, RPCs can be operated in avalanche or

streamer mode. The avalanche mode of operation provides a much better rate capability than streamer mode, but at the expense of smaller signals [5]. Typical gas mixtures used in the avalanche mode of operation are composed of tetrafluoroethane ($C_2H_2F_4$), iso-butane (iso- C_4H_{10}) and sulfur hexafluoride (SF_6). Tetrafluoroethane is a weakly electronegative gas with a high primary ionization. Iso-butane is a UV-quencher gas while sulfur hexafluoride is a strongly electronegative gas, used in avalanche mode to suppress the development of streamers. Recently, Abbrescia *et al* [13] have proposed new gaseous mixtures for RPCs that operate in

avalanche mode to overcome some of the problems encountered with standard gas mixtures based on tetrafluoroethane, iso-butane and sulfur hexafluoride.

There have been numerous models and simulations of RPCs. Being analytical [14, 15], Monte Carlo [3] or based on fluid equations [16–18], all macroscopic models rely on accurate data for electron swarm transport in gases. These quantities can be either measured in swarm experiments or calculated from electron impact cross sections by the Boltzmann equation analysis or by a Monte Carlo technique [19, 20]. In particle detector community, MAGBOLTZ [21] is the most commonly used Monte Carlo code for such a task. It has been routinely used many times in the past to evaluate electron transport data under the hydrodynamic conditions, and for different experimental arrangements including the Pulsed Townsend (PT) and steady-state Townsend conditions (SST). The motivation for this work lies with the fact that there are some important aspects of electron transport which cannot be analyzed by means of a Monte Carlo method used in MAGBOLTZ. One of these aspects includes the explicit and implicit effects of non-conservative collisions on electron transport and implications which arise from their inclusion in models of RPCs. Collisions in which the number of electrons changes either being produced or removed from the initial ensemble are regarded as non-conservative collisions. Typical examples of these collisions are ionization, attachment, as well as electron-induced detachment from negative ions and electron-ion recombination. These processes may have a marked influence on the electron transport properties and the detector performance. As an illustrative example, Doroud *et al* [22] have shown that the recombination dramatically reduces the amount of charge in the gas filled gap which in turn affects the rate capability in the multi gap RPC used for timing purposes in the ALICE experiment at CERN. In particular, kinetic phenomena induced by the explicit effects of ionization and/or electron attachment should be studied in terms of flux and bulk components of transport coefficients [19, 20, 23]. The distinction between these two sets of transport data has been systematically ignored in the particle detector community and reason for this might be the fact that MAGBOLTZ cannot be used to compute the bulk transport coefficients. At the same time the most accurate experiments used to unfold the cross section data measure bulk coefficients. However, the duality in transport coefficients is easy to understand physically. In this paper we present the required theoretical treatment of the non-conservative corrections, and highlight differences in origin and magnitudes of the bulk and flux transport coefficients for electrons in the gas mixtures used in RPCs in various high energy physics (HEP) experiments at CERN.

Recently, it was shown that the addition of SF₆ (and iso-C₄H₁₀) to standard RPC mixtures may improve several important aspects of the RPC performance in avalanche mode, including efficiency and time resolution [24]. It has been long established that electron attachment to SF₆ leads to the formation of both parent (SF₆⁻) and fragment (SF₅⁻, SF₄⁻, SF₃⁻, SF₂⁻, F₂⁻ and F⁻) negative ions [25]. In particular, the cross section for the creation of stable parent negative ions SF₆⁻ at zero energy is huge suggesting that the lower energy electrons are

most likely to be consumed before their recombination with the positive ions. This in turn may induce some attachment induced kinetic phenomena in electron transport due to the strong electronegative nature of SF₆. One of the most striking phenomena induced by strong electron attachment in the mixtures of rare gases and fluorine is the negative absolute electron mobility [26, 27]. Occurrence of these phenomena should be carefully considered in numerical simulations in accordance with the experimental evaluation of the RPC performance.

Here we do not attempt to consider primary ionization effects, space charge effects and signal induction in the presence of resistive material nor do we attempt to compute the RPC performances, i.e. efficiency, time resolution and charge spectra. These important elements of modeling are the subject of our future publications [28]. Instead we isolate and investigate electron swarms under the action of a spatially uniform electric field. In the present work we solve the Boltzmann equation for electrons undergoing non-conservative collisions in the gas mixtures of C₂H₂F₄, iso-C₄H₁₀ and SF₆ used in RPCs in various HEP experiments at CERN. In this application electron attachment and ionization play a key role in the electron behavior, therefore any modeling must treat them in a comprehensive manner. Variation and general trends of the mean energy and effective ionization coefficient, drift velocity and diffusion tensor with the applied reduced electric field are presented. We use our Monte Carlo simulation technique as a complementary method to Boltzmann's equation with the specific purpose to evaluate the spatially resolved transport data and distribution functions amidst non-conservative collisions. The knowledge of spatially resolved transport data is very useful in modeling of RPCs and understanding their performance. Fluid models of RPCs can be further improved by considering the non-local effects induced by a large spatial variation in the electric field during the avalanche-streamer transition or due to presence of physical boundaries. Correct implementation of transport data and accuracy of their calculation is also highlighted in the present work. Our methodology based on complementary Boltzmann and Monte Carlo studies of electron transport in neutral gases has already been used in different gas discharge problems [29]. This is the first paper to our knowledge where the combined Boltzmann equation analysis and Monte Carlo simulation technique are applied to the description of electron kinetics in the gas mixtures used in RPCs.

This paper is organized as follows. In section 2 we substantiate the existence of hydrodynamic regime and identify the differences in the bulk and flux transport coefficients. In section 2.1 we give a brief discussion of the theoretical multi term solution of the Boltzmann equation under non-conservative conditions. The basic elements of our Monte Carlo simulation code are discussed in section 2.2. In section 3, we present the results of a systematic study of electron transport in the gas mixtures used in RPCs that are used for timing and triggering purposes in many high energy experiments at CERN. We focus on the way in which the transport coefficients are influenced by non-conservative collisions, particularly by electron attachment. Spatially resolved energy and rate coefficients as well as spatial profiles of the electrons are calculated

by a Monte Carlo simulation technique with the aim of understanding the NDC and related phenomena. This paper represents the first comprehensive treatment of non-conservative electron transport in typical RPC gas mixtures based on a rigorous Boltzmann equation analysis and the Monte Carlo simulation technique.

2. Theoretical methods

Electron transport in non-conservative RPC gases should be analyzed in terms of bulk (e.g. reactive) and flux components. The main motivation for such analysis is to gain insight into the effect of non-conservative processes on electron transport as these processes influence many operating characteristics of the detector. For example, there is a direct link between the effective ionization coefficient and time resolution of an RPC. Spatial resolution, on the other hand, is greatly affected by transverse diffusion while the role of attachment processes is twofold. On one hand, electron attachment is a desirable process as it controls the avalanche multiplication and limits the amount of charge between the electrodes, which in turns improves the rate capability of an RPC. On the other hand, if the attachment is too strong with a large exponential decay rate for electrons then the time resolution and efficiency might be seriously affected. It is clear that care must be taken when non-conservative collisions are operative to ensure the optimal performance of the detector.

2.1. A brief sketch of the Boltzmann equation analysis

All information on the drift and diffusion of electrons in gases is contained in the electron phase-space distribution function $f(\mathbf{c}, \mathbf{r}, t)$, where \mathbf{r} represents the spatial coordinate of an electron at time t , and \mathbf{c} denotes its velocity. The distribution function $f(\mathbf{r}, \mathbf{c}, t)$ is evaluated by solving Boltzmann's equation:

$$\left(\partial_t + \mathbf{c} \cdot \nabla_{\mathbf{r}} + \frac{e}{m} \mathbf{E} \cdot \nabla_{\mathbf{c}} \right) f(\mathbf{r}, \mathbf{c}, t) = -J(f, f_0), \quad (1)$$

where ∂_t , $\nabla_{\mathbf{r}}$ and $\nabla_{\mathbf{c}}$ are the gradients with respect to time, space and velocity, while e and m are the charge and mass of the electron and \mathbf{E} is the magnitude of the electric field. The right-hand side of (1) $J(f, f_0)$ denotes the linear electron-neutral molecule collision operator, accounting for elastic, inelastic and non-conservative (e.g. electron attachment and/or ionization) collisions, and f_0 is the velocity distribution function of the neutral gas (usually taken to be Maxwellian at fixed temperature). For elastic collisions we use the original Boltzmann collision operator [30], while for inelastic collisions we prefer the semiclassical generalization of Wang-Chang *et al* [31]. The collision operators for non-conservative collisions are discussed in [32, 33]. We assume that in the division of post-collision energy between the scattered and ejected electrons in an ionization process, all fractions are equally probable.

Solution of Boltzmann's equation (1) has been extensively discussed in our recent reviews [20, 34]. In brief, f is expanded in terms of normalized Burnett functions about a Maxwellian at an arbitrary temperature T_b . In the hydrodynamic regime, its

space-time dependence is expressed by an expansion in terms of the gradient of the electron number density $n(\mathbf{r}, t)$. This assumption is generally valid for an RPC detector even in the regions where high energy particle creates the clusters of electrons with steep density gradients. One may expect that diffusion processes will act to validate the assumption on weak gradients after a certain period of time. Thus, the following expansion of the phase-space distribution function follows:

$$f(\mathbf{r}, \mathbf{c}, t) = \tilde{\omega}(\alpha, c) \sum_{\nu=0}^{\infty} \sum_{l=0}^{\infty} \sum_{m=-l}^l \sum_{s=0}^{\infty} \sum_{\lambda=0}^s F(\nu lm|s\lambda; \alpha) \phi_m^{[\nu l]} G_m^{(s\lambda)} n(\mathbf{r}, t), \quad (2)$$

where

$$\tilde{\omega}(\alpha, c) = \left(\frac{\alpha^2}{2\pi} \right)^{3/2} \exp\left(-\frac{\alpha^2 c^2}{2} \right), \quad (3)$$

is a Maxwellian distribution function at a temperature T_b , with $\alpha^2 = \frac{m}{kT_b}$. T_b is not equal to the neutral gas temperature and serves as a free and flexible parameter to optimize the convergence. The quantities $\phi_m^{[\nu l]}$ and $G_m^{(s\lambda)}$ are normalized Burnett functions and irreducible gradient tensor operator, respectively, and are defined in [32, 33]. The coefficients $F(\nu lm|s\lambda; \alpha)$ are called 'moments' and are related to the electron transport properties as detailed below. The bulk drift velocity (W), bulk diffusion coefficients (D_L , D_T) and effective ionization coefficient ($k_{\text{eff ion}}$) are defined in terms of the diffusion equation and can expressed in terms of moments as follows [20, 34]:

$$W = \frac{i}{\alpha} F(010|00) - in_0 \sum_{\nu'=1}^{\infty} J_{0\nu'}^0(\alpha) F(\nu'00|11), \quad (4)$$

$$D_L = -\frac{1}{\alpha} F(010|11) - n_0 \left(\sum_{\nu'=1}^{\infty} J_{0\nu'}^0(\alpha) F(\nu'00|20) - \sqrt{2} F(\nu'00|20) \right), \quad (5)$$

$$D_T = -\frac{1}{\alpha} F(011|11) - n_0 \left(\sum_{\nu'=1}^{\infty} J_{0\nu'}^0(\alpha) F(\nu'00|20) + \frac{1}{\sqrt{2}} F(\nu'00|22) \right), \quad (6)$$

$$k_{\text{eff ion}} = in_0 \sum_{\nu'=1}^{\infty} J_{0\nu'}^0(\alpha) F(\nu'00|00), \quad (7)$$

where $J_{0\nu'}^0(\alpha)$ are reduced matrix elements of the collision operator. The bulk transport coefficients are the sum of the flux transport coefficients (defined in terms of Fick's law and given the first terms in each of the expressions (4)–(6)) and a contribution due to non-conservative collisions (the terms involving the summations in each expression). Differences between the two sets of coefficients thus arise when non-conservative processes are operative. The reader is referred to

[19, 20, 23, 34] for full details. Also of interest is the spatially homogeneous mean energy

$$\varepsilon = \frac{3}{2}kT_b \left(1 - \sqrt{\frac{2}{3}} F(100|00) \right). \quad (8)$$

Using the above decomposition of f (2), the Boltzmann equation (1) is converted to a hierarchy of doubly infinite set of coupled algebraic equations for the moments. To obtain electron transport coefficients identified in (4)–(6) under conditions when the transport is greatly affected by non-conservative collisions, the index s in (2) must span the range (0–2) (e.g. second-order density gradient expansion). Solution of the system of equations can be found by truncation of the infinite summations in the velocity space representation in (2) at l_{\max} and ν_{\max} , respectively. The values of these indices required to achieve the designated convergence criterion, represent respectively the deviation of the velocity distribution from isotropy in velocity space, and the deviation from a Maxwellian speed distribution at the basis temperature T_b . The classical two term approximation sets $l_{\max} = 1$, which is not sufficient for molecular gases used in an RPC due to the anisotropy of f in velocity space. A value of $l_{\max} = 5$ was required for achieving an accuracy to within 1%. Depending of the basis temperature, values of $\nu_{\max} = 95$ were sometimes required under conditions when the distribution function was strongly non-equilibrium and far away from a Maxwellian. The resulting coefficient matrix is sparse and direct numerical inversion procedure is used to calculate the moments.

One should be aware of the differences in the definition of both sets of transport data, bulk and flux, and make sure that proper data are employed in the models. MAGBOLTZ is routinely used in particle detector community for determination of electron transport properties and few comments about this code are appropriate here. MAGBOLTZ cannot compute the bulk transport coefficients and it is exactly these data that are required for some aspects of modeling. For example, in the application of Legler’s model for the avalanche size distribution as a function of the distance [2, 35], one should use the bulk drift velocity to evaluate the ionization coefficient. In addition, the bulk data should be generally used to unfold cross sections from experimentally measured and theoretically calculated transport coefficients [19, 20]. On the other, in fluid modeling of RPCs [16–18] the flux data should be generally used as an input although in some combined fluid/Monte Carlo models the bulk data are required. Generally speaking, the distinction between the bulk and flux data has been systematically ignored in the particle detector community and one of the principal aims of this work is to sound a warning to those who implement the swarm data to be aware of the origin of the transport data and the type of transport data required in their modeling. In this paper we illustrate that bulk and flux data may exhibit not only quantitative but also the qualitative differences in the mixtures of $C_2H_2F_4$, iso- C_4H_{10} and SF_6 used in RPCs operated in avalanche mode.

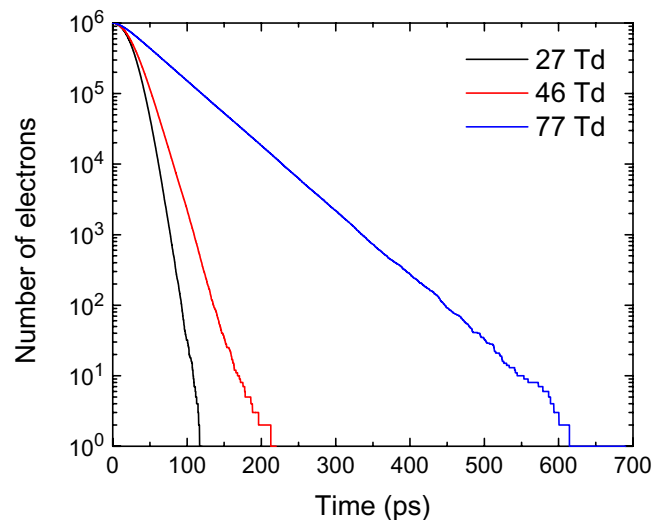


Figure 1. Exponential decay of the number of electrons for three different reduced electric fields as indicated on the graph. Calculations are performed for electrons in ALICE TOF RPC system.

2.2. A brief overview of our Monte Carlo simulation technique

Rather than present a full review of our Monte Carlo simulation technique, we highlight below some of its aspects associated with the sampling of spatially resolved electron transport data. In this work we apply the code primarily to calculate spatially resolved transport data with an aim of using these data to understand the sometimes atypical manifestations of the drift and diffusion in the RPCs. In order to sample spatially resolved transport parameters under hydrodynamic conditions, we have restricted the space to realistic dimensions of the RPC and divided it into cells. Every cell contains 100 sub-cells and these sub-cells are used to sample spatial parameters of electron swarm. This concept allowed us to follow the development of the swarm in both real space and normalized to 6σ , where σ is the standard deviation of the Gaussian distribution in space. The space (and time) resolved electron transport properties including the average energy/velocity and rate coefficients and also density profiles have been determined by counting the electrons and their energies/velocities as well as number of collisions in every cell.

When electron transport is greatly affected by non-conservative collisions, it is of key importance for a tractable simulation to efficiently control the number of electrons in simulations without distortion of the spatial gradients of the distribution function. It is well known that the statistical uncertainty of a Monte Carlo simulation decreases inversely with the square root of the number of electrons processed. In particular, when attachment occurs, electrons are lost continually, so that the number of electrons in the swarm decreases exponentially with time. This is illustrated in figure 1 for electrons in the gas mixture used in ALICE timing RPC.

The initial number of electrons is set to 1×10^6 and calculations are performed for a range of reduced electric fields E/N as indicated on the graph. We see that as E/N decreases the number of electrons decreases markedly. This is a consequence of an increasing collision frequency for electron attachment when E/N is reduced. In order to compensate

the electrons that are consumed by a strong attachment at low electron energy, the following rescaling procedure was adopted. First, the sampling time used for determination of various swarm dynamic properties (for example the mean position, velocity and energy of the electrons) was reduced and adjusted depending on the applied reduced electric field. Second, whenever electron is lost due to attachment another electron is randomly selected in its place from the ensemble of the remaining electrons. This was necessary in order to prevent large and continuous losses of electrons. This procedure was validated for a range of model and real gases when attachment is dominant non-conservative process and found to be correct [36, 37]. Other rescaling procedures to electron swarms with large exponential decay rates are available. The classical example is the procedure developed by Li *et al* [38]. The essence of their rescaling procedure is the addition of an artificial ionization channel with an energy-independent ionization frequency, chosen to be roughly equal to an attachment collision frequency for a given E/N . Similar procedure was applied to simulate electron transport in pure SF₆ by Yousfi *et al* [39]. Finally, we note that when ionization takes place the rescaling procedure was not necessary under conditions considered in this work, as ionization was not a sufficiently intensive process to increase the number of electrons beyond the limits set by the allocated memory.

3. Results and discussion

3.1. Preliminaries

As discussed in section 1, one of the aims of this work is to consider electron transport parameters as input in fluid and kinetic models of RPCs. The operating values of E/N for RPCs are above the critical electric fields for the corresponding gas mixtures, usually between 400 Td and 450 Td for timing RPC depending on the type of experiment and around 200 Td for triggering RPC. Fluid models of these detectors in both avalanche and streamer modes, however, require tabulation of transport data over a wide range of the reduced electric fields and/or mean energy of the electrons depending on the order of fluid approach [40, 41]. In this work we consider the reduced electric field range: 1–1000 Td ($1\text{Td} = 1 \times 10^{-21} \text{Vm}^2$) while the pressure and temperature of the background gas are 1 atm and 293 K, respectively.

The cross sections for electron scattering from C₂H₂F₄ detailed in Šašić *et al* [42] are used in this study. The cross sections for electron scattering in iso-C₄H₁₀ are taken from MAGBOLTZ code developed by Biagi. Finally, the cross sections for electron scattering in SF₆ are taken from Itoh *et al* [43]. Other sets of cross sections for electron scattering in these gases are available in the literature but our Boltzmann equation analysis has revealed that the present sets provide values of swarm parameters such as ionization and electron attachment rate coefficients, drift velocity, longitudinal and transverse diffusion coefficient in a good agreement with the experimental measurements for a wide range of E/N [44, 45]. The following mixtures are used for different RPCs considered in this work: (1) ALICE timing

RPC C₂H₂F₄/iso-C₄H₁₀/SF₆ = 90/5/5 [8]; (2) ALICE triggering RPC C₂H₂F₄/iso-C₄H₁₀/SF₆ = 89.7/10/0.3 [8]; (3) CMS triggering RPC C₂H₂F₄/iso-C₄H₁₀/SF₆ = 96.2/3.5/0.3 [9]; and (4) ATLAS triggering RPC C₂H₂F₄/iso-C₄H₁₀/SF₆ = 94.7/5/0.3 [7].

3.2. Effects of non-conservative collisions

In the following sections we often find it necessary to refer to the explicit influence of electron attachment and/or ionization on electron transport to explain certain phenomena. The following elementary considerations apply. Even under the hydrodynamic conditions (far away from the boundaries, sources and sinks of electrons) the distribution of the average energy within the swarm is spatially anisotropic. This is illustrated in section 3.3 where spatially resolved average energy for electrons in ALICE timing RPC is shown as a function of E/N . Electrons at the front of the swarm generally have higher energy than those at the trailing edge, as on the average they have been accelerated through a larger potential. Since electron attachment and ionization are energy dependent, they will also occur with a spatial dependence. For example, if the collision frequency for electron attachment increases with energy, attachment will predominantly occur at the front of the swarm, resulting in a backwards shift of the swarm's centre of mass, which is observable as a reduction of the bulk drift velocity as compared with the flux drift velocity. The loss of high energy electrons also lowers the mean energy which in turns reduces the flux component of the diffusion. This process is known as *attachment cooling* [33].

If the collision frequency for electron attachment decreases with energy, then the opposite situation holds: the lower energy electrons at the trailing edge of the swarms will be consumed resulting in a forward shift of the swarm's centre of mass, which is observable as an increase of the bulk drift velocity. The mean energy is raised as the lower energy electrons are consumed resulting in an enhancement of the flux components of transverse and longitudinal diffusion. This phenomenon is known as *attachment heating* [32] and is particularly important for electron transport in the gas mixtures used in RPCs. Finally, when ionization takes place, electrons are preferentially created in regions of higher energy resulting in a shift in the centre of mass position as well as a modification of the spread about the centre of mass. This will be observable as an increase of the bulk drift velocity and the bulk diffusion coefficients. This situation also plays an important role in consideration of electron kinetics in RPCs analyzed in this work.

3.3. Boltzmann equation results for electron transport coefficients

In figure 2 we show the variation of mean energy with E/N for RPCs used in ALICE, CMS and ATLAS experiments at CERN.

The properties of the cross sections are reflected in the profiles of the mean energy and we observe three distinct regions of transport. Excepting ALICE timing RPC, in the remaining experiments we first observe a region of slow rise due to (relatively) large energy losses associated with vibrational

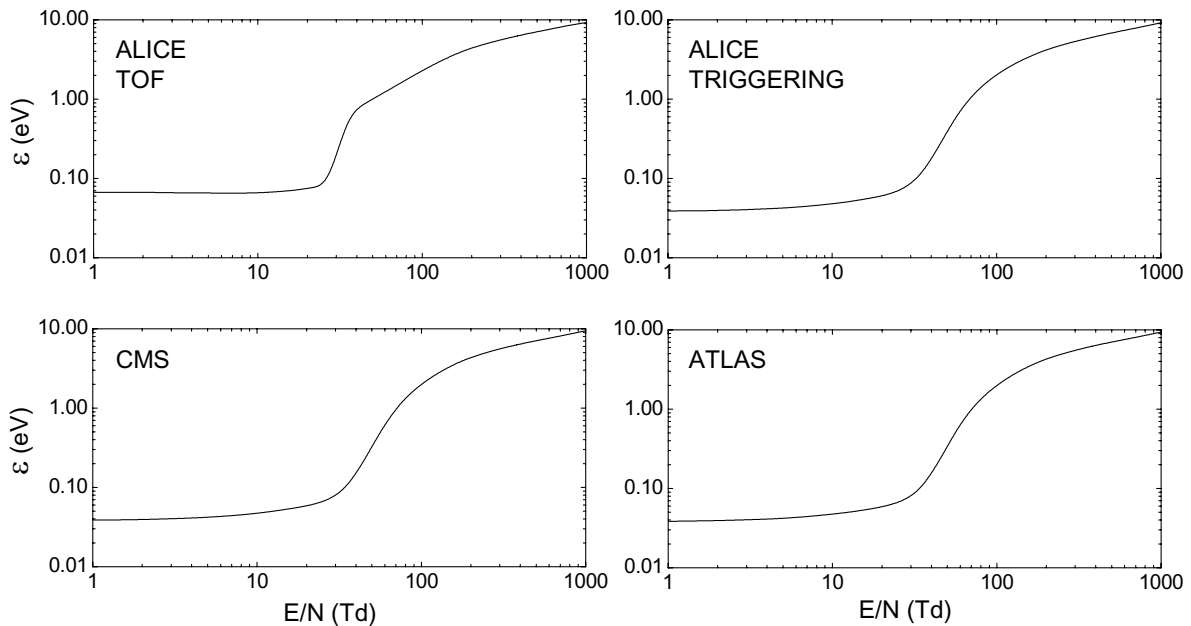


Figure 2. Variation of the mean energy with E/N for RPCs used in ALICE, CMS and ATLAS experiments at CERN.

excitations. Second, there is a region of sharp rise as the cross sections for vibrational excitations drop off and electrons start to gain energy from the electric field rapidly. Finally, there is another region of slow rise in the mean energy as new inelastic channels including the electronic excitation, neutral dissociation and ionization become open. The variation of the mean energy with E/N in these three RPCs systems is almost identical due to small differences in the abundances of $C_2H_2F_4$ and iso- C_4H_{10} in the gas mixtures. The amount of SF_6 in these systems is the same and set to 0.3%.

However, for ALICE timing RPC the situation is more interesting. In this system the amount of SF_6 in the gas mixture is much higher and the electron transport is greatly affected by electron attachment. In the limit of the lowest E/N considered in this work (less than 10 Td) and contrary to the results for other RPC systems, we see that for increasing E/N the mean energy varies very slowly and essentially stays unaltered. We also observe that the mean energy is significantly higher than thermal electron energy $\left(\frac{3}{2}kT\right)$ indicating the presence of an additional heating mechanism for electrons. This unusual situation follows from the combined effects of attachment heating and inelastic cooling. The term *inelastic cooling* simply refers to the fact that whenever an electron undergoes an inelastic collision it loses at least the threshold energy of the excitation process and emerges from the collision with reduced energy. In the energy range of interest, the collision frequency for electron attachment (which leads to the formation of stable parent SF_6^- negative ion) decreases with the electron energy and the lower energy electrons which predominantly exist at the trailing edge of the swarm are preferentially consumed. As already discussed in section 3.2, under these conditions the mean energy is raised and bulk drift velocity is increased (see figure 3). However, due to inelastic cooling if the electrons have energy just above the threshold energy, then in any

inelastic encounter with a neutral they will lose almost all energy, resulting in a substantial cooling effect on the swarm, even if only a relatively small fraction of the electrons have the required energy. This is exactly what happens for electrons in ALICE timing RPC; due to attachment heating the mean energy is raised above thermal energy and due to inelastic cooling the mean energy cannot be further increased for increasing E/N as the collision frequency for inelastic collisions in this energy range rapidly increases with the electron energy.

In figure 3 we show the variation of the bulk and flux drift velocity with E/N for RPCs used in ALICE, CMS and ATLAS experiments at CERN. In all experiments the bulk component dominates the flux component over the entire E/N range considered in this work. For lower E/N this follows from the attachment heating while for higher E/N this is a consequence of the explicit effects of ionization on the drift velocity. The effects of electron attachment are stronger than those induced by ionization and are the most evident for ALICE timing RPC where differences between the bulk and flux values are of the order of 100% for lower E/N . For other RPC systems these differences are of the order of 10% for lower E/N while for higher E/N are around 20%.

The existence of negative differential conductivity (NDC) in the bulk drift velocity component with no indication of any NDC for the flux component in the ALICE timing RPC system is certainly one of the most striking phenomena observed in this work. NDC is a kinetic phenomenon which represents the decrease of the drift velocity with increasing driving electric field. From the plot of the drift velocity for ALICE timing RPC it is seen that electrons exhibit NDC in the bulk drift velocity for reduced electric fields between 30 Td and 100 Td. Conditions leading to this phenomenon have been extensively discussed by Petrović *et al* [46] and Robson [47]. In brief, it was concluded that NDC arise from certain combination of

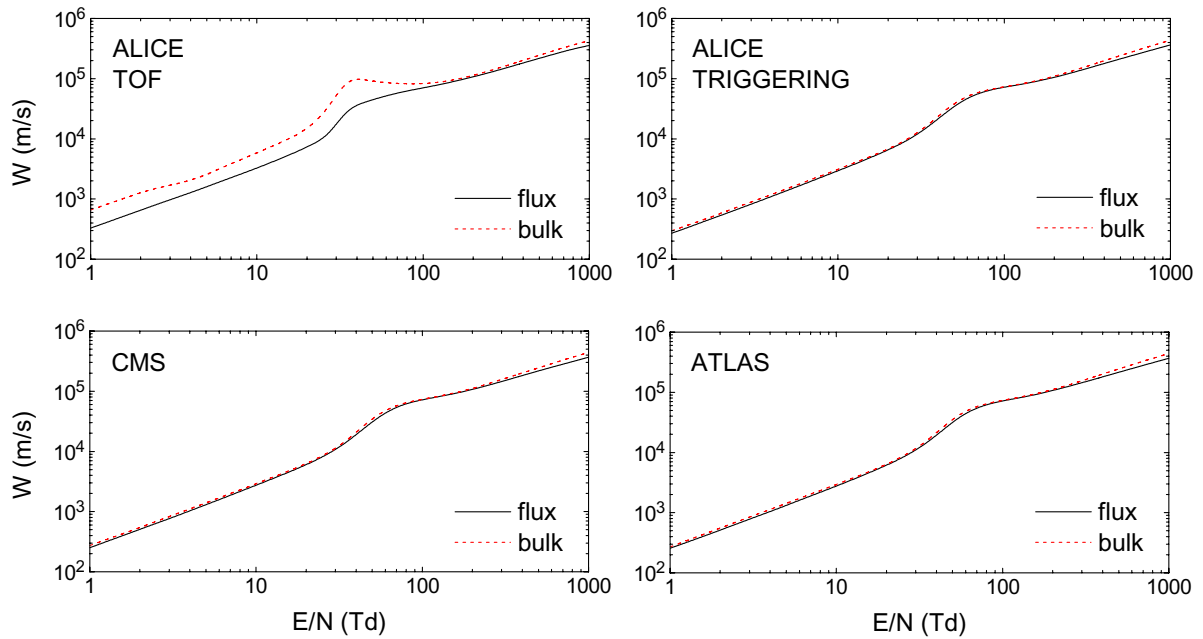


Figure 3. Variation of the bulk and flux drift velocities with E/N for RPCs used in ALICE, CMS and ATLAS experiments at CERN.

elastic-inelastic cross sections and is present in both the bulk and flux drift velocity components. The conditions for the attachment or ionization (non-conservative collision) induced NDC were first discussed by Vrhovac and Petrović [48] where it was concluded that the effect is possible but most likely to result in both bulk and flux drift velocities albeit at a different degree. This paper left a possibility that the flux drift velocity may not have NDC but a strongly developed plateau indicating that the NDC is on verge of being observable. This conclusion was based on the survey of observable effects for most gases with strong dissociative attachment.

In our case, however, NDC is present only in the bulk drift velocity which is a reminiscent of recently observed NDC effect for positrons in molecular gases [49, 50]. In these studies, it was concluded that NDC is induced by non-conservative nature of Positronium (Ps) formation. This conclusion has been confirmed in calculations where the Ps formation was treated as a conservative inelastic process; the NDC phenomenon has been removed from the profiles of the bulk drift velocity along with the differences between bulk and flux drift velocity components. Following the same strategy, we have treated electron attachment as a conservative inelastic process for SF_6 in our Boltzmann equation analysis. Results of our calculations are shown in figure 4. We see that NDC is absent from the profile of the bulk drift velocity and the only differences between the bulk and flux drift velocity are those originating from the explicit contribution of ionization for E/N higher than approximately 200 Td. The physical mechanisms behind the attachment induced NDC phenomenon is discussed in section 3.4.

In figures 5 and 6 we show the variation of the longitudinal and transverse diffusion coefficients with E/N for RPCs used in ALICE, CMS and ATLAS experiments at CERN. Both the bulk and flux values are shown and we see that all diffusion

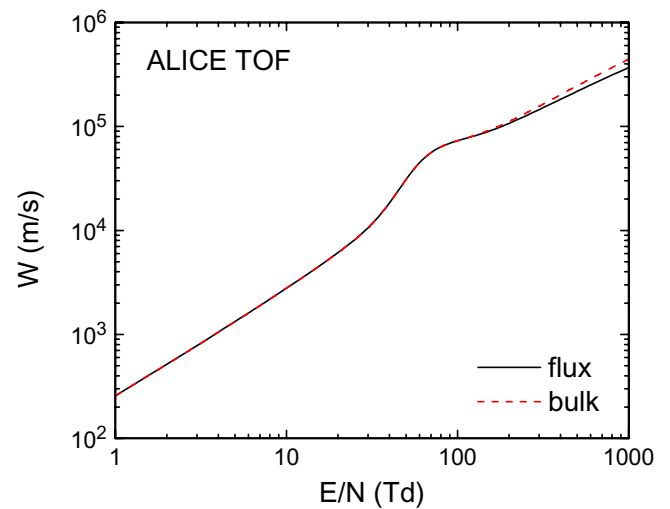


Figure 4. Variation of the bulk and flux drift velocity with E/N when electron attachment is treated as a conservative inelastic process for electrons in an ALICE timing RPC.

coefficients reflect to some degree the three distinct regions of electron transport discussed above. For ALICE triggering, CMS and ATLAS RPC systems, the variations of bulk and flux components of ND_L and ND_T with E/N are almost identical. Differences between the bulk and flux data for ND_L and ND_T are of the order of 20%. In these systems the differences between the bulk and flux values are only of quantitative nature and are not as high as those present between the bulk and flux values for ND_L and ND_T in the ALICE timing RPC system. In this case the bulk and flux components of the diffusion coefficients exhibit *qualitatively* different behavior; although as E/N increases both ND_L and ND_T generally increase, there exist certain regions of E/N where the bulk components of both ND_L and ND_T (and flux ND_L) are decreased for increasing E/N .

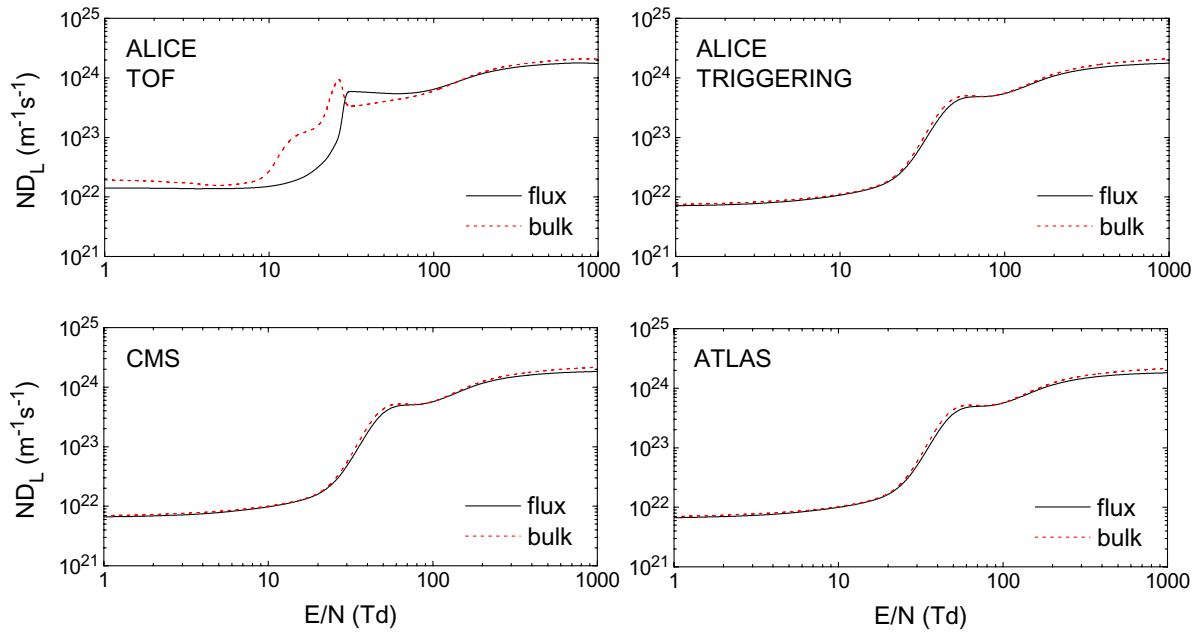


Figure 5. Variation of the longitudinal diffusion coefficient with E/N for RPCs used in ALICE, CMS and ATLAS experiments at CERN. Dashed lines are bulk coefficients while solid lines represent flux coefficients.

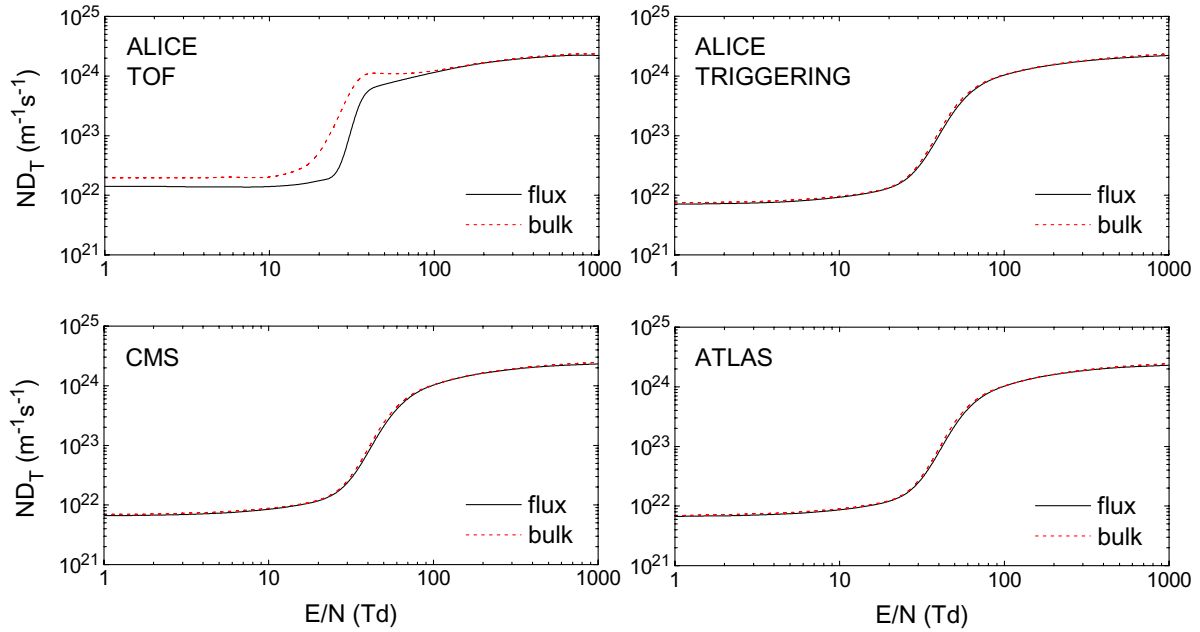


Figure 6. Variation of the transverse diffusion coefficient with E/N for RPCs used in ALICE, CMS and ATLAS experiments at CERN. Dashed lines are bulk coefficients while solid lines represent flux coefficients.

This illustrates the complexity of diffusion processes in general and for electrons in RPC systems at CERN indicating how difficult it is to understand the influence of non-conservative collisions on the diffusion coefficients. In brief, many parallel factors affect the diffusion simultaneously. In addition to the effects of thermal anisotropy (dispersion of electrons due to thermal motion is not the same in different directions) and anisotropy at elevated reduced electric fields (spatial variation of the average energy in conjunction with energy-dependent collision frequency produces differences in the average local

velocities for a given direction, which act to inhibit and/or enhance diffusion in that direction), there is always the contribution of non-conservative collisions and the complex energy dependence of electron attachment and ionization that even further complicate the physical picture. In conclusion, our results suggest a weak sensitivity of the diffusion coefficients with respect to electron attachment and ionization for ALICE triggering, CMS and ATLAS RPC systems and a much more complex behavior of diffusion processes for electrons in ALICE timing RPC.

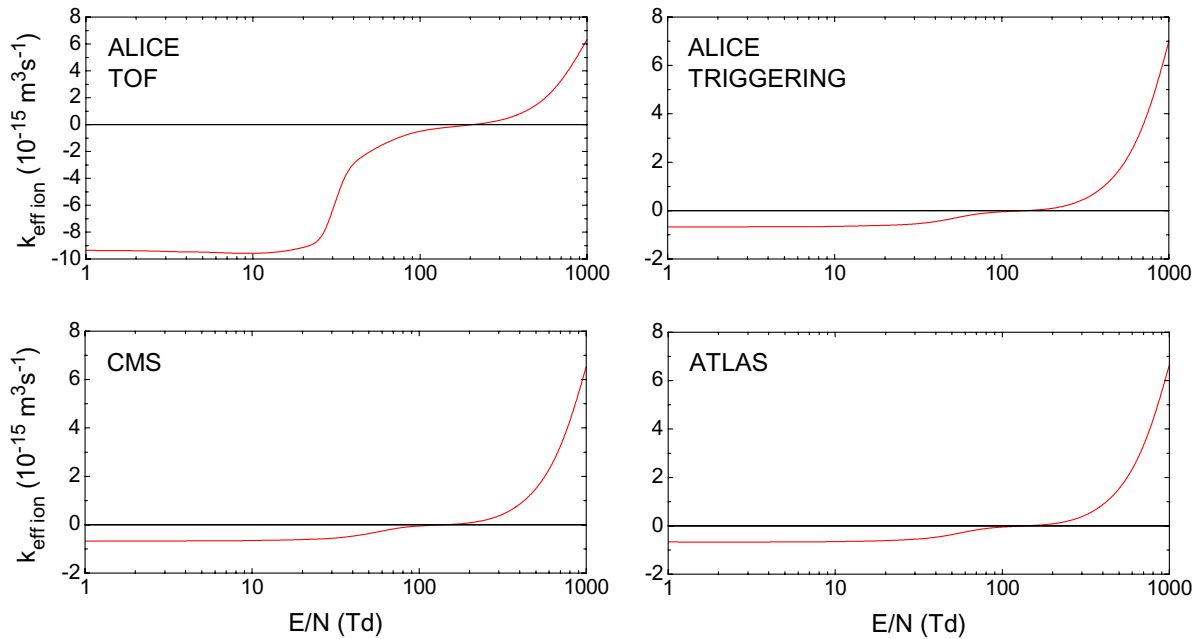


Figure 7. Variation of the effective ionization coefficient with E/N for RPCs used in ALICE, CMS and ATLAS experiments at CERN.

In figure 7 we show the variation of the effective ionization coefficient with E/N for RPCs used in ALICE, CMS and ATLAS experiments at CERN. The variation of this property with E/N is almost identical for ALICE triggering, CMS and ATLAS RPC systems due to small variations in the abundances of $C_2H_2F_4$ and iso- C_4H_{10} in the gas mixtures. The critical electric field for these systems is around 140 Td. The critical electric field for ALICE timing RPC is much higher, around 215 Td, due to higher abundance of SF_6 in the gas mixture and stronger effects of electron attachment on the electron energy distribution function.

3.4. Monte Carlo results for spatially resolved transport data and distribution function

While all results presented above may be reproduced exactly (for all practical purposes) by Monte Carlo simulation (albeit with a much more computing effort) there is a number of results important for RPC modeling that may be obtained by Monte Carlo technique with less difficulty and a more direct interpretation. In this section we show spatially resolved electron transport data that are sampled at every location over the entire swarm. The effect of the electric field on the spatial distribution of the electron transport data and distribution function is examined. In figure 8 we show the spatial profile and spatially resolved average energy for four different values of E/N as indicated in the graphs. The Monte Carlo simulations were simplified by assuming stationary gas ($T = 0$ K). This is the reason why our Monte Carlo results for electron transport coefficients are slightly shifted to the left, towards lower E/N comparing to our Boltzmann equation results obtained for the gas temperature of 293 K (not shown here). As a consequence, according to our Monte Carlo simulations the NDC occurs approximately between 20 Td and 77 Td while the

Boltzmann equation analysis suggest the NDC between 30 Td and 100 Td. One should bear this in mind in the following discussions.

In addition to our actual results given by solid lines where electron attachment is treated as a true non-conservative process, the results denoted by the dashed lines are obtained assuming electron attachment as a conservative inelastic process with zero energy loss. When electron attachment is treated as a conservative inelastic process, the spatial profile of electrons is almost perfectly symmetric and it has a typical Gaussian profile independently of the applied E/N . The spatially resolved average energy has a characteristic slope indicating spatially anisotropic distribution of the electron energy. There are no imprinted oscillations in the spatial profile of the electrons or in the profile of the average energy indicating the collisional energy loss is governed essentially by ‘continuous’ energy loss processes [51].

When electron attachment is treated regularly, as a true non-conservative process, we observe dramatic modifications to the spatial profile of the electron density and to the spatially resolved average energy. For E/N of 5.9 Td and 10 Td the spatial profile of electrons is no longer Gaussian while for E/N of 21 Td the spatial profile exhibits an asymmetric Gaussian distribution whose height is significantly decreased comparing to the Gaussian profile of the swarm when electron attachment is treated as a conservative inelastic process. For $E/N = 5.9$ Td we see that the average energy is essentially spatially uniform along the swarm. This is indicative of our normalization procedure: the spatial profile is not symmetric and number of electrons attachments is also asymmetric along the swarm and combination of these two yields a little spatial variation of the average energy along the swarm. For $E/N = 10$ Td, however, we observe that the trailing edge of the swarm is drastically cut off while the average energy remains

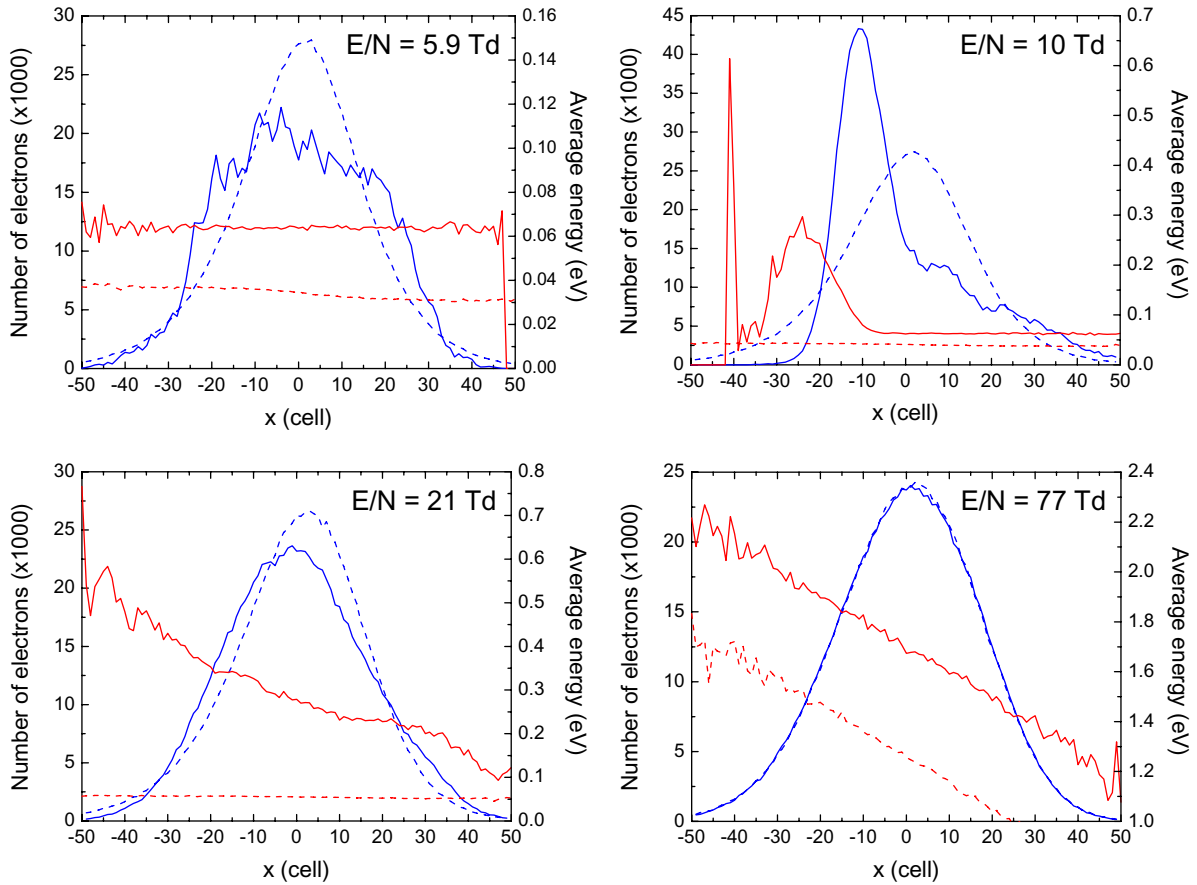


Figure 8. Spatial profile of electrons (blue curves) and spatially resolved averaged energy (red curves) at four different E/N in ALICE timing RPC. Full lines denote the results when electron attachment is treated as a non-conservative process, while the dashed lines represent our results when electron attachment is treated as a conservative inelastic process. ($t = 1$ ns).

essentially constant otherwise. At the leading edge of the swarm, the average energy is raised with a much steeper slope towards the front. Before reaching the highest energy at the leading edge of the swarm, there is a spatial region where the average energy is first drastically decreased, and then rapidly increased in a very narrow spatial region. For $E/N = 21$ Td the spatial dependence of the average energy is almost linear and no sharp jumps and drop-offs in the profile are observed. For increasing E/N the average electron energy increases and there are fewer and fewer electrons available for attachment. Thus the explicit contribution of electron attachment is further reduced which in turns removes the differences between the bulk and flux components of the drift velocity and diffusion coefficients in the energy region where NDC occurs. Finally for $E/N = 77$ Td, the spatial profile of electrons almost coincides with the profile obtained under conditions when electron attachment is treated as a conservative inelastic process. In both cases the average energy linearly increases from the trailing edge towards the leading part of the swarm. This is regime when electron attachment has no longer dominant control over the electron swarm behavior.

The spatially resolved attachment rates are shown in figure 9 and are calculated under the same conditions as for the spatial profile of the electrons and spatially averaged energy. They have complex profiles that reflect the overlap of the average energy and the corresponding cross sections. The

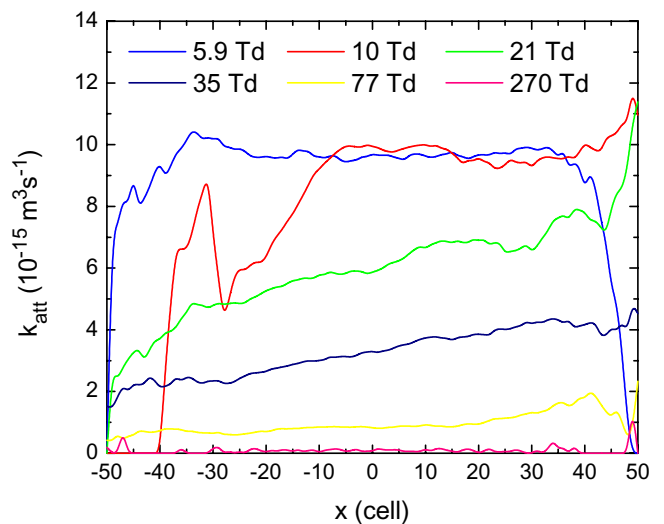


Figure 9. Spatially resolved attachment rate coefficient for a range of E/N in ALICE timing RPC. ($t = 1$ ns).

attachment rate is generally higher at the trailing edge of the swarm where the average energy of the electrons is lower and exactly these lower energy electrons are most likely to be consumed by electron attachment. This results in a forward shift of the centre of mass of the electron swarm, which is observable as an increase of the bulk drift velocity over the flux

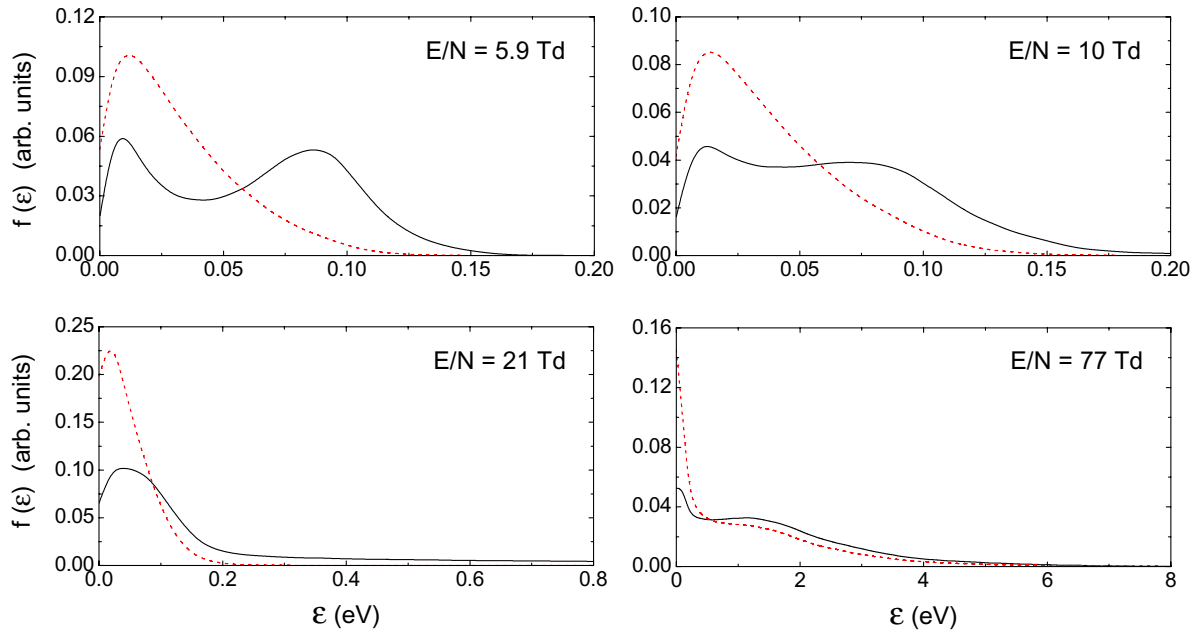


Figure 10. Electron energy distribution functions for four different E/N in ALICE timing RPC. Black lines denote the results when electron attachment is treated as non-conservative process while dashed red lines represent our results when electron attachment is treated as a conservative inelastic process. ($t = 1$ ns).

values as discussed above. For increasing E/N the spatially resolved rate coefficients are decreased suggesting much less impact of electron attachment on the electron swarm behavior.

When electron transport is greatly affected by non-conservative collisions it is often very useful to look at the energy distribution functions in order to make conclusions about the underlying physics of some processes. In figure 10 we show the electron energy distribution functions for the same four values of E/N considered above. The electron energy distribution functions are calculated when electron attachment is treated regularly as a true non-conservative process (black line) and under conditions when electron attachment is assumed to be a conservative inelastic process (dash red line). We see that strong electron attachment induces a ‘hole burning’ in the electron energy distribution function. For decreasing E/N the electron energy is generally reduced and the attachment cross section becomes larger. As a result the effect of electron loss on the distribution function increases. This phenomenon has been extensively discussed for electrons in O_2 [52] and O_2 mixtures [29, 53] and under conditions leading to the phenomenon of absolute negative electron mobility [26, 27]. The same effect is not present when attachment is treated as a conservative inelastic process. Under these conditions, we see that the population of low energy electrons is much higher than the corresponding situation when electron attachment is treated regularly. For increasing E/N , the population of high energy electrons becomes well described even when electron attachment is treated as a conservative inelastic process.

4. Conclusion

In this work, we have presented the results of a systematic investigation of non-conservative electron transport in the

mixtures of $C_2H_2F_4$, iso- C_4H_{10} and SF_6 used in RPCs in ALICE, CMS and ATLAS experiments at CERN. We have considered conditions consistent with the electrons in an avalanche and streamer mode of operation of these RPC systems with partial motivation being the provision of transport coefficients to be employed in fluid modeling of such systems. Transport coefficients presented in this work are given as a function of E/N and are accurate to within 2%. The E/N -dependence of electron transport coefficients for ALICE triggering, CMS and ATLAS RPC systems are almost identical due to similar composition of the corresponding gas mixtures. The bulk drift velocity is slightly higher than flux component even for lower E/N indicating the presence of attachment heating. When ionization dominates attachment the difference between the bulk and flux drift velocities is further increased. The most striking phenomenon observed in this work is the existence of NDC in the bulk drift velocity component with no indication of any NDC for the flux component in the ALICE timing RPC system. This phenomenon was predicted as possible [48] but has never been observed for electrons primarily as the dominance of explicit effects and strongly energy dependent attachment were sought due to limitations of the momentum transfer theory that was employed in that paper. In order to understand the physical mechanisms behind of this atypical manifestation of the drift velocity, we have calculated spatially resolved transport properties and energy distribution functions for electric fields critical for occurrence of this phenomenon. It was found that the attachment heating governs the phenomenon and plays the dominant role in consideration of non-conservative effects on various transport properties. A ‘hole burning’ in the distribution function has been observed illustrating the richness and complexity of electron transport phenomena in RPCs.

Acknowledgments

DB, ZLjP and SD acknowledge support from MPNTRRS Projects OI171037 and III41011. RDW is supported by the Australian Research Council.

References

- [1] Santonico R and Cardarelli R 1981 *Nucl. Instrum. Methods* **187** 377–80
- [2] Riegler W, Lippmann C and Veenhof R 2003 *Nucl. Instrum. Methods A* **500** 144–62
- [3] Riegler W and Lippmann C 2004 *Nucl. Instrum. Methods A* **518** 86–90
- [4] Santonico R 2012 *Nucl. Instrum. Methods A* **661** S2–5
- [5] Fonte P 2002 *IEEE Trans. Nucl. Sci.* **49** 881–7
- [6] Fonte P 2013 *J. Instrum.* **8** P11001
- [7] The ATLAS Collaboration 2008 *J. Instrum.* **3** S08003
- [8] The ALICE Collaboration 2008 *J. Instrum.* **3** S08002
- [9] The CMS Collaboration 2008 *J. Instrum.* **3** S08004
- [10] Blanco A, Couceiro M, Crespo P, Ferreira N C, Ferreira Marques R, Fonte P, Lopes L and Neves J A 2009 *Nucl. Instrum. Methods A* **602** 780–3
- [11] Couceiro M, Crespo P, Mendes L, Ferreira N, Ferreira Marques R and Fonte P 2012 *Nucl. Instrum. Methods A* **661** S156–8
- [12] Cârloganu C et al 2013 *Geosci. Instrum. Methods Data Syst.* **2** 55–60
- [13] Abbrescia M, Cassano V, Nuzzo S, Piscitelli G, Vadrucchio D and Zaza S 2012 *Nucl. Instrum. Methods A* **661** S190–3
- [14] Riegler W 2009 *Nucl. Instrum. Methods A* **602** 377–90
- [15] Mangiarotti A, Fonte P and Gobbi A 2004 *Nucl. Instrum. Methods A* **533** 16–21
- [16] Khosravi Khorashad L, Moshaii A and Hosseini S 2011 *Europhys. Lett.* **96** 45002
- [17] Khosravi Khorashad L, Eskandari M and Moshaii A 2011 *Nucl. Instrum. Methods A* **628** 470–3
- [18] Moshaii A, Khosravi Khorashad L, Eskandari M and Hosseini S 2012 *Nucl. Instrum. Methods A* **661** S168–71
- [19] Petrović Z Lj, Dujko S, Marić D, Malović G, Nikitović Ž, Šašić O, Jovanović J, Stojanović V and Radmilović-Radenović M 2009 *J. Phys. D: Appl. Phys.* **42** 194002
- [20] White R D, Robson R E, Dujko S, Nicoletopoulos P and Li B 2009 *J. Phys. D: Appl. Phys.* **42** 194001
- [21] Biagi S F 1999 *Nucl. Instrum. Methods A* **421** 234–40
- [22] Doroud K, Afarideh H, Hatzifotiadou D, Rahighi J, Williams M C S and Zichichi A 2009 *Nucl. Instrum. Methods A* **610** 649–53
- [23] Robson R E 1991 *Aust. J. Phys.* **44** 685
- [24] Lopes L, Fonte P and Mangiarotti A 2012 *Nucl. Instrum. Methods A* **661** S194–7
- [25] Christophorou L G and Olthoff J K 2000 *J. Phys. Chem. Ref. Data* **29** 267
- [26] Dyatko N A, Napartovich A P, Sakadzic S, Petrovic Z and Raspopovic Z 2000 *J. Phys. D: Appl. Phys.* **33** 375–80
- [27] Dujko S, Raspopovic Z M, Petrovic Z L and Makabe T 2003 *IEEE Trans. Plasma Sci.* **31** 711–6
- [28] Bošnjaković D, Petrović Z Lj and Dujko S 2014 A microscopic Monte Carlo approach in modeling of resistive plate chambers *J. Instrum.* submitted
- [29] Dujko S, Ebert U, White R D and Petrović Z Lj 2011 *Japan. J. Appl. Phys.* **50** 08JC01
- [30] Boltzmann L 1872 *Wien. Ber.* **66** 275
- [31] Wang-Chang C S, Uhlenbeck G E and de Boer J 1964 *Studies in Statistical Mechanics* **2** (New York: Wiley) p 241
- [32] Robson R E and Ness K F 1986 *Phys. Rev. A* **33** 2068–77
- [33] Ness K F and Robson R E 1986 *Phys. Rev. A* **34** 2185–209
- [34] Dujko S, White R D, Petrović Z Lj and Robson R E 2010 *Phys. Rev. E* **81** 046403
- [35] Legler W 1961 *Z. Naturf.* **16a** 253
- [36] Raspopović Z M, Sakadžić S, Bzenić S A and Petrović Z Lj 1999 *IEEE Trans. Plasma Sci.* **27** 1241–8
- [37] Petrović Z Lj, Raspopović Z M, Dujko S and Makabe T 2002 *Appl. Surf. Sci.* **192** 1–25
- [38] Li Y M, Pitchford L C and Moratz T J 1989 *Appl. Phys. Lett.* **54** 1403
- [39] Yousfi M, Hennad A and Alkaa A 1994 *Phys. Rev. E* **49** 3264–73
- [40] Dujko S, Markosyan A H, White R D and Ebert U 2013 *J. Phys. D: Appl. Phys.* **46** 475202
- [41] Markosyan A H, Dujko S and Ebert U 2013 *J. Phys. D: Appl. Phys.* **46** 475203
- [42] Šašić O, Dupljanin S, de Urquijo J and Petrović Z Lj 2013 *J. Phys. D: Appl. Phys.* **46** 325201
- [43] Itoh H, Matsumura T, Satoh K, Date H, Nakao Y and Tagashira H 1993 *J. Phys. D: Appl. Phys.* **26** 1975–9
- [44] Bošnjaković D, Dujko S, Petrović Z Lj 2012 Electron transport coefficients in gases for resistive plate chambers *Proc. of the 26th Summer School and Int. Symp. on the Physics of Ionized Gases* (Zrenjanin, Serbia, 27–31 August) Kuraica M and Mijatović Z (Bristol: IOP) pp 265–8
- [45] Bošnjaković D, Petrović Z Lj and Dujko S 2013 Monte Carlo modelling of resistive plate chambers *Proc. of the XVII Int. Workshop on Low-Energy Positron and Positronium Physics and the XVIII Int. Symposium on Electron-Molecule Collisions and Swarms* (Kanazawa, Japan, 19–21 July) p 44
- [46] Petrović Z Lj, Crompton R W and Haddad G N 1984 *Aust. J. Phys.* **37** 23
- [47] Robson R E 1984 *Aust. J. Phys.* **37** 35
- [48] Vrhovac S B and Petrović Z Lj 1996 *Phys. Rev. E* **53** 4012–25
- [49] Banković A, Dujko S, White R D, Marler J P, Buckman S J, Marjanović S, Malović G, García G and Petrović Z Lj 2012 *New J. Phys.* **14** 035003
- [50] Banković A, Dujko S, White R D, Buckman S J and Petrović Z Lj 2012 *Nucl. Instrum. Methods B* **279** 92–5
- [51] Dujko S, White R D, Raspopović Z M and Petrović Z Lj 2012 *Nucl. Instrum. Methods B* **279** 84–91
- [52] Skullerud H R 1983 *Aust. J. Phys.* **36** 845
- [53] Hegerberg R and Crompton R W 1983 *Aust. J. Phys.* **36** 831

A microscopic Monte Carlo approach to modeling of Resistive Plate Chambers

D. Bošnjaković,^{a,b,1} Z.Lj. Petrović^{a,b} and S. Dujko^a

^a*Institute of Physics,*

University of Belgrade, Pregrevica 118, 11070 Belgrade, Serbia

^b*Faculty of Electrical Engineering,*

University of Belgrade, Bulevar kralja Aleksandra 73, 11120 Belgrade, Serbia

E-mail: dbosnjak@ipb.ac.rs

ABSTRACT: We present a “microscopic” approach in modeling of Resistive Plate Chambers where individual electrons and their collisions with the gas molecules are followed using a Monte Carlo simulation technique. Timing resolutions and efficiencies are calculated for a specific timing RPC with 0.3 mm gas gap and gas mixture of 85% C₂H₂F₄ + 5% iso-C₄H₁₀ + 10% SF₆. Calculations are performed for different sets of cross sections for electron scattering in C₂H₂F₄ and primary cluster size distributions. Results of calculations are compared with those obtained in experimental measurements. Electron avalanche fluctuations are also studied and compared with analytical models.

KEYWORDS: Resistive-plate chambers; Detector modelling and simulations II (electric fields, charge transport, multiplication and induction, pulse formation, electron emission, etc); Charge transport and multiplication in gas; Gaseous detectors

¹Corresponding author.

Contents

| | | |
|----------|---|-----------|
| 1 | Introduction | 1 |
| 2 | Simulation technique | 2 |
| 2.1 | Primary ionization | 2 |
| 2.2 | Electron tracking | 3 |
| 2.3 | Signal induction | 4 |
| 3 | Results and discussion | 4 |
| 3.1 | Preliminaries | 4 |
| 3.2 | Single-electron avalanches | 6 |
| 3.3 | Avalanches started by primary ionization | 8 |
| 3.4 | Full model with primary ionization and boundaries | 8 |
| 4 | Summary and conclusions | 11 |

1 Introduction

Developed in the 1980s [1, 2], Resistive Plate Chambers (RPCs) became widely used particle detectors in high energy physics experiments [3–5]. Electrodes of highly resistive material, such as glass or bakelite, make them free from destructive discharges. They also show remarkable timing resolutions of about 50 ps [6]. Due to their simple construction and low cost, they are often used for large area timing and triggering purposes, but other applications such as medical imaging were also considered [7].

Despite their apparent simplicity, modeling of RPCs is not an easy task because of various physical phenomena ranging from charge generation, transport and multiplication, to signal induction, propagation and electrode relaxation effects, all occurring on different time scales. Yet, many RPC models were developed and published [8]. Most numerical models are based on either the Monte Carlo simulation technique [9, 10] or on the fluid equations [11, 12]. The latter can only provide the mean values of RPC signals in a deterministic fashion while the Monte Carlo models usually follow some theoretical distributions for primary ionization and electron avalanche fluctuations in order to calculate the RPC performance characteristics such as timing resolution, efficiency and charge spectrum. On the other hand, while often being approximate, only the analytical models [13, 14] can provide general conclusions about the influence of different parameters on the RPC performance. These models can also include the stochastic effects in physics of RPCs.

Every RPC model relies on accurate data for electron swarm transport in gases. These parameters include the transport coefficients (e.g. drift velocity and diffusion coefficients) and rate coefficients (e.g. attachment and ionization rate) which are usually calculated from electron impact cross sections using a computer code based on either Monte Carlo method or Boltzmann equation

analysis. A Monte Carlo code that is often used for such purpose — MAGBOLTZ 2 [15, 16] has cross sections imbedded into the code. Thus cross sections cannot be easily modified, compared or presented. The questions associated with the reliability of cross sections for electron scattering in RPC’s gases were already raised in case of $C_2H_2F_4$ [17], which is the main component in gas mixtures for RPCs operated in avalanche mode. As will be shown, the final results that describe the RPC performance may differ considerably depending on the cross sections used.

In this paper, we follow a completely different approach in RPC modeling. Our approach is based on 3D tracking of individual electrons and their collisions with the background gas in a typical Monte Carlo fashion. Here the avalanche fluctuations and the RPC performance characteristics emerge naturally from the stochastic character of electron collisions and are determined exclusively by the cross sections for electron scattering. Such an approach based on MAGBOLTZ was used for the calculation of gas gain fluctuations [18] but still, no such attempts in RPC modeling were published [17].

This paper is organized as follows. First, we discuss our simulation technique (section 2). Then, we present the results for electron avalanches in an infinite space (sections 3.2 and 3.3) which are used for comparison with the analytical models of avalanche development and timing. Finally, the boundaries are introduced (section 3.4) and timing and efficiency are calculated for a specific timing RPC (0.3 mm gas gap, gas mixture of 85% $C_2H_2F_4$ + 5% iso- C_4H_{10} + 10% SF_6). A study is made with different cross section sets and cluster size distributions. The results are compared with experimental values. Due to limited computing resources we are only able to use a relatively low value of signal threshold of about 10^6 electrons which excludes the space charge effects.

2 Simulation technique

Our simulation technique for an RPC event (i.e. passage of an incoming particle) can be divided into a few steps. First, we generate the primary ionization, e.g., the initial electrons due to passage of the incoming particle. The individual electrons and their collisions with the background gas are then traced between the moments of sampling. In these moments, we record some quantities (e.g. number of electrons) and calculate the induced signal. Sampling interval is set to 0.2 ps. The threshold crossing time is determined using the exponential interpolation between the samples. The simulation consisting of 10000 events usually takes approximately two days of computation time on a multiprocessor system with about 300 active CPU cores @ 2.1 GHz.

2.1 Primary ionization

Primary ionization is generated according to a commonly used model. The primary electrons are grouped in clusters. Electrons belonging to the same cluster have the same initial position. Number of electrons in the cluster is generated using a cluster size distribution. The positions of the clusters are generated using exponential distribution for the distance between neighboring clusters

$$P(x) = \frac{1}{\lambda} \exp\left(-\frac{x}{\lambda}\right),$$

where λ is the mean distance between clusters. Initial velocity of primary electrons is chosen according to the Maxwellian velocity distribution with the mean electron energy of 1 eV. Mean

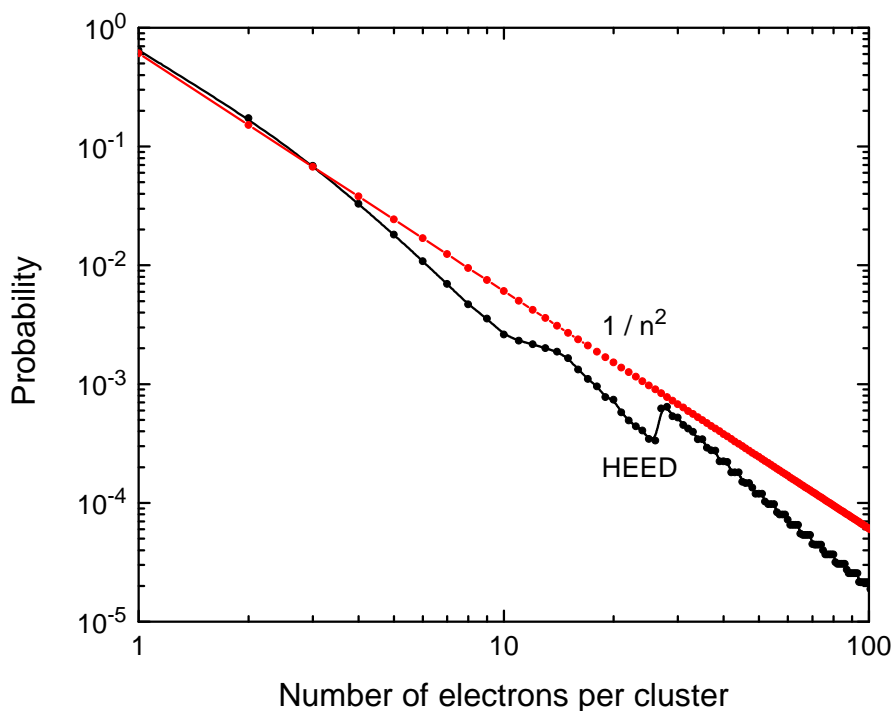


Figure 1. Cluster size distribution calculated by HEED, and $1/n^2$ model.

distance between the clusters and cluster size distribution are calculated using a computer program HEED [19, 20]. For minimum ionizing particles, we have obtained a value of 8.44 clusters/mm, which differs from 7.5 clusters/mm quoted in [21]. Considering the arguments and measurements presented in [21], we have decided to use the value of 7.5 clusters/mm since it seems more realistic. For cluster size distributions we use two models in our simulations for comparison: the $1/n^2$ model and the distribution calculated by HEED (figure 1). Both distributions are cut to 500 electrons.

2.2 Electron tracking

In the work reported here, the Monte Carlo method is used to simulate the motion of electrons in the background gas. In the present Monte Carlo code both elastic and inelastic collisions are assumed to occur in the interactions of the electrons with the gas molecules. The electron-electron interactions are neglected since the transport is considered in the limit of low electron density. Calculations are performed at zero gas temperature and isotropic scattering is assumed to occur in all electron-molecule collisions regardless of the nature of specific processes or energy.

Spatiotemporal evolution of each electron is followed through a time step determined from the mean free time between collisions. This small time step is used to solve the integral equation for the collision probability in order to determine the time of the next collision. This can be done using either the null collision technique or integration technique. In our code (and in contrast to MAGBOLTZ) the latter approach is employed. The number of time steps is determined in such a way as to optimize the performance of the Monte Carlo code without reducing the accuracy of the final results. After a collision has occurred, it is then determined whether the electron has collided elastically or experienced one of the several possible types of inelastic events, by using the relative

probabilities of various collision types. When an elastic collision has occurred, the electron energy is reduced by the amount $2m/M$ where m and M are the electron and molecule masses, respectively. In an inelastic collision the electron is assumed to lose an amount of energy corresponding to the energy loss for that particular process. After ionization, it is assumed that all fractions of the distribution of the available energy are equally probable between primary and secondary electrons. When electron attachment takes place, the consumed electron is simply removed from the simulation. Under the hypothesis of isotropic scattering, the change in direction of the electron velocity after a collision is expressed by uniformly distributed scattering angle within interval $[0, \pi]$ and by the azimuthal angle uniformly distributed within the interval $[0, 2\pi]$. For more details on our Monte Carlo simulation technique the reader is referred to our recent reviews [22–24].

In the present work we have employed three different sets of cross sections for electron scattering in $C_2H_2F_4$: 1) a set recently developed by our group [25], 2) a set from MAGBOLTZ 2.8.9 (2010), and 3) a set from MAGBOLTZ 2.7.1 (pre-2010). The set developed by our group and the set from MAGBOLTZ 2.8.9 have been recently updated and modified on the basis of new experimental measurements of electron transport data in $C_2H_2F_4$ under the pulsed Townsend conditions [26]. For electron scattering in iso- C_4H_{10} , we have used a set of cross sections from MAGBOLTZ 2.7.1. There is an updated version of the same cross sections hard-coded in more recent versions of MAGBOLTZ but our calculations have revealed much better agreement between our data for ionization coefficient and those experimentally measured [27], if the cross sections from MAGBOLTZ 2.7.1 are considered [27, 28]. Finally, for electron scattering in SF_6 we have employed a set of cross sections developed by Itoh et al. [29].

2.3 Signal induction

The induced current in an electrode is calculated using Ramo’s theorem [30]:

$$i(t) = \frac{E_w}{V_w} \cdot q \cdot n(t) \cdot w(t),$$

where E_w is the weighting field of the electrode (calculated as electric field in the gas gap when the electrode is raised to the potential of V_w while the other electrodes are grounded), q is the electron charge, and n is the number of electrons and w represents the flux drift velocity. The flux drift velocity is the average electron velocity while the bulk drift velocity is defined as velocity of center of mass of the electron swarm (avalanche) [31, 32]. The two may differ quantitatively and sometimes even qualitatively when non-conservative collisions such as attachment and/or ionization are present [33]. For our RPC geometry (0.3 mm gas gap, one metallic and one 3 mm thick glass electrode with $\epsilon_r = 8$) the weighting field of 1.48/mm was calculated. The induced charge is calculated as an integral of the induced current, $q(t) = \int_0^t i(\tau) d\tau$.

3 Results and discussion

3.1 Preliminaries

First we give a brief summary of the most important parameters used in the following sections. We consider the gas mixture of 85% $C_2H_2F_4$, 5% iso- C_4H_{10} and 10% SF_6 and the gas number density is set to $N = 2.505 \cdot 10^{25} \text{ m}^{-3}$ which corresponds to the pressure of 1 atm and temperature of 20°C).

Table 1. Calculated $S = (\alpha - \eta)w$ and $k = \eta/\alpha$ parameters for a mixture of 85% $C_2H_2F_4$ + 5% iso- C_4H_{10} + 10% SF_6 with three different $C_2H_2F_4$ cross section sets. All calculations presented here are made using our Monte Carlo method.

| E/N (Td) | <i>Our set</i> | | <i>MAGBOLTZ 2.8.9 set</i> | | <i>MAGBOLTZ 2.7.1 set</i> | |
|-------------|------------------------|-----------------|---------------------------|-----------------|---------------------------|-----------------|
| | S ($10^{10} s^{-1}$) | k | S ($10^{10} s^{-1}$) | k | S ($10^{10} s^{-1}$) | k |
| 359 | 1.27 ± 0.04 | 0.20 ± 0.01 | 1.40 ± 0.04 | 0.16 ± 0.01 | 1.66 ± 0.04 | 0.16 ± 0.01 |
| 385 | 1.62 ± 0.04 | 0.16 ± 0.01 | 1.77 ± 0.04 | 0.13 ± 0.01 | 2.14 ± 0.04 | 0.13 ± 0.01 |
| 412 | 2.01 ± 0.04 | 0.13 ± 0.01 | 2.20 ± 0.04 | 0.10 ± 0.01 | 2.68 ± 0.05 | 0.10 ± 0.01 |
| 439 | 2.43 ± 0.05 | 0.11 ± 0.01 | 2.67 ± 0.05 | 0.08 ± 0.01 | 3.26 ± 0.05 | 0.08 ± 0.01 |

The reduced electric field E/N is expressed in Td ($1 \text{ Td} = 10^{-21} \text{ Vm}^2$). The primary ionization is generated assuming the mean value of 7.5 clusters/mm for minimum ionizing particles. Velocity of the initial electron(s) is chosen according to the Maxwellian velocity distribution with the mean starting energy of 1 eV. Induced signal is calculated using the weighting field of $E_w/V_w = 1.48/\text{mm}$. The gas gap is 0.3 mm.

Our simulation results are compared with those obtained in an analytical model for time response functions [13]. The model shows that, except for small thresholds (e.g. less than 1000 electrons), the RPC time response function can be written as

$$\rho(n_{\text{th}}, t) = \frac{1}{2\pi i} \oint_{|z|=r} \frac{\exp(n_{\text{cl}}F(z)) - 1}{\exp(n_{\text{cl}}) - \exp(n_{\text{cl}}F(1/k))} \frac{(1-k^2)n_{\text{th}}S}{(1-kz)^2} \cdot \exp\left(-St - n_{\text{th}} \frac{(1-k)(1-z)}{1-kz} \exp(-St)\right) dz, \quad (3.1)$$

where n_{th} and n_{cl} are the threshold given as number of electrons and the mean number of clusters (in our simulation $2.25 = 7.5/\text{mm} \cdot 0.3 \text{ mm gas gap}$), respectively; $F(z)$ and $S = (\alpha - \eta)w$ are the Z -transform of cluster size distribution with radius of convergence r_F and the effective ionization rate, respectively; α and η are the ionization coefficient and attachment coefficient, respectively; and w is the flux drift velocity and $k = \eta/\alpha$. The integration is made over a circle with radius $r_F < r < 1/k$. Using the expression (3.1), it can easily be shown that the shape of the time response function does not depend on the threshold level. It is only shifted in time, and thus the timing resolution does not depend on the threshold. This is a well know experimental observation [6]. One should note that this model does not include the space charge effects and the effects induced by the gas gap boundaries, i.e. an infinite space is assumed. In addition, when comparison is made with our timing distributions, the theoretical time response functions (3.1) are shifted in time so that their mean threshold crossing time is equal to that of simulated data. Table 1 shows the S and k parameters for different $C_2H_2F_4$ cross section sets and electric field strengths calculated using our Monte Carlo method described in section 2.2.

The analytical model presented above is based on the Legler's basic theory of avalanche statistics [34]. This theory is also used by some other analytical and numerical models [8]. According to this theory the probability for an avalanche, initiated by one electron, to have n electrons after

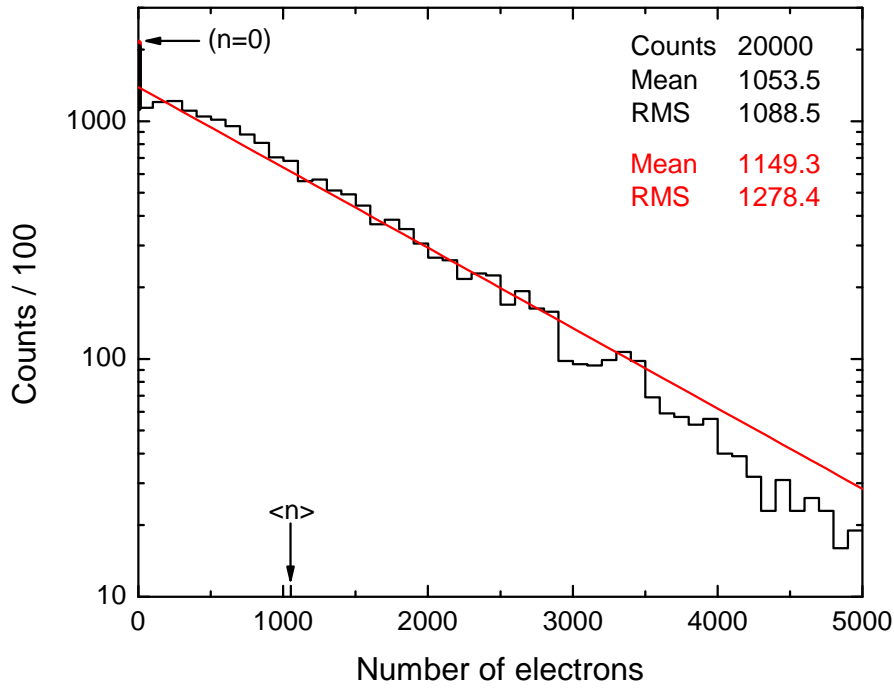


Figure 2. Avalanche size distribution at $t = 290$ ps. (Red) comparison with Legler’s model (3.2). Our cross sections for $C_2H_2F_4$ [25] are assumed. $E/N = 439$ Td.

path x is given by

$$P(n,x) = \begin{cases} k \frac{\bar{n}(x) - 1}{\bar{n}(x) - k}, & n = 0 \\ \bar{n}(x) \left(\frac{1 - k}{\bar{n}(x) - k} \right)^2 \left(\frac{\bar{n}(x) - 1}{\bar{n}(x) - k} \right)^{n-1}, & n > 0 \end{cases} \quad (3.2)$$

where $\bar{n}(x) = \exp((\alpha - \eta)x)$ is the mean avalanche size at the position x . This distribution has a characteristic exponential shape which has been experimentally confirmed for many gases at lower electric field strengths. But at higher electric fields, a prominent deviation was noticed and could be attributed to the approximation of constant ionization coefficient used by this model [35]. Also, one should bear in mind that x is the position of avalanche center of mass and therefore α and η should be regarded as “bulk” coefficients, i.e. calculated using the bulk drift velocity. However, if the probability $P(n,x)$ is considered as time dependent (3.1), then the distinction between flux and bulk values is not necessary since in each case \bar{n} reduces to $\bar{n}(t) = \exp(St)$ where S is the effective ionization rate.

3.2 Single-electron avalanches

First we present the results of simulation for 20000 avalanches in an infinite space initiated by a single electron. The results for the avalanche size distribution (figure 2) are useful for comparison with Legler’s theory of avalanche statistics which is often used in many RPC simulations and modeling [8]. Results show a deviation from the predicted exponential dependence (3.2) mostly prominent at small avalanche sizes. This deviation follows from an approximation of constant first

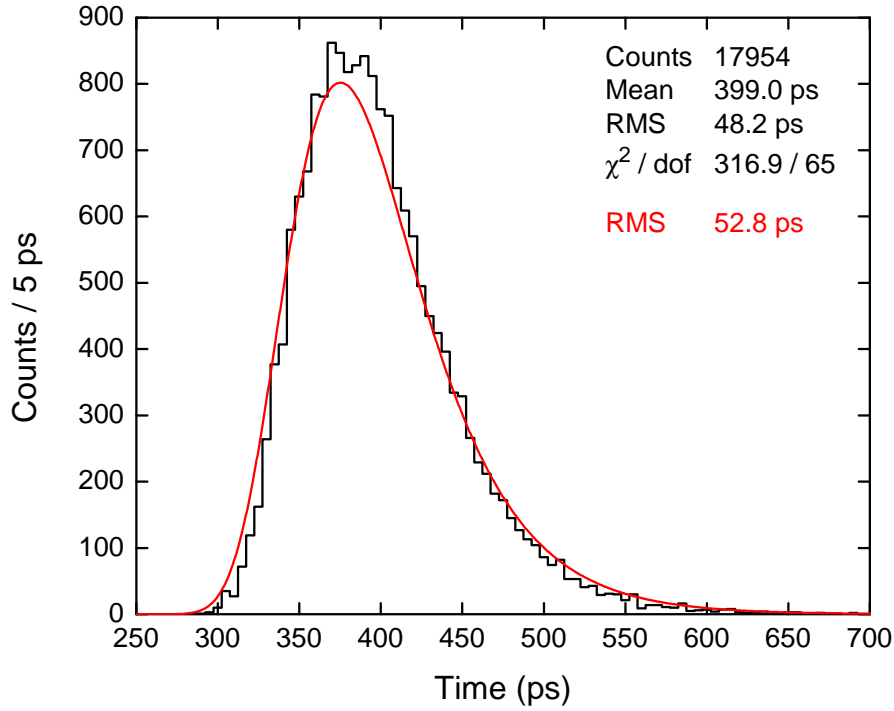


Figure 3. Timing distribution for single electron avalanches. The threshold is set to 10000 electrons and our cross sections for $\text{C}_2\text{H}_2\text{F}_4$ [25] are assumed. $E/N = 439$ Td.

Townsend ionization coefficient, assumed by Legler’s basic model. In reality, however, the ionization coefficient varies during avalanche development, especially in the initial stages where only one or just a few electrons are present. Without going into further details, it should be mentioned that there have been several attempts to describe and to deal with this issue in Legler’s theory [36]. Unfortunately, even after setting aside the question of their validity and justification, each of these attempts makes the solution for the avalanche size distribution unobtainable in closed form. On the other hand, microscopic Monte Carlo approach does not have to deal with these approximations since the avalanche statistics arise naturally from the stochastic character of electron-molecule collisions. This is the key difference between our model and the other RPC models based on theoretical avalanche size distributions (mostly Legler or Polya type).

Figure 3 shows the timing distribution for a threshold of 10000 electrons. The expected theoretical distribution was calculated using the time response function for the case of single electron avalanches [13]:

$$\rho(n_{\text{th}}, t) = \frac{n_{\text{th}} S (1 - k)}{1 - \exp(-n_{\text{th}} (1 - k))} \exp(-St - n_{\text{th}} (1 - k) \exp(-St)) .$$

The slight disagreement with the theoretical distribution can be attributed to the same cause as the disagreement between avalanche size distributions discussed in the previous paragraph. Since the corresponding theoretical avalanche size distribution is “wider” (i.e. has larger standard deviation) than the simulated one, we expected the same for the timing distribution, which is the case. A test was also made with different energy distribution for the initial electron as in the late stage of avalanche development (mean energy of 6.7 eV). The test showed that the higher initial electron en-

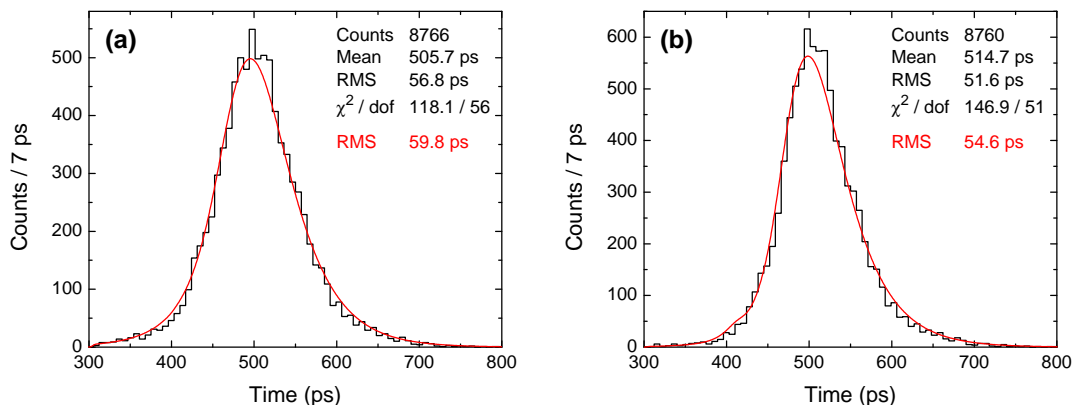


Figure 4. Timing distribution for avalanches started by primary ionization generated using (a) $1/n^2$, (b) HEED cluster size distribution. Infinite space. The threshold is set to 10^6 electrons and our cross sections for $\text{C}_2\text{H}_2\text{F}_4$ [25] are assumed. $E/N = 439$ Td.

ergy had practically no effect on the r.m.s. value of threshold crossing times (it was lower by 0.2 ps) while the number of avalanches which reached the threshold was slightly higher (18350). The latter was expected since the initial electron with higher energy had a lower probability for attachment.

3.3 Avalanches started by primary ionization

The case of avalanches started by primary ionization progressing in an infinite space was also studied. The primary ionization was generated according to the model described in section 2.1. Simulations with 10000 events were made for $1/n^2$ and HEED cluster size distributions. Figure 4 shows the timing distribution for a threshold of 10^6 electrons. The theoretical distributions were calculated using the model (3.1). Slightly higher theoretical r.m.s. values have already been discussed in the previous section. As of distribution shape, one can see that the left tail of the distribution for the $1/n^2$ case is wider than in the case where HEED cluster size distribution was used. This is expected since the left tail represents the fastest events which most often come from high primary ionization, and the probability for large primary clusters is higher in the case of $1/n^2$ distribution (figure 1). The same reasoning applies for the difference between r.m.s. values for the $1/n^2$ and HEED case.

3.4 Full model with primary ionization and boundaries

We now consider the effects of boundaries with gas gap set to 0.3 mm. Avalanches initiated by primary ionization move towards the anode due to electric field. When an electron reaches the anode it is removed from the simulation. Figure 5 shows the results for timing distribution with a threshold of 10^6 electrons. Since the simulation also consists of 10000 events, comparing the number of events which reached the threshold with the one from the previous case without boundaries, one can see the “absorbing effect” of the anode. Also, a slightly higher r.m.s. value can be attributed to the uncertainty of cluster positions, especially the ones closest to the anode which are the first to be absorbed.

The same simulation was performed for a threshold of 2 fC of induced charge. This value corresponds to about 10^6 electrons in the gas gap when the threshold is reached. One could expect

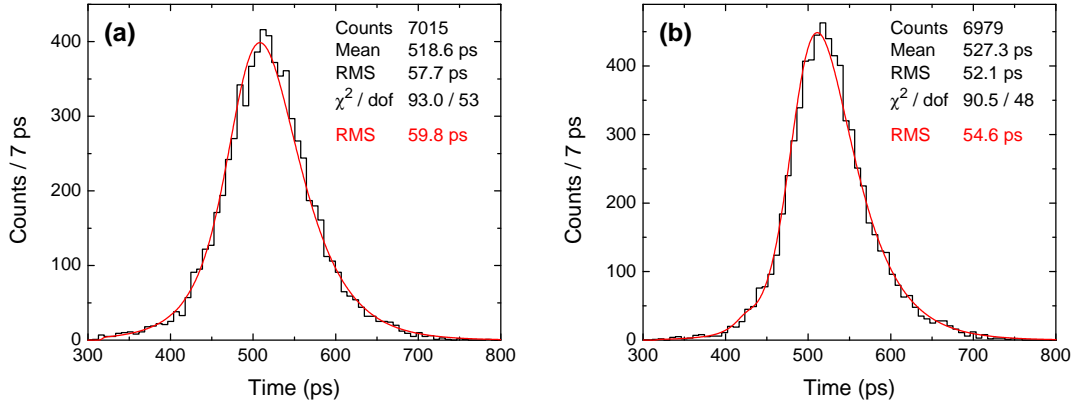


Figure 5. Timing distribution for avalanches started by primary ionization generated using (a) $1/n^2$, (b) HEED cluster size distribution. Gas gap 0.3 mm. The threshold is set to 10^6 electrons and our cross sections for $C_2H_2F_4$ [25] are assumed. $E/N = 439$ Td.

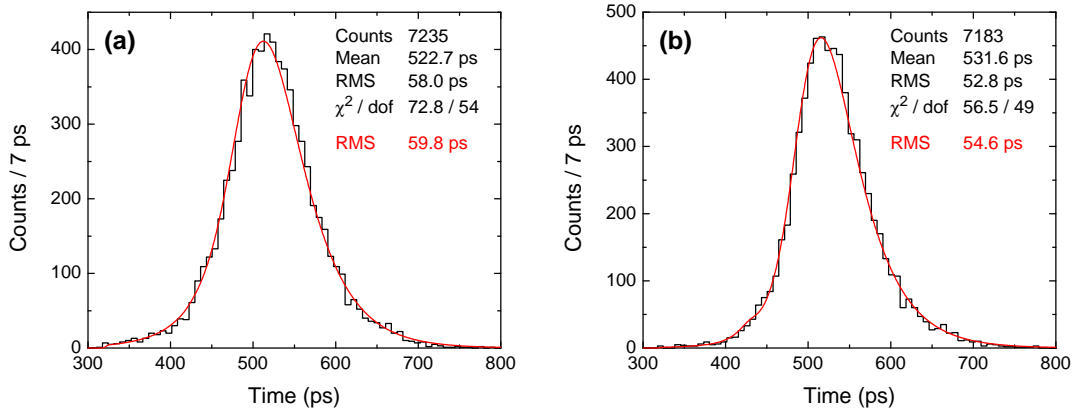


Figure 6. Timing distribution for avalanches started by primary ionization generated using (a) $1/n^2$, (b) HEED cluster size distribution. Gas gap 0.3 mm. The threshold is set to 2 fC and our cross sections for $C_2H_2F_4$ [25] are assumed. $E/N = 439$ Td.

somewhat different results when boundaries are present, because this time the threshold is given by induced charge i.e. the integral of the induced current (which is proportional to the number of electrons in the gas gap). However, the results for this case (figure 6) show that practically only the number of events which reached the threshold is slightly higher than in the case when the threshold is 10^6 electrons. A possible explanation lies in the cumulative character of the induced charge in such way that the avalanches which are absorbed in the anode are not completely “lost” as if they were not present at all. Instead, they contribute to the induced charge, and the other avalanches which would otherwise be too small or too close to the anode to reach the threshold alone, can also contribute so that eventually the threshold is reached.

Finally, we present the results for timing resolution (figure 7) and efficiency (figure 8) of the RPC. The results were made for a range of electric field strengths, different $C_2H_2F_4$ cross section sets and primary cluster size distributions. For each set of parameters 10000 events were simulated with the threshold set to 2 fC. The timing resolution is simply the r.m.s. of the threshold crossing times while the efficiency is the fraction of events which have reached the threshold. Results are

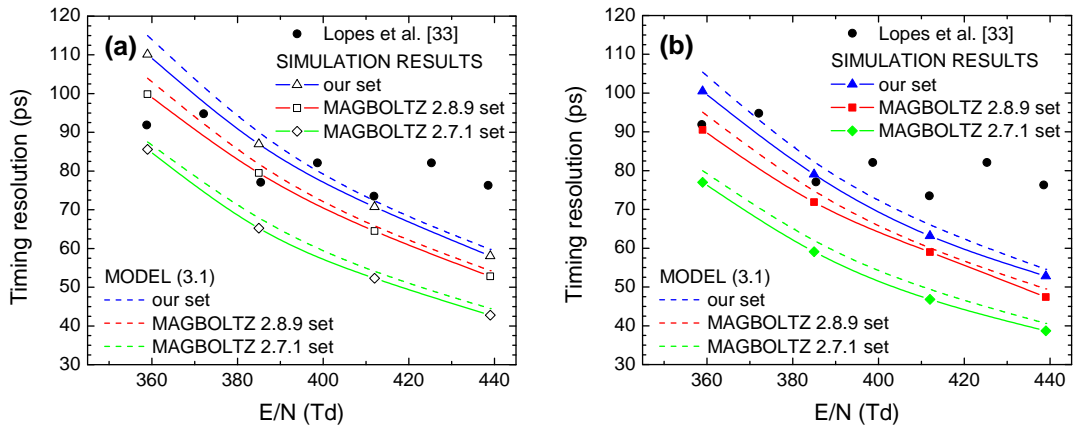


Figure 7. Timing resolutions for different C₂H₂F₄ cross section sets and primary ionization models, (a) $1/n^2$, (b) HEED cluster size distribution. Comparison with experimental values by Lopes et al. [37].

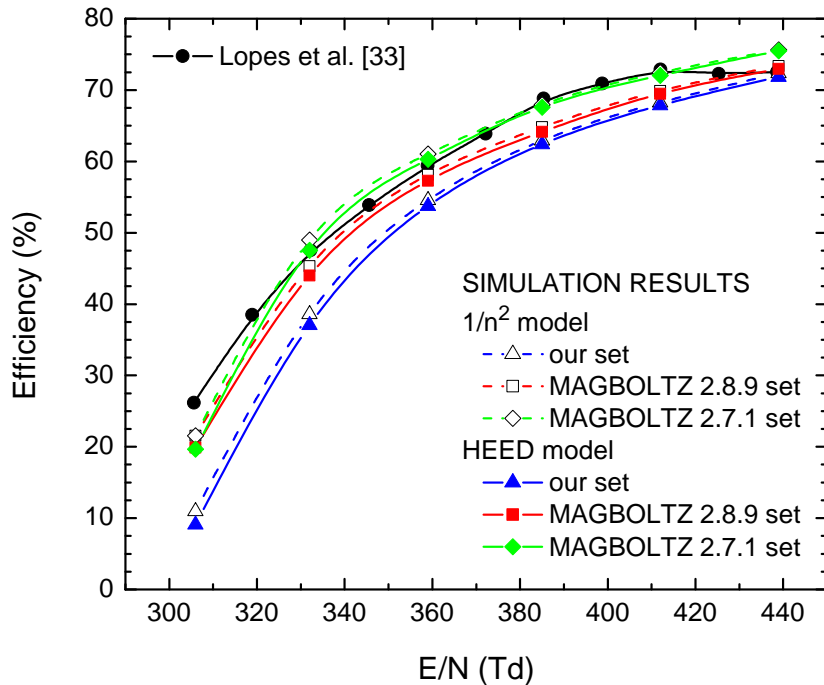


Figure 8. Efficiencies for different C₂H₂F₄ cross section sets and primary ionization models, (a) $1/n^2$, (b) HEED cluster size distribution. Comparison with experimental values by Lopes et al. [37].

compared with measurements by Lopes et al. [37] which show a clear fluctuation of the timing resolution, probably due to some kind of experimental uncertainty. Also, the measured timing resolutions and efficiencies both show a pronounced saturation effect at higher electric field strengths which is not present in our results. The theoretical timing resolutions, calculated using (3.1), are in good agreement with the simulated ones. The discrepancy between the results for different C₂H₂F₄ cross sections sets is expected since the effective ionization rate is the dominant factor in both timing and efficiency [8]. Somewhat higher efficiency in the $1/n^2$ case is a consequence of larger mean cluster size than in the case of HEED cluster size distribution. It should also be mentioned that the

tests with different energy distributions for the initial electrons showed no effect on the timing, but the efficiencies were higher by 1-2% in case when mean initial electron energy was set to 10 eV.

4 Summary and conclusions

A microscopic Monte Carlo approach, based on tracking of individual electrons and their collisions with the gas molecules, was developed and used with the aim of obtaining the performance characteristics of a timing RPC. The development of electron avalanches in infinite space was also studied and the results for threshold crossing times showed good agreement with an analytical model. Since the energy distribution of the initial electrons showed no effect on timing, the minor differences can only be attributed to Legler's basic theory of avalanche statistics, assumed in this analytical model.

The realistic RPC simulations with implemented gas gap boundaries and primary ionization models were performed with three different sets of cross sections for electron scattering in $C_2H_2F_4$. The inclusion of boundaries show no significant effect on timing, unlike the effect of different cross section sets which is very prominent. Overall, the results for timing and efficiency show good agreement with experimental values. Because of limited computing resources, a relatively low value of signal threshold was chosen corresponding to about 10^6 electrons in the gas gap. Still, the results can be considered valid as the theory and experiments show that the timing resolution does not depend on the threshold level. The extension of the threshold to realistic levels where space charge is present, without sacrifice in accuracy, is an ongoing work.

Acknowledgments

This work was supported by MPNTRRS Projects OI171037 and III41011.

References

- [1] R. Santonico and R. Cardarelli, *Development of resistive plate counters*, *Nucl. Instrum. Meth.* **187** (1981) 377.
- [2] R. Santonico, R. Cardarelli, A. Di Biagio and A. Lucci, *Progress in Resistive Plate Counters*, *Nucl. Instrum. Meth. A* **263** (1988) 20.
- [3] ATLAS collaboration, *The ATLAS experiment at the CERN LHC*, *2008 JINST* **3** S08003.
- [4] ALICE collaboration, *The ALICE experiment at the CERN LHC*, *2008 JINST* **3** S08002.
- [5] CMS collaboration, *The CMS experiment at the CERN LHC*, *2008 JINST* **3** S08004.
- [6] P. Fonte, *Applications and new developments in resistive plate chambers*, *IEEE Trans. Nucl. Sci.* **49** (2002) 881.
- [7] G. Georgiev et al., *Multigap RPC for PET: development and optimisation of the detector design*, *2013 JINST* **8** P01011.
- [8] P. Fonte, *Survey of physical modelling in Resistive Plate Chambers*, *2013 JINST* **8** P11001.
- [9] W. Riegler and C. Lippmann, *The physics of resistive plate chambers*, *Nucl. Instrum. Meth. A* **518** (2004) 86.

- [10] S. Mohammed, R. Hasan, N. Majumdar, S. Mukhopadhyay and B. Satyanarayana, *Simulation studies on the Effect of SF₆ in the RPC gas mixture*, *PoS(RPC2012)* 034.
- [11] L. Khosravi Khorashad, A. Moshaii and S. Hosseini, *Fast and total charges in a resistive plate chamber: a numerical approach*, *Europhys. Lett.* **96** (2011) 45002.
- [12] A. Moshaii, L. Khosravi Khorashad, M. Eskandari and S. Hosseini, *RPC simulation in avalanche and streamer modes using transport equations for electrons and ions*, *Nucl. Instrum. Meth. A* **661** (2012) S168.
- [13] W. Riegler, *Time response functions and avalanche fluctuations in resistive plate chambers*, *Nucl. Instrum. Meth. A* **602** (2009) 377.
- [14] A. Mangiarotti, P. Fonte and A. Gobbi, *Exactly solvable model for the time response function of RPCs*, *Nucl. Instrum. Meth. A* **533** (2004) 16.
- [15] S.F. Biagi, *Monte Carlo simulation of electron drift and diffusion in counting gases under the influence of electric and magnetic fields*, *Nucl. Instrum. Meth. A* **421** (1999) 234.
- [16] S. Biagi, *MAGBOLTZ — Program to compute electron transport parameters in gases*, version 2, CERN.
- [17] D. Gonzalez-Diaz and A. Sharma, *Current challenges and perspectives in resistive gaseous detectors: a manifesto from RPC 2012*, *PoS(RPC2012)* 084.
- [18] H. Schindler, S.F. Biagi and R. Veenhof, *Calculation of gas gain fluctuations in uniform fields*, *Nucl. Instrum. Meth. A* **624** (2010) 78.
- [19] I.B. Smirnov, *Modeling of ionization produced by fast charged particles in gases*, *Nucl. Instrum. Meth. A* **554** (2005) 474.
- [20] I.B. Smirnov, *HEED — Program to compute energy loss of fast particles in gases*, Version 1.01, CERN.
- [21] W. Riegler, C. Lippmann and R. Veenhof, *Detector physics and simulation of resistive plate chambers*, *Nucl. Instrum. Meth. A* **500** (2003) 144.
- [22] S. Dujko, Z.M. Raspopović and Z.Lj. Petrović, *Monte Carlo studies of electron transport in crossed electric and magnetic fields in CF₄*, *J. Phys.* **D 38** (2005) 2952.
- [23] S. Dujko, R.D. White, K.F. Ness, Z.Lj. Petrović and R.E. Robson, *Non-conservative electron transport in CF₄ in electric and magnetic fields crossed at arbitrary angles*, *J. Phys.* **D 39** (2006) 4788.
- [24] S. Dujko, R.D. White and Z.Lj. Petrović, *Monte Carlo studies of non-conservative electron transport in the steady-state Townsend experiment*, *J. Phys.* **D 41** (2008) 245205.
- [25] O. Šašić, S. Dupljanin, J. de Urquijo and Z.Lj. Petrović, *Scattering cross sections for electrons in C₂H₂F₄ and its mixtures with Ar from measured transport coefficients*, *J. Phys.* **D 46** (2013) 325201.
- [26] J. de Urquijo, A.M. Juárez, E. Basurto and J.L. Hernández-Ávila, *Electron swarm coefficients in 1,1,1,2 tetrafluoroethane (R134a) and its mixtures with Ar*, *Eur. Phys. J.* **D 51** (2009) 241.
- [27] I.B. Lima et al., *Experimental investigations on the first Townsend coefficient in pure isobutane*, *Nucl. Instrum. Meth. A* **670** (2012) 55.
- [28] D. Bošnjaković, S. Dujko and Z.Lj. Petrović, *Electron transport coefficients in gases for Resistive Plate Chambers*, in proceedings of the 26th Summer School and International Symposium on the Physics of Ionized Gases, August 27, Zrenjanin, Serbia (2012).

- [29] H. Itoh, *Electron transport coefficients in SF₆*, *J. Phys.* **D 26** (1993) 1975.
- [30] S. Ramo, *Currents induced by electron motion*, *Proc. I.R.E.* **27** (1939) 584.
- [31] R.E. Robson, *Transport phenomena in the presence of reactions: definition and measurement of transport coefficients*, *Aust. J. Phys.* **44** (1991) 685.
- [32] S. Dujko, R.D. White, Z.M. Raspopović and Z.Lj. Petrović, *Spatially resolved transport data for electrons in gases: definition, interpretation and calculation*, *Nucl. Instrum. Meth.* **B 279** (2012) 84.
- [33] S. Dujko, Z.M. Raspopović, Z.Lj. Petrović and T. Makabe, *Negative mobilities of electrons in radio frequency fields*, *IEEE Trans. Plasma Sci. PS* **31** (2003) 711.
- [34] W. Legler, *Die Statistik der Elektronenlawinen in elektronegativen Gasen bei hohen Feldstärken und bei grosser Gasverstärkung*, *Z. Naturforsch.* **16a** (1961) 253.
- [35] H. Raether, *Electron avalanches and breakdown in gases*, Butterworths, London U.K. (1964).
- [36] W. Legler, *The influence of the relaxation of the electron energy distribution on the statistics of electron avalanches*, *Br. J. Appl. Phys.* **18** (1967) 1275.
- [37] L. Lopes, P. Fonte and A. Mangiarotti, *Systematic study of gas mixtures for timing RPCs*, *Nucl. Instrum. Meth.* **A 661** (2012) S194.